Ludwig-Maximilians-Universität

Sigillum Universitatis Ludovici Maximiliani

Interactions between Dark Energy and Dark Matter

Dissertation der Fakultät für Physik
Dissertation of the Faculty of Physics / Dissertazione della Facoltà di Fisica

der Ludwig-Maximilians-Universität München
at the Ludwig Maximilian University of Munich / dell'Università Ludwig Maximilian di Monaco

für den Grad des
for the degree of / per il titolo di

Doctor rerum naturalium

vorgelegt von Marco Baldi
presented by / presentata da

aus Bologna (Italien)
from / da

München, 10.02.2009

Sigillum Universitatis Ludovici Maximiliani

1. Gutachter: Prof. Dr. Simon D. M. White

referee: / relatore:

2. Gutachter: Prof. Dr. Jochen Weller

referee: / relatore:

Tag der mündlichen Prüfung: 20.03.2009

Date of the oral exam / Data dell'esame orale

Curriculum vitæ et studiorum

Marco Baldi

Personal data

First Name: Marco
Last name: Baldi
Date of birth: 4 January 1980
Place of birth: Bologna (Italy)
Citizenship: Italian
Hobbies: Music, Jazz Piano, Reading, Food and Wine
Sports: Football, Tennis, Sailing
Languages: Italian (native), English (excellent),
Spanish (good), German (Basic)

Contacts

✉ *Address:* c/o Max-Planck-Institut für Astrophysik
Karl-Schwarzschild-Straße, 1
D-85748 Garching b. München - M (Germany)
☎ *Phone:* +49 (0)89 30 000 2019, +39 051 520769
📱 *Mobile:* +49 (0)176 61065892, +39 348 2944353
@ *E-mail:* mbaldi@mpa-garching.mpg.de, mail@marcobaldi.it

Education

2009, 20th March: Ph. D. rer. nat. Ludwig-Maximilians-Universität München
Max-Planck-Institut für Astrophysik (Garching b. München)
2004, 17th December: Laurea in Physics
Alma Mater Studiorum · University of Bologna (Italy)
Faculty of Mathematical, Physical and Natural Sciences
Department of Physics
Thesis: *Perturbation evolution in cosmological models with dynamic dark energy*
Supervisors: Prof. Dr. Lauro Moscardini
Prof. Dr. Sabino Matarrese
Dr. Fabio Finelli
Final score: 110 / 110 cum laude
1998, July: Diploma di Maturità Scientifica
Liceo Scientifico Statale Augusto Righi - Bologna (Italy)
Final score: 60 / 60
1993 - 1998: Liceo Scientifico Statale Augusto Righi - Bologna (Italy)
1990 - 1993: Scuola Media Statale Giovanni Battista Gandino - Bologna (Italy)
1985 - 1990: Scuola Elementare Mario Longhena - Bologna (Italy)

Research

Subjects: Theoretical Cosmology - Dark Energy - Dark Matter - Structure Formation
Methods: Analytical - N-body Simulations

Refereed publications

✓ L. Amendola, **M. Baldi** and C. Wetterich, “Quintessence cosmologies with a growing matter component”, Phys. Rev. D **78** (2008) 023015

✓ **M. Baldi**, F. Finelli and S. Matarrese, “Inflation with violation of the null energy condition”, Phys. Rev. D **72** (2005) 083504

Non-refereed publications (proceedings and others)

✓ **M. Baldi**, V. Pettorino, G. Robbers and V. Springel, “N-body simulations of coupled dark energy cosmologies”, arXiv:0812.3901 [astro-ph], submitted to MNRAS

Marco Baldi

“…se pasean por todo el Mundo, mirando un mapa,
sin costarles blanca, ni padecer calor ni frío,
hambre ni sed.”

Miguel De Cervantes - El ingenioso Hidalgo Don Quijote de la Mancha
Parte II, Libro 3, Capitulo 6

“…they journey all over the Universe in a map,
without the expense and fatigue of traveling,
without suffering the inconveniences of heat, cold,
hunger, and thirst.”

Miguel De Cervantes - Don Quijote
Part II, Book 3, Chapter 6

Contents

Contents **3**

Zusammenfassung **19**

Abstract **21**

Introduction **23**

I General overview **27**

1 The Dark Energy issue **29**

1.1 The Standard Cosmological Model 29

1.2 The Cosmological Constant 32

1.3 Observational Evidence of Dark Energy 34

1.4 The Cosmological Constant Problems 36

2 Dynamic models of Dark Energy **41**

2.1 Quintessence 41

2.2 Phase-Space analysis 43

2.3 The properties of Scaling Solutions 45

2.4 Shortcomings of uncoupled dynamic Dark Energy 47

3 Interacting Dark Energy **51**

3.1 Motivations for interacting dark energy 51

3.2 Basic equations of an interacting dark energy component 54

3.3 Phase space analysis for coupled quintessence 56

3.4 The weak coupling regime and the ϕMDE phase 62

3.5 The strong coupling regime and the solution of the Coincidence Problem . . 65

3.6 A generalized model for interacting dark energy: background and perturbations evolution 67

II The Growing Neutrino Scenario 73

4 Quintessence models with a Growing Matter component 75

4.1 Multiple dark matter families 75

4.2 The Growing Matter Model 76

4.3 The Growing Neutrino Scenario 80

4.4 Enhanced growth of neutrino density fluctuations 81

4.5 Observational features 83

III Numerical Implementation and Cosmological Simulations 85

5 Numerical implementation of coupled dark energy models 87

5.1 Modified expansion rate 90

5.2 Mass variation 90

5.3 Cosmological extra friction 93

5.4 Fifth force implementation 94

5.5 Initial conditions 95

5.6 Summary of the coupled dark energy interaction scheme 100

5.7 Tests of the numerical implementation: the linear growth factor 101

6 The N-body simulations 103

6.1 Our set of N-body simulations 103

6.2 The results 104

6.3 Halo mass function 105

6.4 Matter power spectrum 110

6.5 Halo density profiles 114

6.6 Halo concentrations 117

6.7 Integrated bias and halo baryon fraction 129

Conclusions 137

Acknowledgments **141**

IV Bibliography **143**

List of Figures

1.1 Complementary fiducial constraints in the parameter plane $(\Omega_M, \Omega_\Lambda)$ at $z = 0$, coming from the analysis of Supernovae Ia, CMB anisotropies, and Large Scale Structure properties. This figure is taken from the *Supernova Cosmology Project* website *http://supernova.lbl.gov/* (Perlmutter, 2008). . . 37

2.1 Evolution with the scale factor a of the energy densities of different types of fluid: a Cosmological Constant (orange line) keeps a constant energy density during all the expansion history of the Universe, while radiation (green line) and matter (black line) scale respectively as a^{-4} and a^{-3}. A scalar field on a *tracking* scaling solution like the one given by the last critical point of Table 2.1 follows the behavior of the dominant barotropic fluid, and therefore scales as a^{-4} during radiation domination, and automatically switches to a^{-3} at equivalence. This behavior can in principle overcome the *Fine Tuning* problem by removing the need to set the initial dark energy density to unnaturally small values in the early Universe; however, as a consequence of the stability of the *tracking* scaling solution, it does not allow a late time dark energy domination. 48

3.1 The parameter plane (β, μ) for the autonomous system of Eqs. 3.20-3.22 as presented in Figure 1 of Amendola (2000), replotted here with the definitions and the conventions adopted in this work. Each region is labelled with the number corresponding to the only critical point that is stable in that region. The shaded areas correspond to the regions of the parameter space where the stable solution is also accelerated. 63

4.1 Cosmological evolution for neutrino Growing Matter for $\mu = 10$, $\gamma = 5.2$ and $m_\nu(t_0) = 2.3$ eV. *Panel a*: density fractions for radiation Ω_r (black, dotted line), cold dark matter Ω_c (dark-green, dot-dashed line), baryons Ω_b (blue, short-dashed line), dark energy Ω_ϕ (red, long-dashed line), and Growing Matter (neutrinos) Ω_g (light-green, solid line). *Panel b*: blow up of *Panel a* near the present time. *Panel c*: total equation of state $w_{\rm eff} \equiv p_{\rm tot}/\rho_{\rm tot}$ (red, long dashed line); combined equation of state of dark energy and neutrinos (blue, short-dashed line); and equation of state of the dark energy alone (green, solid line). *Panel d*: neutrino energy density ρ_g (red, long-dashed line) and neutrino mass m_ν (green, solid line) normalized to unity today. The dotted curve represents the energy density of always non-relativistic heavy Growing Matter. 81

5.1 *Top panel*: Hubble functions as a function of redshift for the different coupled dark energy models with constant coupling investigated in this work and listed in Table 5.2 as compared to ΛCDM (black curve). *Bottom panel*: Ratio of the Hubble functions of each coupled dark energy model to the Hubble function for the reference ΛCDM cosmology as a function of redshift. 91

5.2 Mass correction as a function of redshift for the coupled dark energy models with constant coupling investigated in this work and listed in Table 5.2 as compared to ΛCDM (black curve). 92

5.3 Gauge-invariant matter power spectra at $z = 60$ for the interacting dark energy models with constant coupling investigated in the present work as computed with the modified version of CMBEASY described in Chapter 3. The increase of power for $k \leqslant 0.004h$ Mpc^{-1} is due to the choice of the gauge-invariant variables for computing the evolution of perturbations implemented in CMBEASY. 96

5.4 Comparison of the function $f(a)$ with its usual approximation $f = \Omega_M^{0.55}$ and with the new fit of Eq. 5.11 for the models ΛCDM, RP1, RP2. 98

5.5 Comparison of the function $f(a)$ with its usual approximation $f = \Omega_M^{0.55}$ and with the new fit of Eq. 5.11 for the models RP3, RP4, RP5. 99

5.6 Comparison of the function $f(a)$ with its usual approximation $f = \Omega_M^{0.55}$ and with the new fit of Eq. 5.11 for the model RP6. 100

5.7 Schematic representation of the possible particle-particle interactions in our N-body simulations and of all the implemented modifications of the code GADGET-2 extensively discussed in this Chapter. 101

5.8 Evolution of the growth function with redshift for the seven models of coupled dark energy investigated with the low-resolution simulations ran with our modified version of GADGET-2. The solid lines are the total growth functions as evaluated numerically with CMBEASY, while the triangles are the growth functions evaluated from the simulations. The relative accuracy in reproducing the theoretical prediction is of the order of a few percent, irrespective of the coupling value β_c. 102

6.1 Projection on the x-y plane of the cold dark matter particles in the simulation box which lie within a slice of thickness $300h^{-1}$kpc perpendicular to the z axis, for the simulations ΛCDM and RP1. As a consequence of the choice of the same random phases for the initial conditions in the different runs the large scale structure looks the same for the two plots, and also in comparison with the plots of Fig. 6.2 in the next page. 106

6.2 Projection on the x-y plane of the cold dark matter particles in the simulation box which lie within a slice of thickness $300h^{-1}$kpc perpendicular to the z axis, for the simulations RP2 and RP5. As a consequence of the choice of the same random phases for the initial conditions in the different runs the large scale structure looks the same for the two plots, and also in comparison with the plots of Fig. 6.1 in the previous page. 107

6.3 Cumulative mass functions for the fully self-consistent high-resolution simulations of the models ΛCDM and RP1. The four differently-colored solid lines in each figure represent the cumulative mass function at four different redshifts in each of the investigated models. The dot-dashed lines are the corresponding predictions according to the Jenkins et al. (2001) formula, computed for each simulation with the appropriate growth function and power spectrum. 108

6.4 Cumulative mass functions for the fully self-consistent high-resolution simulations of the models RP2 and RP5. The four differently-colored solid lines in each figure represent the cumulative mass function at four different redshifts in each of the investigated models. The dot-dashed lines are the corresponding predictions according to the Jenkins et al. (2001) formula, computed for each simulation with the appropriate growth function and power spectrum. 109

6.5 Multiplicity functions for the high-resolution simulations of the models ΛCDM and RP1. The four differently-colored sets of data points are the multiplicity functions evaluated in equally spaced logarithmic mass bins at four different redshifts. The dot-dashed and dashed lines represent the predictions for the multiplicity function from Jenkins et al. (2001) and Sheth and Tormen (1999), respectively, computed for each simulation with the appropriate growth function and power spectrum. The comparison clearly shows a slightly better agreement with the fitting function by Sheth and Tormen (1999), in particular at high redshift. 111

6.6 Multiplicity functions for the high-resolution simulations of the models RP2 and RP5. The four differently-colored sets of data points are the multiplicity functions evaluated in equally spaced logarithmic mass bins at four different redshifts. The dot-dashed and dashed lines represent the predictions for the multiplicity function from Jenkins et al. (2001) and Sheth and Tormen (1999), respectively, computed for each simulation with the appropriate growth function and power spectrum. The comparison clearly shows a slightly better agreement with the fitting function by Sheth and Tormen (1999), in particular at high redshift. 112

6.7 Power spectra of cold dark matter (black line) and baryons (blue line) at $z = 0$ for the set of coupled dark energy models under investigation. The appearance of a bias between the two distributions, which grows with increasing coupling β_c, is clearly visible at the large scale end of the plots. The last two panels show the comparison of a ΛCDM and a coupled dark energy cosmology with $\beta_c = 0.2$ in absence of hydrodynamic forces acting on baryons. In these two panels, the bias on all scales is purely due to the interaction of cold dark matter with the dark energy scalar field ϕ. 113

6.8 Ratio of the power spectra of baryons and cold dark matter as a function of wavenumber for the set of high-resolution simulations ran with our modified version of GADGET-2, for the redshifts $z = 10.06$ and $z = 5.35$. The linear large-scale bias appears already at high redshifts, while at lower redshifts the hydrodynamic forces start to suppress power in the baryon component at small scales. In absence of such hydrodynamic forces the progressive enhancement of the large scale bias at small scales for the RP5-NO-SPH run (light green curve) as compared to the completely flat behavior of the ΛCDM-NO-SPH simulation (blue curve) – where no bias is expected – shows clearly that non-linearities must increase the effect of the coupling on the different clustering rates of the two species. All the curves have been corrected for a spurious numerical drop of the baryonic power at small scales as described in the text. 115

6.9 Ratio of the power spectra of baryons and cold dark matter as a function of wavenumber for the set of high-resolution simulations ran with our modified version of GADGET-2, for the redshifts $z = 1.52$, and $z = 0.0$. The linear large-scale bias appears already at high redshifts, while at lower redshifts the hydrodynamic forces start to suppress power in the baryon component at small scales. In absence of such hydrodynamic forces the progressive enhancement of the large scale bias at small scales for the RP5-NO-SPH run (light green curve) as compared to the completely flat behavior of the ΛCDM-NO-SPH simulation (blue curve) – where no bias is expected – shows clearly that non-linearities must increase the effect of the coupling on the different clustering rates of the two species. All the curves have been corrected for a spurious numerical drop of the baryonic power at small scales as described in the text. 116

6.10 Density profiles of cold dark matter (solid lines) and baryons (dot-dashed lines) for two halos of virial masses $M_{200} = 2.83 \times 10^{14} h^{-1} M_{\odot}$ and $M_{200} = 2.78 \times 10^{13} h^{-1} M_{\odot}$ in the simulation box at $z = 0$. The vertical dot-dashed line indicates the location of the virial radius for the ΛCDM halo. The decrease of the inner overdensity of the profiles with increasing coupling is clearly visible in both plots. 118

6.11 Density profiles of cold dark matter (solid lines) and baryons (dot-dashed lines) for two halos of virial masses $M_{200} = 1.7 \times 10^{13} h^{-1} M_{\odot}$ and $M_{200} = 6.51 \times 10^{12} h^{-1} M_{\odot}$ in the simulation box at $z = 0$. The vertical dot-dashed line indicates the location of the virial radius for the ΛCDM halo. The decrease of the inner overdensity of the profiles with increasing coupling is clearly visible in both plots. 119

6.12 Relative variation with respect to ΛCDM of the scale radius r_s for the four halos plotted in Figs. 6.10,6.11 as a function of coupling β_c. 121

6.13 Variation of the mean halo concentration as a function of mass for the 200 most massive halos in our simulations and for the different cosmological models under investigation. The concentrations have been computed by directly fitting the halo density profile of each halo with an NFW model (*top panel*) or by using the method introduced by Springel et al. (2008) and described in Eqs. 6.3,6.4 (*bottom panel*). The halos have been binned by mass, and the mean concentration in each bin is plotted as a filled circle. The colored dashed lines indicate for each simulation the spread of 68% of the halos in each mass bin. The highest mass bin is not plotted because of its very low number of halos. The decrease of the mean concentration with increasing coupling appears in the same way in both plots. 123

6.14 Mean halo formation redshift z_f as a function of halo mass for the 200 most massive halos in our simulations and for the different cosmological models under investigation. The formation redshift z_f is defined as the redshift at which the main progenitor of the halo has a virial mass equal to half the virial mass of the halo at $z = 0$. The halos have been binned by mass, and the mean formation redshift in each bin is plotted as a filled circle. The colored dashed lines indicate for each simulation the spread of 68% of the halos in each mass bin. The highest mass bin is not plotted because of its too low number of halos. 124

6.15 Variation of halo concentrations for the same models and the same halo sample as in Fig. 6.13, and for an additional test simulation in each of the two panels. In the *top panel*, the simulation RP5-NO-MASS shows the effect of switching off the mass correction for $z < z^{*} \sim 1.5$: there is a small but systematic increase of average halo concentrations over the whole mass range. In the *bottom panel*, the simulation RP5-NO-FRIC shows the effect of switching off in the same redshift interval the friction term. The increase of concentrations in this case is much more consistent and accounts for a large fraction of the total concentration reduction of RP5. 126

6.16 Evolution with respect to the scale factor a of the average mass (solid) and of the average number of particles (dashed) enclosed in a sphere of physical radius $r = 20h^{-1}$kpc centered on the potential minimum of each halo in our sample. The curves are normalized at $a = 0.48$ ($z \sim 1$) and show the expected flat behavior for the ΛCDM case (black line) for which the solid and the dashed curves coincide due to the constancy of the mass of particles. For the RP5 case (light blue curves), there is a strong decrease in time of both mass and particle number, which clearly illustrates the expansion of RP5 halos with respect to the ΛCDM case. By switching off the extra friction acting on cold dark matter particles (RP5-NO-FRIC, light green curves), an almost flat behavior is recovered again for the particle number, while the decrease of mass is now due to the particle mass variation – which is still in place for this simulation – on top of the particle number evolution. This plot therefore clearly shows that the extra physics of coupled dark energy cosmologies induces an overall expansion of cold dark matter halos at low redshifts, and clearly identifies the friction term as the leading mechanism that produces this expansion. 128

6.17 Variation of the integrated bias $B(< r)$ for the four fully self-consistent high-resolution simulations and for two selected halos of mass $M_{200} = 1.58 \times 10^{14}h^{-1}M_{\odot}$ and $M_{200} = 2.76 \times 10^{13}h^{-1}M_{\odot}$ in our sample. The horizontal dashed lines indicate the value of the large scale linear bias as evaluated from the power spectrum amplitudes of baryons and cold dark matter. The vertical black dot-dashed line shows the position of the virial radius for the ΛCDM halo in the sample. The drop of the value of $B(< r)$ in the innermost regions of the halos is evident but in these runs is given by a superposition of effects due to hydrodynamical forces and to the modified gravitational interaction. On large scales, the bias tends to converge to the linear value, as expected. 130

6.18 Variation of the integrated bias $B(< r)$ for the four fully self-consistent high-resolution simulations and for two selected halos of mass $M_{200} = 1.10 \times 10^{13} h^{-1} M_{\odot}$ and $M_{200} = 7.79 \times 10^{12} h^{-1} M_{\odot}$ in our sample. The horizontal dashed lines indicate the value of the large scale linear bias as evaluated from the power spectrum amplitudes of baryons and cold dark matter. The vertical black dot-dashed line shows the position of the virial radius for the ΛCDM halo in the sample. The drop of the value of $B(< r)$ in the innermost regions of the halos is evident but in these runs is given by a superposition of effects due to hydrodynamical forces and to the modified gravitational interaction. On large scales, the bias tends to converge to the linear value, as expected. 131

6.19 Variation of the integrated bias $B(< r)$ for the two high-resolution simulations without hydrodynamical forces on baryon particles for the same two halos shown in Fig. 6.17. The enhancement of the bias due to the extra scalar force in the core of highly non-linear structures appears here clearly. . 133

6.20 Variation of the integrated bias $B(< r)$ for the two high-resolution simulations without hydrodynamical forces on baryon particles for the same two halos shown in Fig. 6.18. The enhancement of the bias due to the extra scalar force in the core of highly non-linear structures appears here clearly. . 134

6.21 Variation with virial mass M_{200} of the relative baryon fraction Y_b within the virial radius r_{200} of all the halos in our sample. The colored diamonds represent the relative baryon fraction of each single halo, while the filled circles and the colored curves show the behavior of the mean relative baryon fraction in each mass bin for the four fully self-consistent high-resolution simulations. A decrease of Y_b with increasing coupling is clearly visible both in the distribution of the individual halos and in the averaged curves. 135

List of Tables

2.1 Table of the five critical points for the system 2.16-2.17 with the corresponding existence conditions and stability conditions, as determined by an analysis of the eigenvalues of the system (see Copeland et al. (1998)). The last two columns contain respectively the energy density of the scalar field Ω_{ϕ} and its equation of state w_{ϕ} for each critical point. 45

3.1 List of the critical points for the autonomous system 3.20-3.22 within the quarter of unitary sphere with positive y and z. The values of the variables x, y, and z for each critical point are listed together with the corresponding value of the total dark energy density Ω_{ϕ}, the effective equation of state of the Universe $w_{\rm eff}$ introduced in Eq. 3.24, and the scalar field equation of state w_{ϕ}. 58

3.2 Existence, stability, and acceleration conditions in the parameter space (β, μ) for all the critical points listed in Table 3.1. The table corresponds to the analysis done in Amendola (2000) for the definitions and the conventions adopted in this work, and where a few misprints present in Amendola (2000) have been corrected. 61

5.1 Cosmological parameters for our set of N-body simulations, consistent with the WMAP 5 year results for a ΛCDM cosmology (Komatsu et al., 2008). . 88

5.2 List of the different simulations performed with our modified version of GADGET-2. The simulations have different force and mass resolution, and are accordingly labelled as *low* or *high* resolution. Notice that the values of the coupling listed here are different from the ones adopted in Macciò et al. (2004) due to the different definition of the coupling function 3.37. However, the models in effect have *identical* coupling strength to those investigated in Macciò et al. (2004). 89

5.3 List of input functions for the coupled dark energy implementation in GADGET-2. 90

6.1 Evolution of the scale radius r_s for the four halos shown in Figs. 6.10,6.11 with respect to the corresponding ΛCDM value. The trend is towards larger values of r_s with increasing coupling β_c, with a relative growth of up to 36% for the largest coupling value $\beta_c = 0.2$. 120

Zusammenfassung

In dieser Arbeit haben wir kosmologische Modelle analysiert, in welchen dunkle Energie mit anderen Materieformen wechselwirkt. Wir haben den Einfluss solch einer Kopplung sowohl auf die Expansionsgeschichte des Universums als auch auf die kosmische Strukturbildung untersucht.

Für ersteres haben wir ein kosmologisches Modell entwickelt, in welchem eine Materieform existiert, die aus Teilchen mit stets zunehmender Masse besteht. In einem solchen Modell bremst das Auftreten einer *Growing Matter* Komponente, welche im frühen Universum noch vernachlässigbar ist, die Entwicklung des Skalarfeldes, welches die dunkle Energie beschreibt, bei einer Rotverschiebung von etwa 6 dramatisch ab. Dadurch wird die beschleunigte Expansion des Universums eingeleitet, was eine Lösung des Koinzidenzproblems darstellen könnte. Wir schlagen vor, eine solche *Growing Matter* Komponente mit kosmischen Neutrinos zu identifizieren. In diesem Fall kann die heutige dunkle Energiedichte mit der gemessenen durchschnittlichen Neutrinomasse in Verbindung gebracht werden.

Für letzteres haben wir die neuen physikalischen Eigenschaften von Modellen mit gekoppelter dunkler Energie in dem kosmologischen N-body Code GADGET-2 implementiert. Wir präsentieren die Ergebnisse einer Reihe hochaufgelöster Simulationen für eine einfache Form der Wechselwirkung von dunkler Energie mit Materie. Als eine Folge der neuen Physik entwickeln sich die Dichteverteilungen von kalter dunkler Materie und Baryonen sowohl im linearen als auch im nichlinearen Bereich der Strukturbildung unterschiedlich. Schon auf gro/ssen Skalen entwickelt sich ein linearer Bias zwischen den beiden Komponenten, welcher durch die nichtlineare Entwicklung noch weiter verstärkt wird. Im Gegensatz zu früheren Arbeiten finden wir auch, dass die Dichteprofile von Halos aus kalter dunkler Materie in Kosmologien mit gekoppelter dunkler Energie im Vergleich zu ΛCDM-Kosmologien weniger stark konzentriert sind. Zudem ist der Baryonenanteil in Halos verglichen mit dem mittleren Baryonenanteil im Universum in gekoppelten Modellen signifikant reduziert. Die obigen Eigenschaften unserer Modelle reduzieren Unstimmigkeiten, die auf kleinen Skalen zwischen Beobachtungen und dem ΛCDM-Modell existieren. Unsere Methodologie ist ideal dafür geeignet, die Vorhersagen von Kosmologien mit gekoppelter dunkler Energie im vollständig nichtlinearen Bereich zu testen. Dies kann starke Einschränkungen an den erlaubten Parameterbereich solcher Szenarien liefern.

Abstract

We have investigated interacting dark energy cosmologies both concerning their impact on the background evolution of the Universe and their effects on cosmological structure growth.

For the former aspect, we have developed a cosmological model featuring a matter species consisting of particles with a mass that increases with time. In such model the appearance of a *Growing Matter* component, which is negligible in early cosmology, dramatically slows down the evolution of the dark energy scalar field at a redshift around six, and triggers the onset of the accelerated expansion of the Universe, therefore addressing the Coincidence Problem. We propose to identify this *Growing Matter* component with cosmic neutrinos, in which case the present dark energy density can be related to the measured average mass of neutrinos.

For the latter aspect, we have implemented the new physical features of interacting dark energy models into the cosmological N-body code GADGET-2, and we present the results of a series of high-resolution simulations for a simple realization of dark energy interaction. As a consequence of the new physics, cold dark matter and baryon distributions evolve differently both in the linear and in the non-linear regime of structure formation. Already on large scales, a linear bias develops between these two components, which is further enhanced by the non-linear evolution. We also find, in contrast with previous work, that the density profiles of cold dark matter halos are less concentrated in coupled dark energy cosmologies compared with ΛCDM. Also, the baryon fraction in halos in the coupled models is significantly reduced below the universal baryon fraction. These features alleviate tensions between observations and the ΛCDM model on small scales. Our methodology is ideally suited to explore the predictions of coupled dark energy models in the fully non-linear regime, which can provide powerful constraints for the viable parameter space of such scenarios.

Introduction

The nature and the properties of dark energy and dark matter constitute one of the most central problems in modern astrophysics, and in science in general.
While the evidence for their existence today seems incontrovertible after more than a decade of cosmological observations, all confirming the need to introduce in our models of the Cosmos these two mysterious components, their fundamental nature remains unknown.
An enormous effort is being made, from several different perspectives, to unveil the mystery and to shed some light on the "dark sector" that dominates the energy density of our Universe.

In the present work, we contribute to this effort by investigating the possibility – proposed by Wetterich (1995) – that these two components might directly interact with each other by exchanging energy during their cosmic evolution. Our approach consists in a phenomenological representation of the dark energy as a dynamical quantity replacing the Cosmological Constant of the standard cosmological model (which we review in Chapter 1), and in a phenomenological description of the interaction between such a dynamic dark energy component and a perfect dark matter fluid.

The investigation that we present here relies on a large literature (recalled in Chapters 2 and 3) concerning the study of the main features of such interacting dark energy models, and aims at extending it in a twofold way: on one side, we propose an extension of the basic model of dark energy interaction to a case where more than one dark matter family is present in the Universe; on the other side, we develop a new tool capable of following the dynamics of the coupled dark energy models down to the non-linear regime of gravitational instability, thereby opening new observational channels to constrain the whole scenario.

For the first of these tasks, described in Chapter 4, we have further developed the multiple dark matter scenario first introduced by Huey and Wandelt (2006), identifying the cases in which such a model can contribute to the solution of the *Coincidence Problem*, and we have also proposed to identify one of the dark matter families of the model with cosmic neutrinos. This assumption avoids the introduction of any new unknown particle in the model, and allows to relate some cosmological properties to a directly measurable quantity as the neutrino mass. Furthermore, we have studied the compatibility of this model with the present cosmological observations and described possible characteristic observational features to look for in the future in order to test, constrain, or rule out such a "*Growing Neutrino*" scenario.

For the second of these tasks we have developed and tested a modification of the cosmological N-body code GADGET-2 (Springel, 2005) suitable for integrating the newtonian limit of gravitational dynamics in a wide variety of interacting dark energy models. This implementation is fully described in Chapter 5, and consists in including in the integration algorithm all the new physical effects that the interaction of dark energy with other cosmic fluids induces. These effects consist in a modified expansion history of the Universe, which influences the dynamics of all the particles in the simulation, and, for the coupled particles only, in a time dependence of the mass, an enhanced effective mutual gravitational attraction, and an additional non-conservative friction acceleration.

We have then used this modified N-body code to run some high-resolution hydrodynamic cosmological N-body simulations for a simple realization of the dark energy interaction and for different values of the coupling strength. The results of these simulations are discussed in Chapter 6. In the analysis of the non-linear effects of the dark energy interaction we focused our attention on the properties of massive collapsed objects, identifying the main modifications with respect to the standard cosmological ΛCDM model. In particular, we found that the density profiles of massive halos are less overdense in the center for increasing coupling as compared to their ΛCDM counterparts, and that the halo concentrations therefore decrease significantly in coupled dark energy models. Furthermore, the halo baryon fraction is reduced, which alleviates tensions with present observations of galaxy clusters.

Part I

General overview

Chapter 1

The Dark Energy issue

1.1 The Standard Cosmological Model

Modern Cosmology is based on the field equations of General Relativity which can be written as:

$$G_{\mu\nu} = \kappa^2 T_{\mu\nu} \, , \tag{1.1}$$

where $\kappa^2 \equiv 8\pi G$, G being Newton's gravitational constant. The quantity that appears on the left hand side of Eq. 1.1 is the Einstein Tensor:

$$G_{\mu\nu} \equiv R_{\mu\nu} - \frac{1}{2} R g_{\mu\nu} \, , \tag{1.2}$$

and encodes information about the geometry of space-time[1]. The different quantities that appear in Eq. 1.2 are the space-time metric tensor $g_{\mu\nu}$, which defines the line element of space-time[2]:

$$ds^2 = g_{\mu\nu} dx^\mu dx^\nu \, , \tag{1.3}$$

and the two contractions of the Riemann Tensor $R^\sigma_{\lambda\mu\nu}$, namely the Ricci Tensor:

$$R_{\mu\nu} \equiv R^\sigma_{\mu\sigma\nu} \, , \tag{1.4}$$

and the Curvature Scalar:

$$R \equiv R^\mu_\mu = g^{\mu\nu} R_{\mu\nu} \, . \tag{1.5}$$

The quantity that appears on the right hand side of Eq. 1.1 is the total stress-energy tensor, which encodes information about the energy distribution in the Universe, and that for a perfect fluid in its own rest frame can be written as:

---

[1] In this work we always assume greek indices to span over space-time coordinates, i.e. $\mu = (0, 1, 2, 3)$, and latin indices to span over space dimensions only, i.e. $i = (1, 2, 3)$. Furthermore, the Einstein convention for the contraction of repeated indices is always used.

[2] We assume here the (-,+,+,+) convention for the metric signature.

$$T_{\mu\nu} = (\rho + p)u_\mu u_\nu + p g_{\mu\nu}\,, \tag{1.6}$$

where ρ and p are, respectively, the energy density and the pressure of the fluid, and u_μ is the 4-velocity of the fluid element.

The ratio between pressure and density of a fluid defines its equation of state w[3]:

$$w \equiv \frac{p}{\rho}\,. \tag{1.7}$$

In general, different types of fluids with different equations of state are present in the Universe , and therefore the stress-energy tensor of Eq. 1.1 will be in general the sum of different stress-energy tensors which will take, for each of the different fluids, the form 1.6 with the respective values of ρ and p.

The assumption of General Covariance for General Relativity determines a constraining condition on the Einstein Tensor 1.2 which goes under the name of the *Contracted Bianchi Identities* (Weinberg, 1972):

$$\nabla_\mu G^\mu_\nu = 0\,, \tag{1.8}$$

and as a consequence of the tensor character of Eq. 1.1, this property needs to hold also for the total stress-energy tensor T^μ_ν:

$$\nabla_\mu T^\mu_\nu = 0\,. \tag{1.9}$$

Besides the Einstein Field Equations 1.1, a second fundamental pillar of modern cosmology is the assumption that space-time can be sliced in space-like hypersurfaces which are homogeneous and isotropic on large scales. This slicing of space-time in space-like hypersurfaces defines a global time-like parameter which is called the *Cosmic Time* t and which, for all practical purposes, can be identified as a global time variable. This assumption goes under the name of the *Cosmological Principle*, and has been recently challenged by several authors (Ellis and Stoeger, 1987; Buchert, 2000; Kolb et al., 2005; Chuang et al., 2008; Paranjape and Singh, 2006). Nevertheless, we will always assume in this work that the Cosmological Principle holds, and that the Universe is homogeneous and isotropic on large scales.

The importance of the Cosmological Principle in the development of the standard cosmological model resides in the fact that it allows us to rewrite the line element of space-time in a simple form in which the time dependence of the metric tensor is confined in a single function $a(t)$ of the cosmic time t, called the *Scale Factor*. When using spherical polar coordinates (r, θ, φ) for the space-like dimensions, the line element then takes the form:

---

[3] We always assume, unless specified otherwise, the Planck system of units in which $c = \hbar = 1$.

$$ds^2 = g_{\mu\nu} dx^\mu dx^\nu = dt^2 - a^2(t) \left[\frac{1}{1 + Kr^2} dr^2 + r^2 d\Omega^2 \right] , \tag{1.10}$$

where $d\Omega^2 = d\theta^2 + \sin^2\theta d\varphi^2$ is the line element on a sphere, and K is a constant which determines the curvature of the space-like hypersurfaces of constant cosmic time t:

$$\begin{aligned} K &= -1 &&: \text{negative curvature, hyperbolic geometry;} \\ K &= 0 &&: \text{no curvature, Euclidean geometry;} \\ K &= +1 &&: \text{positive curvature, spherical geometry.} \end{aligned}$$

This is known as the Friedmann-Lemaître-Robertson-Walker metric (hereafter, FLRW) (Friedman, 1922; Lemaître, 1931; Robertson, 1935; Walker, 1937), and by substituting its elements in the field equations 1.1 it is possible to derive two evolution equations for the scale factor $a(t)$, which will describe the dynamic evolution of the Universe as a whole:

$$\frac{\dot{a}^2}{a^2} = \frac{\kappa^2}{3} \left[\rho_k + \sum_i \rho_i \right] , \tag{1.11}$$

$$\frac{\ddot{a}}{a} = -\frac{\kappa^2}{6} \sum_i (\rho_i + 3p_i) , \tag{1.12}$$

where ρ_k is the curvature density:

$$\rho_k \equiv -\frac{3}{\kappa^2} \frac{K}{a^2} , \tag{1.13}$$

and ρ_i and p_i are respectively the energy density and the pressure of the different cosmic components. Eqs. 1.11,1.12 are known as the *Friedmann Equations* and completely determine the background time-evolution of the Universe.

Ordinary perfect fluids, such as matter or radiation, fulfill the condition:

$$\rho + 3p \geqslant 0 , \tag{1.14}$$

which is called the *Strong Energy Condition*. It is therefore clear that for this kind of fluids the Friedmann Equations will not have static solutions, since the second derivative of the scale factor $\ddot{a}$ is always negative.

1.2 The Cosmological Constant

The absence of static solutions for the Friedmann Equations led the same Einstein, in 1917, to revise the field equations of General Relativity 1.1 in order to allow a static Universe (Einstein, 1917). Such revision amounted to introducing a repulsive *Cosmological Constant* term in the field equations in order to balance the attractive pull of gravity.

The Cosmological Constant term is just a property of space-time itself, and does not depend on the spatial distribution of the energy density of all the different components that source the gravitational field of the Universe. Therefore, the natural place to add a Cosmological Constant Λ is in the Einstein Tensor $G_{\mu\nu}$:

$$\hat{G}_{\mu\nu} \equiv R_{\mu\nu} - \frac{1}{2}Rg_{\mu\nu} + \Lambda g_{\mu\nu} = G_{\mu\nu} + \Lambda g_{\mu\nu} \,. \tag{1.15}$$

It is important to notice that the introduction of the Cosmological Constant in the form described by Eq. 1.15 is not a purely *ad hoc* artifact. Indeed, a cosmological term of this form naturally arises in the context of General Relativity as a constant of integration of the theory. In fact, the most general action functional that it is possible to write in terms of the metric tensor $g_{\mu\nu}$ and of its first and second derivatives with respect to space-time coordinates x^{μ} has the form:

$$S = \frac{1}{2\kappa^2}\int d^4x\sqrt{-g}(R - 2\Lambda + \mathcal{L}) \,, \tag{1.16}$$

where g is the determinant of the metric tensor $g_{\mu\nu}$, $\mathcal{L}$ is the Lagrangian density of all the different energy fields in the Universe, and Λ is a constant. By applying the *Least Action Principle* to the general action 1.16 the field equations of General Relativity can be derived, having the form:

$$\hat{G}_{\mu\nu} = \kappa^2 T_{\mu\nu} \,, \tag{1.17}$$

with $\hat{G}_{\mu\nu}$ defined by Eq. 1.15. The usual field equations in the form 1.1 come from the choice to set to zero the value of Λ.

It is possible to formally move the Cosmological Constant term to the right-hand-side of the field equations, and to treat it as an additional fluid present in the Universe besides the components described by the Lagrangian density $\mathcal{L}$. In this case, the field equations will take the form:

$$G_{\mu\nu} = \kappa^2\hat{T}_{\mu\nu} \equiv \kappa^2\left[T_{\mu\nu} - \frac{\Lambda}{\kappa^2}g_{\mu\nu}\right] \,. \tag{1.18}$$

By applying the expression for the stress-energy tensor of a perfect fluid 1.6 to $\hat{T}_{\mu\nu}$ it is straightforward to find the formal energy density and pressure of the Cosmological Constant:

$$\rho_\Lambda = \frac{\Lambda}{\kappa^2}\,, \quad p_\Lambda = -\frac{\Lambda}{\kappa^2}\,, \tag{1.19}$$

from which the equation of state of the Cosmological Constant turns out to be:

$$w_\Lambda = \frac{p_\Lambda}{\rho_\Lambda} = -1\,. \tag{1.20}$$

This is an important feature of the Cosmological Constant, and determines its impact on the dynamics of the Universe. In fact, the condition 1.20 violates the Strong Energy Condition 1.14, and the Cosmological Constant is therefore able to counteract the gravitational pull of the other ordinary cosmic fluids, by changing the Friedmann equations to the following form:

$$\frac{\dot{a}^2}{a^2} = \frac{\kappa^2}{3}\left[\rho_k + \rho_\Lambda + \sum_i \rho_i\right]\,, \tag{1.21}$$

$$\frac{\ddot{a}}{a} = -\frac{\kappa^2}{6}\left[-2\rho_\Lambda + \sum_i (\rho_i + 3p_i)\right]\,. \tag{1.22}$$

Now the Eqs. 1.21,1.22 have static solutions for $K = +1$ (geometrically spherical, closed Universe) and for non-negative values of ρ_i, p_i, and Λ. Such static solutions are, however, unstable.

The discovery by E. Hubble, in 1929, of the expansion of the Universe (Hubble, 1929), removed the original motivation for the introduction of a Cosmological Constant, which was therefore abandoned, except for a periodically renewd interest, until the recent discovery, in 1998, of the accelerated expansion of the Universe by means of the study of the magnitude-redshift relation for Supernovae of Type Ia (Riess et al., 1998; Perlmutter et al., 1999).

Another important consequence of the value of the equation of state for the Cosmological Constant 1.20 is the fact that the Cosmological Constant energy density ρ_Λ does not change with the expansion of the Universe. In general, for a barotropic fluid (i.e. a fluid with $-1 \leqslant w \leqslant +1$), the energy density evolves with the scale factor of the Universe $a(t)$ following the relation:

$$\rho_i \propto a^{-3(1+w_i)}\,, \tag{1.23}$$

which for a Cosmological Constant implies:

$$\rho_\Lambda = \text{const.} \tag{1.24}$$

As a consequence of Eq. 1.24 one has that the energy density of the Cosmological Constant has always been (and will always be) the same throughout the whole expansion history of the Universe. Its value can therefore be considered a fundamental constant of Nature.

1.3 Observational Evidence of Dark Energy

In the last decade a large and constantly increasing amount of cosmological data from several independent datasets and from several different types of observations has revived the interest in the Cosmological Constant and in its phenomenology, after the long period of disregard that followed Hubble's discovery of the expansion of the Universe. We are not going to review here in detail the whole range of such observational probes, but we will nevertheless mention some crucial evidence in favor of the existence of a dark energy component.

The first observational evidence which started this revival process was a discrepancy between the large-scale angular correlation function of galaxies in the APM Galaxy Survey (Maddox et al., 1990) and the theoretical prediction based on the assumption of a flat cosmology dominated by cold dark matter. Efstathiou et al. (1990) showed that this discrepancy could be solved by assuming a flat low-density Universe with $\Omega_M h \approx 0.2$, where the missing energy for closure is given by a Cosmological Constant Λ.

In their conclusions, Efstathiou et al. (1990) invoked other independent probes, for example geometric tests of the deceleration of the expansion of the Universe, as possible ways to confirm or constrain the hypothesis of a positive Cosmological Constant dominating the present cosmic density. Such an independent confirmation came a few years later from the two independent studies made by the *Supernova Cosmology Project* (Riess et al., 1998) and the *High-z Supernova Search Team* (Perlmutter et al., 1999) on the relation between magnitude and redshift for the Supernovae of Type Ia (the redshift z is defined as $z \equiv a^{-1} - 1$). The two groups independently found an evolution of the supernovae magnitude with redshift not compatible with a decelerating Universe, and put observational constraints on the deceleration parameter q_0, defined as:

$$q_0 \equiv \left(-\frac{\ddot{a}a}{\dot{a}^2}\right)_0 = \left(-\frac{\dot{H}+H^2}{H^2}\right)_0 . \tag{1.25}$$

As we already stressed in the previous section, ordinary cosmic fluids that fulfill the *Strong Energy Condition* cannot account for a positive value of $\ddot{a}$, and therefore the case of a negative value of the deceleration parameter q_0 found in Riess et al. (1998) and Perlmutter et al. (1999) requires the assumption of the existence of a cosmic component whose equation of state does violate the *Strong Energy Condition.* If such component is assumed to be a Cosmological Constant, the deceleration parameter q_0 can be related to the fractional energy density in matter and in Cosmological Constant at $z = 0$:

$$q_0 = \frac{\Omega_{M,0}}{2} - \Omega_{\Lambda,0} \,, \tag{1.26}$$

and a constraint on q_0 therefore determines a linear relation in the $(\Omega_M, \Omega_\Lambda)$ plane at the present time.

An independent and almost orthogonal constraint in the same plane derives from the statistical analysis of the temperature anisotropies of the Cosmic Microwave Background (hereafter, CMB) radiation that was predicted by the Big Bang theory and discovered in 1965 by A. Penzias and R. Wilson (Penzias and Wilson, 1965). The angular power spectrum of the CMB temperature anisotropies – first detected by the COBE satellite in 1992 (Wright et al., 1992) – is in fact sensitive to the spatial geometry of the Universe and therefore constrains the total energy density. Such constraint derives mainly by the location of the first acoustic peak in the CMB temperature angular power spectrum as a function of multipole moment l.

The first acoustic peak is in fact related to the Hubble radius at the time of the last scattering, and the angular scale at which the peak is observed depends on the total energy density of the Universe through the relation:

$$l_{\rm peak} \simeq 220\,\Omega_{\rm TOT}^{-1/2} \,. \tag{1.27}$$

If again one assumes that the total energy density after the last scattering is given by the sum of matter and Cosmological Constant $\Omega_M + \Omega_\Lambda$, a determination of the angular position of the first acoustic peak results in a linear relation in the $(\Omega_M, \Omega_\Lambda)$ plane. The most recent CMB constraints on the total energy density of the Universe are (Komatsu et al., 2008):

$$\Omega_{TOT} = 1.005 \pm 0.006\,, \tag{1.28}$$

and therefore imply the relation $\Omega_M + \Omega_\Lambda \simeq 1$.

Together with the constraint on the total energy density of the Universe by means of the statistical properties of the CMB radiation, the independent observational determination of the fractional energy density in matter Ω_M constitutes another piece of evidence for the existence of a cosmic component that does not cluster on astrophysical scales. In fact, several different and independent determinations of Ω_M result in a fiducial value well below unity. All such different determinations of Ω_M rely on the clustering of matter due to its gravitational instability, and therefore a low value of Ω_M indicates the existence of an unclustered form of energy in the Universe.

For instance, the matter density can be estimated based on the analysis of the properties of Large Scale Structure, by the relation between the observed peculiar velocity field and the galaxy density distribution (Peacock et al., 2001), or independently from the evolution with redshift and mass of the cluster number counts, according to the *Press-Schechter Formalism* (Press and Schechter, 1974) (see e.g. Percival et al. (2001)). Other determinations of Ω_M based on gravitational lensing effects, or on the Sunyaev-Zeldovich effect for clusters of galaxies, all result in a low-matter-density Universe.

The combination of all these different observational constraints is capable of breaking the degeneracy between the two parameters Ω_M and Ω_Λ, and selects a confidence region in the plane $(\Omega_M, \Omega_\Lambda)$ at $z = 0$ around the point $(0.279, 0.721)$, as can be seen in Fig. 1.3, thus providing strong observational evidence for a *dark energy* component able to drive an accelerated expansion.

1.4 The Cosmological Constant Problems

As discussed in the previous paragraph, a huge and constantly increasing amount of data collected in the last decade and coming from several independent datasets indicates that roughly 75% of the total energy density in the Universe must be made of a dark energy

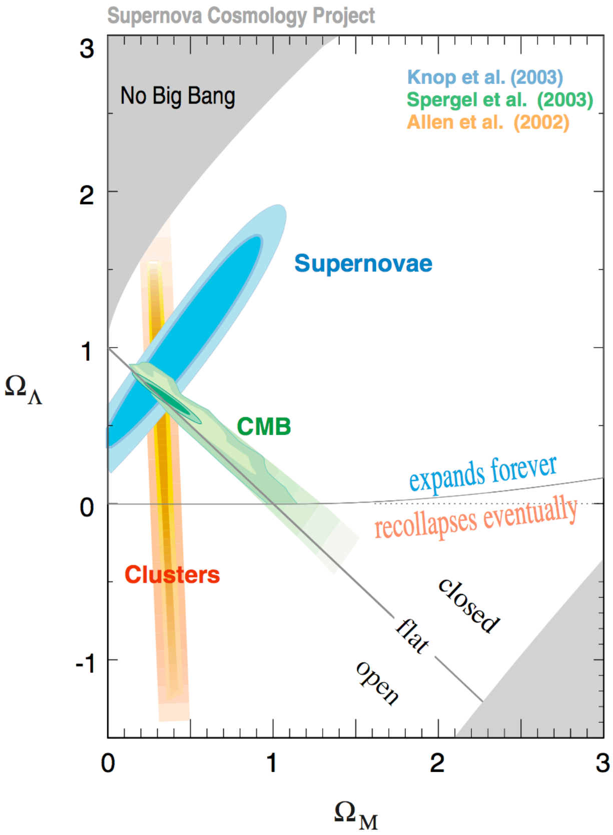

Figure 1.1: Complementary fiducial constraints in the parameter plane $(\Omega_M, \Omega_\Lambda)$ at $z = 0$, coming from the analysis of Supernovae Ia, CMB anisotropies, and Large Scale Structure properties. This figure is taken from the *Supernova Cosmology Project* website *http://supernova.lbl.gov/* (Perlmutter, 2008).

component that does not cluster on astrophysical scales. Such a cosmic component must at the present time have an equation of state w very close to -1 (Komatsu et al., 2008; Bean and Melchiorri, 2002; Jimenez et al., 2003; Hannestad and Mortsell, 2004). These features immediately suggest the Cosmological Constant, which has therefore been invoked as a natural explanation of the strong observational evidence for the existence of dark energy.

However, although the Cosmological Constant would appear as the most obvious candidate to fit the observational data, it presents us with two deep conceptual puzzles. As already discussed in the previous section, the study of the angular power spectrum of the CMB anisotropies indicates that the spatial geometry of the Universe is very close to Euclidean, and this finding constrains the total energy density to be very close to the critical density. As already stated in 1.28, the latest constraint on Ω_{tot} is (Komatsu et al., 2008):

$$\Omega_{\rm tot}(0) = \frac{\kappa^2 \rho_{\rm tot}(0)}{3H_0^2} = 1.005 \pm 0.006\,. \tag{1.29}$$

Therefore, from the measure of H_0 it is possible to infer the present value of the dark energy density ρ_Λ:

$$\rho_\Lambda = 0.75\,\rho_{\rm tot}(0) \sim \frac{3H_0^2}{\kappa^2} \sim 1.0 \cdot 10^{-10} {\rm erg\ cm}^{-3}\,. \tag{1.30}$$

The constancy of energy density for a Cosmological Constant (Eq. 1.24) implies therefore that the value 1.30 for ρ_Λ remains constant at all cosmological epochs. This means that also at the Planck time:

$$t_p \simeq \left(\frac{\hbar G}{c^5}\right)^{1/2} \simeq 10^{-43}{\rm s}\,, \tag{1.31}$$

which is considered to be the earliest moment of the evolution of the Universe which is accessible to our present theoretical understanding, ρ_Λ has the value 1.30. Therefore, at the time t_p, the ratio of the Cosmological Constant energy density ρ_Λ to the ambient density, which is the Planck density:

$$\rho_p \simeq \frac{c^5}{G^2 \hbar} \simeq 10^{113} {\rm erg\ cm}^{-3}\,, \tag{1.32}$$

would be of the order of:

$$\frac{\rho_\Lambda}{\rho_p} \sim 10^{-123} \tag{1.33}$$

in order to produce the observed value of ρ_Λ today.

This appears as an unreasonably fine tuning of the Cosmological Constant value, and has been therefore dubbed the *"Fine Tuning Problem"*.

Another consequence of Eq. 1.24 is the fact that the crossover of the Cosmological Constant energy density with respect to the matter density must have happened in the very recent past. In fact, given that the equation of state of matter is $w_M = 0$, from Eq. 1.23, one has that the matter energy density scales with the scale factor $a(t)$ as:

$$\rho_M \propto a^{-3}\,. \tag{1.34}$$

This means that the crossover must have taken place at a cosmological time corresponding to the scale factor a_* given by:

$$\rho_M(0) \cdot a_*^{-3} = \rho_\Lambda \rightarrow a_* = \left(\frac{\rho_\Lambda}{\rho_M(0)}\right)^{-1/3} \simeq 3^{-1/3} \simeq 0.7\,, \tag{1.35}$$

which corresponds to a redshift of $z_* \simeq 0.4$.

At earlier cosmological epochs the Cosmological Constant energy density was less and less important compared to the energy density of the other cosmic fluids; for instance, for any epoch earlier than the time at which the scale factor was $a \sim 0.14$ (corresponding to $z \sim 6$), the energy density in Λ was smaller than 10^{-3} times the critical density of the Universe.

This unexpected coincidence between the appearance of the Cosmological Constant and the present cosmological epoch is a second fundamental puzzle concerning the Cosmological Constant, and has been dubbed as the *"Coincidence Problem"*.

These two conceptual problems are not directly related with each other, but for the case of a Cosmological Constant they turn out to be indeed the same issue: by fine-tuning the value of Λ in the very early Universe to the huge degree of accuracy demanded to reproduce its present energy density, one gets automatically that the dark energy given by the Cosmological Constant comes to dominate the energy budget of the Universe at the time given by Eq. 1.35.

This is not the case, in general, for other models of dark energy, which can in different cases address either one or the other of these two issues. As will be described in the next Chapters, a dark energy model capable of solving both of these two problems at the same time turns out to be a very challenging task.

Chapter 2

Dynamic models of Dark Energy

2.1 Quintessence

The need to address the Fine Tuning and the Coincidence problems introduced in the previous Chapter is at the origin of the investigation of dynamic dark energy models. By allowing variability in time of the dark energy component one introduces an additional degree of freedom in the theory, which could provide a way to escape the constraints that challenge the Cosmological Constant, and could help to reconcile the model with the observed value of the dark energy density.

Nevertheless, it is worth remembering that dynamic models of dark energy were introduced in 1988 by Wetterich (Wetterich, 1988) and Ratra & Peebles (Ratra and Peebles, 1988), well before the first observational evidence in favor of a dark energy dominated Universe.

The simplest models of dynamic dark energy are based on the concept of a *Classical Scalar Field*, a physical entity that can be described, at any point of space-time, by a single number. A Scalar Field – which we denote with ϕ – moving in a self-interaction potential can be described, in its most general form, by a lagrangian density $p(\phi, \partial_\mu \phi)$, a function of the scalar field itself and of its 4-derivative. The requirement that p be a Lorentz-invariant implies that the dependence on the 4-derivative must be expressed in a scalar form. The simplest scalar quantity derivable from the Lorentz vector $\partial_\mu \phi$ is its self contraction, which can be written as [1]:

$$\chi \equiv -\frac{1}{2} g^{\mu\nu} \partial_\mu \phi \partial_\nu \phi = \frac{1}{2} \dot{\phi}^2 \,, \tag{2.1}$$

and represents the kinetic energy of the scalar field. The last equality of Eq. 2.1 derives from the assumption that the scalar field is spatially homogeneous.

---

[1] We always denote with an overdot a derivation with respect to the cosmic time t.

The simplest possible form for the function p contains therefore a kinetic term and a potential term, and can be written as:

$$p = \frac{1}{2}\dot{\phi}^2 - V(\phi) = \chi - V(\phi)\,, \tag{2.2}$$

where $V(\phi)$ is any regular function of the scalar field. The expression 2.2 defines what is usually called *Quintessence* (Wetterich, 1988), and determines, through the definition of a specific potential function $V(\phi)$, the dynamic evolution of the scalar field. Introducing such a scalar field component in the general action functional of the Universe 1.16 in place of the Cosmological Constant term brings to the following expression:

$$S = \frac{1}{2\kappa^2}\int d^4x\sqrt{-g}\left[R + \frac{1}{2}\dot{\phi}^2 - V(\phi) + \mathcal{L}\right]\,. \tag{2.3}$$

Applying now the Least Action Principle to the action 2.3 it is possible to derive the form of the scalar field stress-energy tensor, which allows us to identify expressions for the energy density and the pressure of the perfect fluid associated to the scalar field ϕ. These are:

$$\rho_\phi = \frac{1}{2}\dot{\phi}^2 + V(\phi)\,, \quad p_\phi = p(\phi,\chi) = \frac{1}{2}\dot{\phi}^2 - V(\phi)\,. \tag{2.4}$$

The equation of state w_ϕ of the scalar field fluid will therefore take the form:

$$w_\phi = \frac{\frac{1}{2}\dot{\phi}^2 - V(\phi)}{\frac{1}{2}\dot{\phi}^2 + V(\phi)}\,, \tag{2.5}$$

and this expression shows the dynamic nature of a dark energy component represented by a scalar field ϕ with respect to the static behavior of a Cosmological Constant Λ: the equation of state of the scalar field takes the value of -1 (which corresponds, from Eq. 1.23, to a constant energy density) only for the limiting case of a static or quasi-static configuration ($\dot{\phi}^2 \ll V(\phi)$), otherwise being always larger than -1, and so requiring evolution of the scalar field energy density with the expansion of space.

Such a dynamic nature is the main reason why a scalar field dark energy can in principle solve the Fine Tuning Problem: a very low dark energy density at the present time would not necessarily imply a very low dark energy density at the Planck time, because the dark energy density can evolve in time like the energy density of all the other cosmic fluids.

2.2 Phase-Space analysis

In order to analyze the dynamic evolution of a cosmological model with such a scalar field dark energy, Copeland et al. (1998) investigated the dynamics of a flat FLRW cosmological model with a scalar field subject to an exponential self-interaction potential:

$$V(\phi) = V_0 e^{-\mu\kappa\phi} \tag{2.6}$$

and with a barotropic fluid with equation of state $p_\eta = \eta\rho_\eta$. In this case, the evolution equations for the system are given by:

$$\begin{aligned} \dot{H} &= -\frac{\kappa^2}{2}\left(\rho_\eta + p_\eta + \dot{\phi}^2\right)\,, && (2.7)\\ \dot{\rho}_\eta &= -3H\left(\rho_\eta + p_\eta\right)\,, && (2.8)\\ \ddot{\phi} &= -3H\dot{\phi} - \frac{dV}{d\phi}\,. && (2.9) \end{aligned}$$

The system of Eqs. 2.7-2.9 is then subject to a constraint given by the first Friedmann equation 1.11, which in this case reads:

$$H^2 = \frac{\kappa^2}{3}\left(\rho_\eta + \frac{1}{2}\dot{\phi}^2 + V\right)\,. \tag{2.10}$$

The method introduced by Copeland et al. (1998) consists in using dimensionless variables in terms of which the system of Eqs. 2.7-2.9 and its Friedmann constraint 2.10 can be rewritten as a plane autonomous system.

Such dimensionless variables are defined as:

$$x \equiv \frac{\kappa\dot{\phi}}{\sqrt{6}H} \quad ; \quad y \equiv \frac{\kappa\sqrt{V}}{\sqrt{3}H}\,. \tag{2.11}$$

By using these two variables the dimensionless energy density of the scalar field can be expressed in the form:

$$\Omega_\phi \equiv \frac{\rho_\phi}{\rho_{crit}} = \frac{\kappa^2\left[\frac{1}{2}\dot{\phi}^2 + V(\phi)\right]}{3H^2} = x^2 + y^2\,, \tag{2.12}$$

and it is possible to identify the contribution given to the total density by the kinetic and potential terms of the scalar field lagrangian, as:

$$\Omega_{\phi,\mathrm{kin}} = x^2 \quad ; \quad \Omega_{\phi,\mathrm{pot}} = y^2\,. \tag{2.13}$$

Furthermore, by the assumption of flatness of the Universe given by the constraint Eq. 2.10, the total energy density in the barotropic fluid can be written as:

$$\Omega_\eta = 1 - x^2 - y^2\,. \tag{2.14}$$

Also the equation of state of the scalar field can be expressed in terms of the variables x and y as:

$$w_{\phi} = \frac{x^2 - y^2}{x^2 + y^2} \,. \tag{2.15}$$

Rewriting the Eqs. 2.7-2.9 in terms of these new variables results in the autonomous system:

$$\begin{aligned} x' &= -\frac{3}{2}x + \mu\sqrt{\frac{3}{2}}y^2 + \frac{3}{2}x\left[x^2 - y^2 + \eta(1 - x^2 - y^2)\right] \,, \qquad (2.16) \\ y' &= -\mu\sqrt{\frac{3}{2}}xy + \frac{3}{2}y\left[1 + x^2 - y^2 + \eta(1 - x^2 - y^2)\right] \,, \qquad (2.17) \end{aligned}$$

where a prime indicates a derivative with respect to the logarithm of the scale factor, $\alpha \equiv \ln a$. The constraint:

$$0 \leqslant x^2 + y^2 \leqslant 1 \tag{2.18}$$

coming from the Friedmann equation 2.10 indicates that the evolution of the system is completely described by the dynamic evolution of the variables (x, y) within the unitary disc. Furthermore, since the system is symmetric under the reflection $(x, y) \rightarrow (x, -y)$ and under time inversion $t \rightarrow -t$ (since the lower half-disk $y < 0$ corresponds to contracting solutions), it is always sufficient to consider the upper half-disk $y \geqslant 0$.

For this autonomous system we can now derive the *critical points* in the upper half-disk, defined as the points for which $x' = 0$ and $y' = 0$. Depending on the values of μ and η we can have for the system 2.16-2.17 up to five of these critical points. Their stability can be analyzed by means of an eigenvalue analysis (as discussed in detail in Copeland et al. (1998)) and will also obviously depend on the values of the parameters μ and η. The condition that defines a critical point ($x' = 0$, $y' = 0$) implies that on a critical point the equation of state of the scalar field will stay constant (see Eq. 2.15), and this corresponds to the definition of a *Scaling Solution*. Therefore a critical point always corresponds to a scaling solution. The five critical points for this system are listed in Table 2.1 together with the parameter space regions for their existence and stability and with the value of the scalar field equation of state, where for convenience we have set $\Gamma \equiv \eta + 1$.

x	y	Existence	Stability	Ω_ϕ	w_ϕ
0	0	$\forall\mu\,,\eta$	Saddle point for $-1 \leqslant \eta \leqslant 1$	0	Undefined
1	0	$\forall\mu\,,\eta$	Unstable node for $\mu < \sqrt{6}$ Saddle Point for $\mu > \sqrt{6}$	1	1
-1	0	$\forall\mu\,,\eta$	Unstable node for $\mu > \sqrt{6}$ Saddle Point for $\mu < \sqrt{6}$	1	1
$\frac{\mu}{\sqrt{6}}$	$\left[1-\frac{\mu^2}{6}\right]^{1/2}$	$\mu^2 < 6$	Stable node for $\mu^2 < 3\Gamma$ Saddle Point for $3\Gamma < \mu^2 < 6$	1	$-1+\frac{\mu^2}{3}$
$\sqrt{\frac{3}{2}}\frac{\Gamma}{\mu}$	$\sqrt{\frac{3}{2}}\left[\frac{(2-\Gamma)(\Gamma)}{2\mu^2}\right]^{1/2}$	$\mu^2 > 3\Gamma$	Stable node for $3\Gamma < \mu^2 < \frac{24\Gamma^2}{(9\Gamma-2)}$ Stable Spiral for $\mu^2 > \frac{24\Gamma^2}{(9\Gamma-2)}$	$\frac{3\Gamma}{\mu^2}$	η

Table 2.1: Table of the five critical points for the system 2.16-2.17 with the corresponding existence conditions and stability conditions, as determined by an analysis of the eigenvalues of the system (see Copeland et al. (1998)). The last two columns contain respectively the energy density of the scalar field Ω_ϕ and its equation of state w_ϕ for each critical point.

2.3 The properties of Scaling Solutions

All the critical points listed in Table 2.1 correspond to scalar field Scaling Solutions, according to the definition of a Scaling Solution as a solution of the dynamic equation for the scalar field (Eq. 2.9) that keeps constant the value of the equation of state w_ϕ. We can analyze the properties of all these points according to their parameter-space regions of existence and stability.

The two points for which the Universe is dominated by the scalar field kinetic energy, which are the points $(x = \pm 1\,, y = 0)$, correspond to a scalar field with a *stiff* equation of state $w_\phi = 1$, and are never stable. Therefore they can play a role only at early times, but they will not be relevant for the late-time dark energy phenomenology.

The behavior of the fluid dominated critical point $(x = 0\,, y = 0)$ is more surprising. The stability analysis shows in fact that such a point is never stable for any value of η in the interval $-1 < \eta \leqslant 1$, which means that, unless the barotropic fluid is a Cosmological Constant itself $(\eta = -1)$, the energy density in the scalar field can never vanish with respect to the energy density in the other fluids present in the Universe at late times.

The two remaining points are the only ones that have stability regions in the parameter space (μ, η), and that can therefore represent late-time attractor solutions. One of them, the one which has $\Omega_\phi = 1$ (i.e. the fourth point of Table 2.1), represents a scalar field dominated solution, which is stable for sufficiently flat potentials ($\mu^2 < 6$), and gives rise to a power-law inflationary expansion for $\mu^2 < 2$, as it was found in Lucchin and Matarrese (1985). This phase-space analysis shows that this kind of solution is also a late time attractor in presence of a barotropic fluid for $\mu^2 < 3(\eta + 1)$.

However, the most interesting situation for the solution of the Fine Tuning Problem related to the observational features of the dark energy component is given by the region of the parameter space where $\mu^2 > 3(\eta + 1)$. In this case, the only stable critical point is given by a completely different type of scaling solution, represented by the last point in Table 2.1, for which none of the two components completely dominates the energy density of the Universe. For this solution, in fact, the scalar field and the barotropic fluid evolve keeping a constant ratio of their energy densities, with $\Omega_\phi = 3(\eta + 1)/\mu^2$. The constancy of the ratio Ω_ϕ/Ω_η is a consequence of the fact that for such a scaling solution the constant value kept by the scalar field equation of state corresponds to the value of the equation of state of the barotropic fluid: $w_\phi = \eta$. This implies that the two components will scale in the same way with the expansion of the Universe:

$$\rho_i = a^{-3(1+w_i)} \, . \tag{2.19}$$

This solution was first found in Wetterich (1988), and takes the name of *tracking* scaling solution – or *tracker* – for its feature of mimicking the behavior of the dominating fluid of the Universe by adjusting the scalar field equation of state to the value of the dominant component.

The importance of the existence of such attractor solution for a wide region of the parameter space ($\mu^2 > 3\,[\eta + 1]$) in easing the fine tuning problem is clear: for a wide range of possible parameter values of the model, and for different types of barotropic fluids (e.g. matter or radiation), the evolution of the Universe will be attracted towards a trajectory on which the scalar field scales like the dominant barotropic component and tracks its evolution. This means that during radiation domination, in the early Universe, we can have a scalar field that scales as radiation (i.e. as a^{-4}), and afterwards, during matter domination, the scalar field will scale as matter (i.e. as a^{-3}). It is therefore not necessary anymore to fine-tune the value of the dark energy density in the early Universe with a huge precision because the scalar field can start with a high density in the early Universe and dilute with the expansion to have the low observed energy density today, the only constraint being the value of $\Omega_\phi = 3(\eta + 1)/\mu^2$ during radiation and matter domination, which has to be compatible with observational constraints on the amount of early dark energy (Xia and Viel, 2009).

A qualitative comparison of the evolution of energy densities with the expansion of the Universe which shows the main advantage of such *tracking* scaling solution as compared to the Cosmological Constant in easing the Fine Tuning Problem is given by Fig. 2.1.

2.4 Shortcomings of uncoupled dynamic Dark Energy

The most relevant feature of the *tracking* behavior of the last critical point of Table 2.1 for the system 2.16-2.17 is the possibility to bring the dark energy density from high values in the early Universe to the low value observed today, without needing to fine-tune the parameters of the model and the initial conditions for the scalar field: the *tracking* scaling solution is stable for a large region of the parameter space, and because of the barotropic condition on the index η ($-1 \leqslant \eta \leqslant 1$) the stability region for such solution results in a single condition on the slope of the exponential self-interaction potential for the scalar field: $\mu^2 > 6$.

The stability of this solution ensures that the system will fall onto the *tracker* no matter which are the initial conditions for the scalar field ϕ and its time derivative $\dot{\phi}$.

However, on the other hand, observational constraints coming from the abundance of primoridal elements predicted by the Big Bang Nucleosynthesis model and from the growth rate of cosmic structures during matter domination, as well as from other independent observational probes, set an upper limit on the amount of early dark energy during radiation and matter domination. If we indicate these values with $\Omega_{\phi,r}$ and $\Omega_{\phi,m}$ respectively, then the relation with the potential slope implies:

$$\begin{aligned} \Omega_\phi(\mathrm{rad}) &= \frac{3\Gamma}{\mu^2} = \frac{4}{\mu^2} < \Omega_{\phi,r} \quad \rightarrow \quad \mu^2 > \frac{4}{\Omega_{\phi,r}}\,, && (2.20) \\ \Omega_\phi(\mathrm{mat}) &= \frac{3\Gamma}{\mu^2} = \frac{3}{\mu^2} < \Omega_{\phi,m} \quad \rightarrow \quad \mu^2 > \frac{3}{\Omega_{\phi,m}}\,. && (2.21) \end{aligned}$$

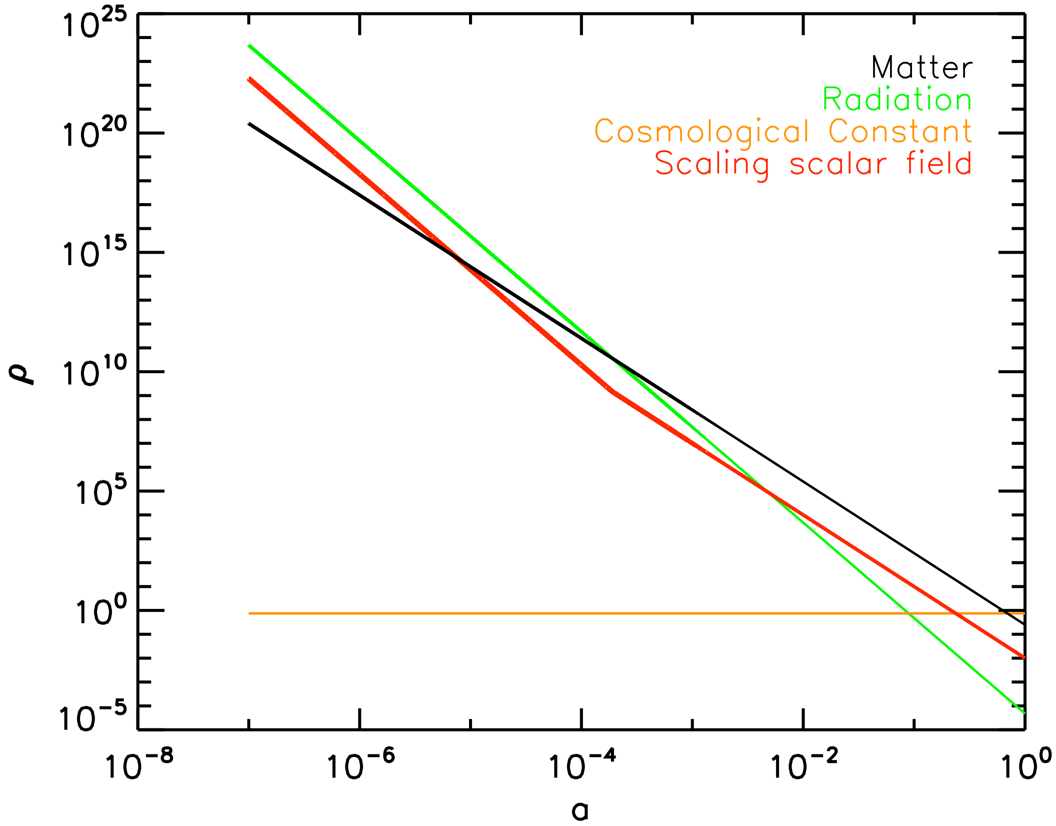

Figure 2.1: Evolution with the scale factor a of the energy densities of different types of fluid: a Cosmological Constant (orange line) keeps a constant energy density during all the expansion history of the Universe, while radiation (green line) and matter (black line) scale respectively as a^{-4} and a^{-3}. A scalar field on a *tracking* scaling solution like the one given by the last critical point of Table 2.1 follows the behavior of the dominant barotropic fluid, and therefore scales as a^{-4} during radiation domination, and automatically switches to a^{-3} at equivalence. This behavior can in principle overcome the *Fine Tuning* problem by removing the need to set the initial dark energy density to unnaturally small values in the early Universe; however, as a consequence of the stability of the *tracking* scaling solution, it does not allow a late time dark energy domination.

In any case, it is known from observational constraints that dark energy must be subdominant during the whole radiation dominated epoch and for a large fraction of matter domination, without exceeding few percent of the total energy budget of the Universe: $\Omega_{\phi,r}\,,\Omega_{\phi,m} \leqslant 2 \sim 3 \cdot 10^{-2}$ (Xia and Viel, 2009).

On the other hand, we measure today an energy density for the dark energy component which is about 75% of the total energy density of the Universe. Therefore, although the *tracking* scaling solution can ease the Fine Tuning problem, it cannot explain the present ratio of energy densities in the Universe, due to the fact that the stability of the *tracker* will forever keep the system on a solution in which the scalar field must be subdominant in order to be compatible with high redshift observational constraints.

This can be seen as a good motivation to try to extend the model in order to account for late time dark energy domination. The introduction of a direct interaction between the dark energy scalar field and other cosmic fluids – that will be extensively discussed in the next Chapters – is one possible way to perform such an extension.

Such a tentative and repeated extension of the theoretical model by introducing a new degree of freedom each time a new conceptual puzzle shows up (as happened with the introduction of a time variation of the dark energy to address the Fine Tuning issue that faces the Cosmological Constant) might look as a sort of "epicycle process", hiding a radically different and deeper explanation of the dark energy physics. However, it is worth remembering here that a direct interaction between the dark energy component (whatever it might be) and the other fluids in the Universe, in particular the dark matter fluid, is not sufficiently constrained by observations to be ruled out, as we will discuss in the first section of Chapter 3. This therefore represents a possibility which deserves further investigation.

Chapter 3

Interacting Dark Energy

3.1 Motivations for interacting dark energy

As we have discussed in detail in the previous Chapter, the introduction of the new degree of freedom consisting in the possibility of time variation of the dark energy density, by means of the dynamic evolution of a self-interacting and minimally coupled (i.e. interacting with the rest of the Universe only gravitationally) scalar field, offers a chance to mitigate the serious conceptual problem associated with the extremely fine tuning which is required to accommodate observations with a Cosmological Constant. The dynamic solution of such problem, based on the *tracking* property 2.19 runs, however, into a new fundamental problem since it cannot produce a crossover between a fluid (radiation or matter) dominated epoch, where the dark energy scalar field tracks the evolution of the dominant component keeping a subdominant energy density, and a dark energy dominated epoch at late times. This is due, as we have stressed in the previous Chapter, to the stability of the *tracking* scaling solution.

Therefore, unless one wants to completely abandon the dark energy hypothesis and assume that the observed phenomena – the acceleration of the expansion of the Universe (Riess et al., 1998; Perlmutter et al., 1999; Astier et al., 2006), the observed flatness of the spatial geometry (Komatsu et al., 2008), the inferred low matter density (Peacock et al., 2001; Percival et al., 2001; Grego et al., 2001), or a detection of the Integrated-Sachs-Wolfe effect (Giannantonio et al., 2008) – that suggest the existence of a dark energy component can in reality be explained by some completely different mechanism (as e.g. modifications of gravity (Capozziello and Francaviglia, 2008; Rubakov and Shaposhnikov, 1983; Bekenstein, 2004), backreaction effects (Kolb et al., 2005), inhomogeneous cosmologies (Chuang et al., 2008; Paranjape and Singh, 2006)), it is necessary to look for possible extensions of the simple model described in the previous Chapter, in order to solve this new fundamental problem of the theory.

One possible way to extend the basic scenario is to try to build models where the *tracking* solution is not so perfectly stable, and the system is perturbed such that after an appropriately extended *tracking* epoch the system is kicked out from the *tracking* solution and falls into the only other attractor, given by the scalar field dominated solution (fourth point in Table 2.1). This type of extension can be performed either by changing the form of the self-interaction potential $V(\phi)$ (e.g with the SUGRA potential proposed in Brax and Martin (1999)), or, more radically, by allowing for more general forms of the lagrangian density $p(\phi, \chi)$ than the simple Quintessence discussed until now (Armendariz-Picon et al., 2000; Amendola et al., 2006).

However, as shown in Amendola et al. (2006), there is no possible choice of the lagrangian density $p(\phi, \chi)$ in the context of single-field minimally-coupled dark energy models that could feature two subsequent *tracking* solutions, one having a subdominant dark energy fraction, and the other having the observed value of Ω_ϕ at the present epoch, thereby solving at the same time the Fine Tuning and the Coincidence problems.

Another possible extension consists in dropping the assumption that the scalar field ϕ is minimally coupled, which means assuming that ϕ can directly interact with other fields in the Universe. A first motivation for considering interacting dark energy models thus resides in the need to address the problem of the exit from a *tracking* cosmic evolution with a subdominant dark energy component. A direct interaction between a scalar field and ordinary matter (i.e. the baryons) would be subject to the constraints that affect any scalar-tensor theory, for instance the Brans-Dicke (Brans and Dicke, 1961) extension of General Relativity, so that the coupling strength would therefore be tightly constrained to very small values. However, as first pointed out in Damour et al. (1990), a non-universal coupling of the dark energy scalar field ϕ involving only cold dark matter would escape such constraints and would allow for a significantly larger value of the interaction strength, thus opening room for new interesting phenomenology.

Indeed, in absence of specific constraints capable of ruling out this type of non-universal coupling, there is no reason to assume that the scalar field ϕ has to be minimally coupled, and the possibility of investigating the scalar field phenomenology hidden beyond such an unnecessary assumption constitutes a further motivation for our study. As we will mention in Chapter 6, the present bounds on the interaction between dark energy and cold dark matter are mainly based on the effects that such interaction would have on CMB properties (Bean et al., 2008), and leave enough room for potentially detectable new physics.

Finally we notice that, although the standard "concordance" cosmological model based on the ΛCDM paradigm – i.e. based on the assumption that the dark energy component is indeed given by a cosmological constant Λ – is very successful in predicting the observed properties of the Universe, in a few cases it nevertheless runs into conflict with observations.

In particular, one of the longstanding problem of the ΛCDM picture is the overpredicted abundance of substructures within cold dark matter halos with respect to the observed number of satellites of galactic halos in the Local Group, first pointed out by Klypin et al. (1999) and Moore et al. (1999)(see also Springel et al. (2008)).

Furthermore, the universal density profile of cold dark matter halos within the ΛCDM scenario shows an exceedingly steep rise of the overdensity in the central region, giving rise to the longstanding so-called "cusp-core" problem (Navarro et al., 1996, 1997).

Finally, the observed baryon fraction in large galaxy clusters (Allen et al., 2004; Vikhlinin et al., 2006; LaRoque et al., 2006) is found to be low as compared to the universal cosmic value that can be inferred by CMB analysis (Komatsu et al., 2008), and this discrepancy is also not easily addressed in the context of a ΛCDM cosmology.

All these different examples of tensions between the predictions of the ΛCDM "concordance" model and specific types of observations constitute another motivation for an investigation of cosmological models that go beyond the standard scenario and also beyond the simplest possible models of dynamic dark energy.

As we will discuss in Chapter 6, our investigation of coupled dark energy models shows that a direct interaction between the dark energy scalar field and the cold dark matter fluid, in the fashion that will be extensively described in this Chapter, produces effects that go in the direction of alleviating several of the problems mentioned here.

3.2 Basic equations of an interacting dark energy component

If we assume General Relativity to be the correct theory for the gravitational interaction at any scale, then we also assume that the Einstein field equations 1.1 hold, together with all their properties.

One of these properties, deriving as a direct consequence of the General Covariance Principle (Weinberg, 1972), constrains the Einstein Tensor $G_{\mu\nu}$ to fulfill the vector equation:

$$\nabla_{\mu} G^{\mu}_{\nu} = 0 \,, \tag{3.1}$$

which constitutes a system of four differential equations going under the name of *Contracted Bianchi Identities*, as already discussed in Chapter 1.

Due to the tensor character of the field equations 1.1, the same constraint needs to hold for the total stress-energy tensor of the Universe $T_{\mu\nu}$, so:

$$\nabla_{\mu} T^{\mu}_{\nu} = 0 \,. \tag{3.2}$$

The vector equation 3.2 represents the total stress-energy conservation for the Universe as a whole. However, the total stress-energy tensor $T_{\mu\nu}$ is in general the sum of several different stress-energy tensors for the different components that are present in the Universe which, according to the present understanding of observational data, should be at least five: radiation, neutrinos, cold dark matter, baryons, and dark energy. This means that General Covariance will apply to the sum of all these components, but no constraint like 3.2 will apply to the stress-energy tensors of the individual components, provided the total $T_{\mu\nu}$ keeps obeying Eq. 3.2. Therefore, for each component i present in the Universe, the covariant derivative of its own stress-energy tensor can be any 4-vector source $Q^{(i)}_{\nu}$:

$$\nabla_{\mu} T^{(i)\mu}_{\nu} = Q^{(i)}_{\nu} \,, \tag{3.3}$$

provided that all such source vectors $Q^{(i)}_{\nu}$ sum up to zero:

$$\sum_{i} Q^{(i)}_{\nu} = 0 \,. \tag{3.4}$$

It is then possible to assume that the scalar field ϕ and the cold dark matter fluid interact with each other through the presence of such a source term in their respective covariant conservation equations [1]:

$$\nabla_\mu T^{(\phi)\mu}_\nu = -Q_\nu \, ; \quad \nabla_\mu T^{(c)\mu}_\nu = Q_\nu \, . \tag{3.5}$$

The pair of equations 3.5 is compatible with the constraint 3.2 and introduces an interaction term between the two dark fields.

In Wetterich (1995) and later in Amendola (2000) it was proposed to assume for the source term Q_ν the form:

$$Q_\nu \equiv -\kappa\beta(\phi) T^c \nabla_\nu \phi \, , \tag{3.6}$$

where T^c is the trace of the cold dark matter stress-energy tensor, and $\beta(\phi)$ is the coupling function that sets the strength of the interaction (for most of this work we will assume $\beta(\phi)$ to be a constant and we will indicate it just as β).

By computing the time-like component of the equations 3.5 with the source term 3.6 it is now possible to derive the new coupled evolution equations for the two interacting fluids, generalizing Eqs. 2.8-2.9:

$$\begin{aligned} \dot{\rho}_c + 3H\rho_c &= -\kappa\beta\rho_c\dot{\phi} \, , &(3.7)\\ \ddot{\phi} + 3H\dot{\phi} + \frac{dV}{d\phi} &= \kappa\beta\rho_c \, . &(3.8) \end{aligned}$$

The coupling terms that appear in Eqs. 3.7-3.8, or equivalently in 3.6, are not an arbitrary assumption but can be derived by a generalized form for the action functional of the Universe in which the mass term of the cold dark matter field (here denoted as ψ) is assumed to be a function of the scalar field ϕ:

$$S = \frac{1}{16\pi G} \int d^4x \sqrt{g} \left[R - \frac{1}{2} g^{\mu\nu} \partial_\mu \phi \partial_\mu \phi - V(\phi) - m(\phi)\bar{\psi}\psi + \mathcal{L}_{kin}[\psi] \right] \, , \tag{3.9}$$

for the case in which the functional dependence of $m(\phi)$ is an exponential:

$$m(\phi) = m_0 e^{-\kappa\beta(\phi)\phi} \, . \tag{3.10}$$

Therefore, if we now assume a simplified model of the Universe in which we discard the baryons and the neutrino components, and we assume that the only three fluids contributing to the energy budget are the dark energy scalar field ϕ, the cold dark matter fluid, and the radiation component (denoted as r), we can rewrite the system of equations

---

[1] From now on we will use the index c to indicate cold dark matter in all equations for quantities that refer to the cold dark matter fluid

2.8-2.9 for the interacting case, which will be given by Eqs. 3.7-3.8 and by the usual Euler equation for the relativistic fluid:

$$\begin{aligned} \dot{\rho}_c + 3H\rho_c &= -\kappa\beta\rho_c\dot{\phi}\,, && (3.11) \\ \ddot{\phi} + 3H\dot{\phi} + \frac{dV}{d\phi} &= \kappa\beta\rho_c\,, && (3.12) \\ \dot{\rho}_r + 4H\rho_r &= 0\,. && (3.13) \end{aligned}$$

By integrating the coupled equations 3.11 and 3.13 we can derive the scaling laws for cold dark matter and radiation in this interacting dark energy cosmological model:

$$\begin{aligned} \rho_c &\propto a^{-3}e^{-\kappa\beta\phi}\,, && (3.14) \\ \rho_r &\propto a^{-4}\,, && (3.15) \end{aligned}$$

from which we can infer that while the relativistic fluid scales in its usual way with the scale factor, the interacting cold dark matter fluid does not simply dilute as the inverse of the volume, but has an additional evolution term deriving from its interaction with the scalar field ϕ. As will be discussed in considerable detail in the next Chapters, this correction term is one of the most striking features of models of direct interaction between the dark energy scalar field and other cosmic fluids.

Finally, to close the system of equations describing the simplified model of the Universe introduced above, we can rewrite the Friedmann constraint 2.10 taking into account the new scaling law 3.14 of the cold dark matter fluid:

$$H^2 = \frac{\kappa^2}{3}\left[\rho_c(0)a^{-3}e^{-\kappa\beta\phi} + \rho_r(0)a^{-4} + \frac{1}{2}\dot{\phi}^2 + V(\phi)\right]\,. \tag{3.16}$$

3.3 Phase space analysis for coupled quintessence

In Amendola (2000) the dynamics of the system 3.11-3.13 has been analyzed by means of a generalization of the autonomous system approach introduced by Copeland et al. (1998) and discussed in Chapter 2.

In this case, to perform such analysis it is necessary to introduce three dimensionless variables in order to rewrite the problem in the form of an autonomous system:

$$x \equiv \frac{\kappa\dot{\phi}}{\sqrt{6}H}\,; \quad y \equiv \frac{\kappa\sqrt{V}}{\sqrt{3}H}\,; \quad z \equiv \frac{\kappa\sqrt{\rho_r}}{\sqrt{3}H}\,, \tag{3.17}$$

where the energy densities of the kinetic and the potential part of the scalar field are still given by x^2 and y^2 respectively, and where z^2 represents the energy density of radiation:

$$\Omega_r \equiv \frac{\kappa^2 \rho_r}{3H^2} = z^2 \,, \tag{3.18}$$

while the cold dark matter energy density is given by the Friedmann constraint 3.16:

$$\Omega_c = 1 - \Omega_\phi - \Omega_r = 1 - x^2 - y^2 - z^2 \,. \tag{3.19}$$

For the same case of an exponential potential 2.6 already discussed in the uncoupled case, by using these variables the system can be recast in the form:

$$\begin{aligned} x' &= \left(\frac{z'}{z} - 1\right) x + \sqrt{\frac{3}{2}} \mu y^2 + \sqrt{\frac{3}{2}} \beta (1 - x^2 - y^2 - z^2) \,, && (3.20) \\ y' &= -\sqrt{\frac{3}{2}} \mu x y + y \left(2 + \frac{z'}{z}\right) \,, && (3.21) \\ z' &= -\frac{z}{2} (1 - 3x^2 + 3y^2 - z^2) \,, && (3.22) \end{aligned}$$

where again a prime denotes a derivative with respect to the logarithm of the scale factor, $\alpha \equiv \ln a$. Also in this case the system has some symmetries: it is invariant under a transformation $(x, y, z) \to (x, -y, -z)$ and under inversion of time $t \to -t$.

Furthermore, the Friedmann constraint 3.16 allows acceptable trajectories only within the unitary sphere $x^2 + y^2 + z^2 \leqslant 1$. Therefore it will be sufficient to study the system in the quarter of the unitary sphere with positive y and z. Following the same argument as in Chapter 2 we can look for the critical points of the system ($x' = 0$, $y' = 0$, $z' = 0$) in such a region and identify the *Scaling Solutions*. On the scaling solutions, the Universe will expand with a rate given by:

$$a \propto t^p \,, \quad p \equiv \frac{2}{3(1 + w_{\text{eff}})} \,, \tag{3.23}$$

where the effective equation of state of the Universe w_{eff} is defined as:

$$w_{\text{eff}} \equiv \Omega_\phi w_\phi + \Omega_r w_r = x^2 - y^2 + \frac{z^2}{3} \,, \tag{3.24}$$

and therefore an accelerated solution which could reproduce the observed accelerated expansion of the Universe (Riess et al., 1998; Perlmutter et al., 1999) will require a value $w_{\text{eff}} < -1/3$.

The system 3.20-3.22 has up to 15 critical points, of which only 8 are in the quarter

Point	x	y	z	Ω_ϕ	w_{eff}	w_ϕ
I	$\frac{\mu}{\sqrt{6}}$	$\left(1-\frac{\mu^2}{6}\right)^{1/2}$	0	1	$-1+\frac{\mu^2}{3}$	$-1+\frac{\mu^2}{3}$
II	$\sqrt{\frac{8}{3}}\frac{1}{\mu}$	$\frac{2}{\sqrt{3}\|\mu\|}$	$\left(1-\frac{4}{\mu^2}\right)^{1/2}$	$\frac{4}{\mu^2}$	$\frac{1}{3}$	$\frac{1}{3}$
III	$-\frac{\sqrt{3}}{\sqrt{2}(\beta-\mu)}$	$\frac{(g-9)^{1/2}}{\sqrt{6}\|\beta-\mu\|}$	0	$\frac{g}{6(\beta-\mu)^2}$	$\frac{\beta}{\mu-\beta}$	$\frac{18-g}{g}$
IV	0	0	1	0	$\frac{1}{3}$	$-$
V	$\frac{1}{\sqrt{6}\beta}$	0	$\left(1-\frac{1}{2\beta^2}\right)^{1/2}$	$\frac{1}{6\beta^2}$	$\frac{1}{3}$	1
VI	$\sqrt{\frac{2}{3}}\beta$	0	0	$\frac{2}{3}\beta^2$	$\frac{2}{3}\beta^2$	1
VII	-1	0	0	1	1	1
VIII	$+1$	0	0	1	1	1

Table 3.1: List of the critical points for the autonomous system 3.20-3.22 within the quarter of unitary sphere with positive y and z. The values of the variables x, y, and z for each critical point are listed together with the corresponding value of the total dark energy density Ω_ϕ, the effective equation of state of the Universe $w_{\rm eff}$ introduced in Eq. 3.24, and the scalar field equation of state w_ϕ.

of unitary sphere with positive y and z and are listed in Table 3.1, where the following quantity has been introduced for convenience:

$$g(\mu,\beta) = 6\beta^2 - 6\beta\mu + 18\,, \tag{3.25}$$

and where for each critical point also the corresponding value of the effective equation of state is quoted. Having a look at Table 3.1 it is immediately possible to recognize some of the critical points already found for the uncoupled case and listed in Table 2.1.

For instance, the points VII and VIII correspond to the second and third point of Table 2.1, and are dominated by the kinetic energy of the scalar field ϕ.

The point I in Table 3.1 corresponds to the fourth point in Table 2.1, and is dominated by the scalar field with the kinetic term and the potential term sharing with a proportion given by the value of the potential slope μ the total energy density of the Universe.

The last point of Table 2.1, which is the *tracking* scaling solution that was thoroughly discussed in Chapter 2, corresponds in our new formulation to points II and III of Table 3.1. In the system 3.20-3.22 we have, in fact, specified the nature of the two barotropic fluids present in the Universe as being radiation ($\eta = 1/3$) and cold dark matter ($\eta = 0$). For the former case, it is immediately evident that point II corresponds to the case where the scalar field tracks the behavior of radiation, given by setting $\eta = 1/3$, and $\Gamma = 4/3$ in the last point of Table 2.1. For the latter case, we need to take into account that we have introduced a coupling between the cold dark matter and the scalar field ϕ, whose strength is given by the value of β. We can therefore recover the case where the scalar field tracks the behavior of cold dark matter that was discussed in Chapter 2 by setting $\eta = 0$, $\Gamma = 1$ in the last point of Table 2.1, and by considering the zero-coupling limit for point III of Table 3.1 by setting $\beta = 0$.

Finally, the first point of Table 2.1 corresponds to the points IV and VI in Table 3.1 for the case of radiation domination ($\eta = 1/3\,, \Gamma = 4/3$), and for the limiting case of uncoupled cold dark matter domination ($\eta = 0\,, \Gamma = 1\,, \beta = 0$), respectively.

Besides recovering the critical points already discussed for the uncoupled case when considering the proper limits of the system 3.20-3.22, we can identify the novel features introduced in the scaling solutions of Table 3.1 by the presence of the coupling between cold dark matter and the dark energy scalar field ϕ. The most evident of such new features is given by point V in Table 3.1. This is the only point for which there is no correspondence to any of the critical points of Table 2.1. In fact, this point is clearly not defined for $\beta = 0$, and exists only in presence of relatively large coupling. This point corresponds to a radiation dominated solution, where the radiation energy density $\Omega_r = z^2$ is at least 0.875, and where the dark energy scalar field ϕ and the cold dark matter fluid share the remaining energy density required for closure, having energy densities Ω_ϕ and Ω_c not larger than 0.042 and 0.083, respectively.

However, the most important new feature introduced by the coupling is given by point VI and by its modification with respect to the first point of Table 2.1 for the case of a non-vanishing coupling, $\beta \neq 0$. In fact, in presence of a coupling between cold dark matter and the dark energy scalar field ϕ, this point becomes a completely new type of

tracking scaling solution.
The novelty here is given by the fact that the scalar field tracks the evolution of the cold dark mater fluid even though the two components do not have the same equation of state. A careful analysis of the properties of point VI, in fact, reveals that in the case of a constant coupling β, the scalar field ϕ shares a constant fraction $\frac{2}{3}\beta^2$ of the total energy budget of the Universe, even if its *stiff* equation of state ($w_\phi = +1$) would imply a much faster dilution of the scalar field density ($\rho_\phi \propto a^{-6}$) as compared to the evolution of cold dark matter ($\rho_c \propto a^{-3}$). This is possible due to the presence of a direct interaction between the two fluids, that according to Eqs. 3.5,3.7,3.8 determines a net flux of energy from one fluid to the other. In particular, according to the specific form of the coupling considered here, the flux of energy will always go, for $\beta > 0$, from the cold dark matter fluid to the scalar field, as is clear by looking at the coupled Euler equation 3.7 and at the mass evolution of the cold dark matter field given by Eq. 3.10.

This implies that the cold dark matter fluid continuously feeds the scalar field energy density during the stage when the Universe follows the scaling solution given by Point VI, and consequently will also deviate from the usual uncoupled cold dark matter scaling law, a^{-3}. In particular, both fluids will scale with the same scaling law that can be written by taking into account the energy transfer between the two fluids given by Eq. 3.10, and which takes the form given by Eq. 3.14:

$$\rho_\phi \propto \rho_c \propto a^{-3} e^{-\kappa\beta\phi} \,. \tag{3.26}$$

As will be discussed in the next section, this modified evolution is one of the most relevant features of interacting dark energy models of this kind, and can have important cosmological consequences.

Now we can move to analyze the conditions of existence and stability of the critical points listed in Table 3.1. As already done for the uncoupled case, the conditions for stability of each critical point can be computed by means of an eigenvalue analysis of the system, and are listed, together with the existence conditions and the conditions for acceleration, in Table 3.2, where following Amendola (2000) the two quantities:

$$\mu_+ \equiv \frac{1}{2}\left(\beta + \sqrt{12+\beta^2}\right) \,, \quad \mu_0 \equiv \beta + \frac{3}{2\beta} \,, \tag{3.27}$$

Point	Existence	Stability	Accelerated for
I	$\mu < \sqrt{6}$	$\mu < \mu_+$, $\mu < 2$	$\mu < \sqrt{2}$
II	$\mu > \sqrt{2}$	$2 < \mu < 4\beta$	Never
III	$\mu < \mu_0$, $\lvert\mu - \beta\rvert > \sqrt{3/2}$	$\mu > \mu_+$, $\mu > 4\beta$	$\mu < -2\beta$
IV	$\forall\mu\,,\beta$	unstable $\forall\mu\,,\beta$	Never
V	$\lvert\beta\rvert > 1/\sqrt{2}$	$\mu > 4\beta$, $\beta > 1/\sqrt{2}$	Never
VI	$\lvert\beta\rvert < \sqrt{3/2}$	$\lvert\beta\rvert < 1/\sqrt{2}$, $\mu > \mu_0$	Never
VII	$\forall\mu\,,\beta$	unstable $\forall\mu\,,\beta$	Never
VIII	$\forall\mu\,,\beta$	unstable $\forall\mu\,,\beta$	Never

Table 3.2: Existence, stability, and acceleration conditions in the parameter space (β, μ) for all the critical points listed in Table 3.1. The table corresponds to the analysis done in Amendola (2000) for the definitions and the conventions adopted in this work, and where a few misprints present in Amendola (2000) have been corrected.

have been introduced for convenience.

It is very important to notice, from Table 3.2, that for any point in the parameter space (β, μ) more than one critical point can exist, but only one of them is stable, therefore for any choice of the parameters β and μ there will be only one *attractor* for the system.

As we already noticed, the only critical point whose existence region does not include the uncoupled case $\beta = 0$ is the Point V. All the other critical points can be evaluated for the case of zero coupling and can therefore be related to the critical points of the uncoupled case listed in Table 2.1. This holds also for the existence, stability, and acceleration conditions, which reduce for $\beta = 0$ to the ones found for the uncoupled case and listed in Table 2.1.

However, we are interested here in the case where a coupling $\beta \neq 0$ is present. In such case, we can see from Table 3.2 that there are only two scaling solutions which can be accelerated, corresponding to the points I and III in Table 3.1. This is anyway one more than in the uncoupled case, where the only accelerated solution was given by the scalar field dominated critical point given by the fourth point listed in Table 2.1. This point corresponds to Point I in the coupled case, and is the only late time accelerated attractor for sufficiently flat potentials.

The other accelerated solution is given by Point III, which corresponds, as already discussed, to the *tracking* scaling solution for the uncoupled case. However, in the uncoupled system described in Chapter 2 this solution could not be accelerated, while we can see from Table 3.2 that in presence of a coupling, and for sufficiently negative values of the coupling constant β, this solution is accelerated and stable.

The stability and acceleration regions in the parameter space (β, μ) as listed in Table 3.2 are shown in Fig. 3.1, which reproduces the Figure 1 presented in Amendola (2000) replotted with the conventions and definitions adopted in this work.

In the re-elaboration of the phase space analysis done in Amendola (2000) that we have presented in this paragraph we have also corrected a few misprints, in particular in the Table 3.2 for the stability of the critical points and in Eq. 3.27, that were present in the published version of Amendola (2000).

3.4 The weak coupling regime and the ϕMDE phase

If we start analyzing the properties of the accelerated scaling solution given by the Point I of Table 3.1, we immediately realize that on this solution the Universe is dominated by the energy density of the dark energy scalar field ϕ, and that $\Omega_{\phi} = 1$ along the solution I. This means that if we want to build a cosmological model which could possibly describe the observed Universe, we need to assume that this stable attractor has not yet been reached at the present stage of cosmic evolution, that the Universe is in a transient phase approaching it, but that the expansion is nevertheless already accelerated. This means that if we want to obtain the observed energy ratio between dark energy and cold dark matter, we need to tune the initial conditions for the dynamics of the scalar field.

This sort of tuning is, however, of a different type than the fine tuning that has to be invoked to address the Fine Tuning Problem. In this case, what has to be tuned is not the total amount of dark energy present in the early Universe, but the time of the transition between a decelerated matter dominated regime and an accelerated dark energy dominated attractor. Therefore this type of tuning is more related to the Coincidence Problem than to the Fine Tuning problem. As we have already stressed in Chapter 1, for the case of a cosmological constant Λ the two problems coincide, and they reduce to

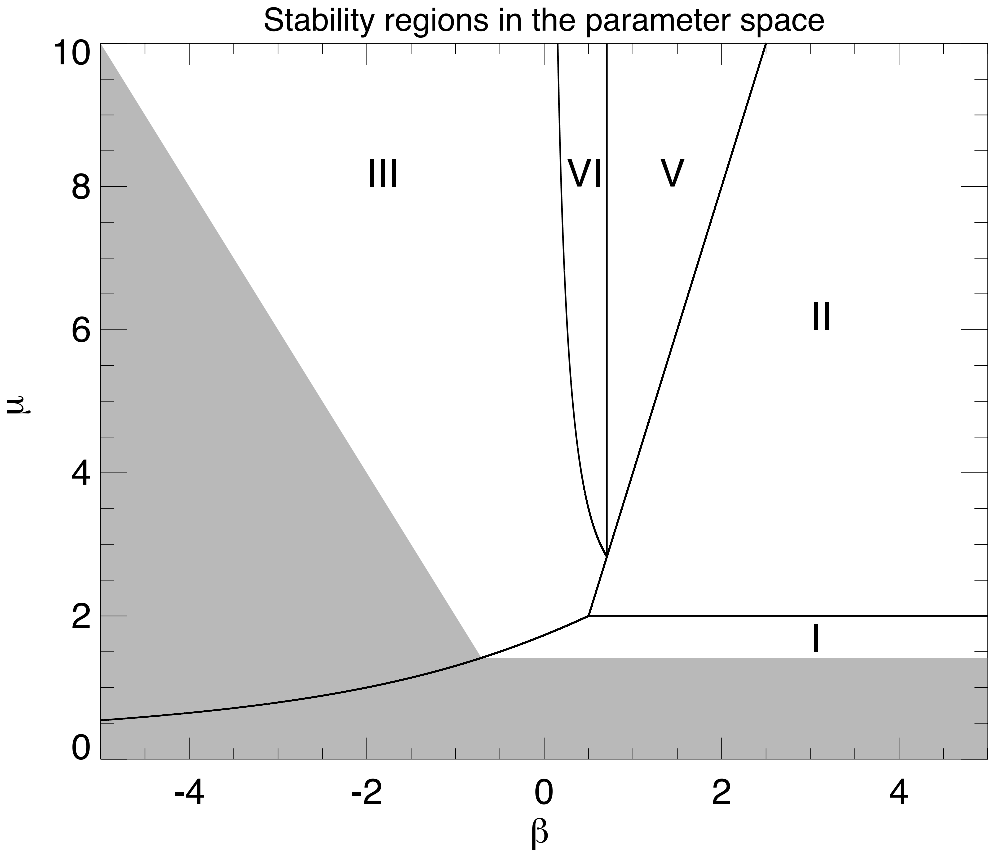

Figure 3.1: The parameter plane (β, μ) for the autonomous system of Eqs. 3.20-3.22 as presented in Figure 1 of Amendola (2000), replotted here with the definitions and the conventions adopted in this work. Each region is labelled with the number corresponding to the only critical point that is stable in that region. The shaded areas correspond to the regions of the parameter space where the stable solution is also accelerated.

the extreme fine tuning of a single number. However, for dynamic dark energy models in general, and therefore also for the case of dynamic coupled dark energy, the additional degree of freedom introduced by the dynamic nature of the scalar field splits the problem into the two different issues described above.

In any case, the stable attractor solution given by Point I could not be a viable description of our Universe without the initial conditions selection required to drive the system to the present-day coincidence of comparable Ω_c and Ω_ϕ.

The positive feature of the solution I is that it can be accelerated also for small values of the coupling β, and can therefore be treated in terms of deviations from the standard ΛCDM cosmological model.

In particular, we can consider the ΛCDM limit of the model, given by the absence of coupling ($\beta = 0$) and by setting the equation of state of the scalar field to the cosmological constant value of -1, which can be realized by ensuring that the kinetic energy of the scalar field ϕ always vanishes: $x^2 = \text{const.} = 0$. This can be done by setting the initial velocity of the scalar field to zero ($\dot{\phi}_{\rm i} = 0$) and by choosing a constant self-interaction potential ($V(\phi) = \text{const.} \ \rightarrow \mu \equiv 0$).

Therefore, the point of parameter space $(\beta, \mu) = (0, 0)$ corresponds to the usual ΛCDM cosmology, and as can be seen from Fig. 3.1, in this case the only accelerated stable solution is the Λ-dominated stage given by Point I which drives a De Sitter exponential expansion.

For a ΛCDM cosmological model, the Universe starts in a radiation dominated epoch at very early times, then it moves to a matter dominated epoch, and eventually reaches the final Λ-dominated stage. This means that a ΛCDM cosmic trajectory would start with $z \sim 1$ at early times (radiation domination), would then move to a stage where $z \sim 0$ and $x\,, y \sim 0$ (matter domination), and would finally reach the solution I where $\Omega_\Lambda = 1$. The trajectory of a ΛCDM cosmology is therefore given by the sequence IV→VI→I.

If we now move to dynamic and coupled dark energy models, we can explore the region of parameter space close to the ΛCDM case, but with non-vanishing values of β and μ. While in the ΛCDM case the saddle point corresponding to the matter dominated epoch is given by the point $(0, 0, 0)$ in the three-dimensional phase-space (x, y, z), for the coupled dark energy case this saddle will move to $(\sqrt{\frac{2}{3}}\beta, 0, 0)$, with a non-vanishing dark energy density given by $\Omega_\phi = \frac{2}{3}\beta^2$.

This is the new type of *tracking* scaling solution already introduced in the previous section, which is sustained by the continuous net flux of energy flowing from the cold dark matter fluid to the dark energy scalar field ϕ. This saddle point is not anymore completely dominated by cold dark matter, but presents a non-negligible fraction of dark energy, in a very similar fashion as what happens for the usual *tracking* solutions already discussed for the uncoupled dynamic dark energy case in Chapter 2 (and corresponding to the last point of Table 2.1 and to the limit $\beta = 0$ for the Point III of Table 3.1). However, although giving rise to a subdominant fraction of Early Dark Energy during matter domination in a very similar fashion, the two *tracking* solutions are inherently different. In fact, while the usual *tracking* solution seen in Chapter 2 is driven by a dynamic balance of the kinetic and the potential energy of the scalar field that sticks the equation of state to the one of the dominant fluid, therefore leading to a fraction of Early Dark Energy also during radiation domination, this new type of *tracking* solution is fully driven by the kinetic term of the scalar field, therefore leading to a *stiff* equation of state ($w_\phi = 1$), and allowing the presence of Early Dark Energy only after the end of radiation domination.

This peculiar new type of evolutionary phase of the Universe has been dubbed ϕMDE – which stands for ϕ-Matter-Dominated-Epoch – in Amendola (2000), and represents the main new feature of coupled dark energy models in the weak coupling regime close to the standard ΛCDM case $(\beta, \mu) = (0, 0)$.

Observational bounds on the coupling (which we will not discuss here in detail) for the case of one single dark matter family interacting with a constant coupling β with the dark energy scalar field ϕ (Wetterich (1995); Bean et al. (2008)) restrict the allowed region for β to the range $|\beta| < 0.1$. It is therefore clear from the conditions listed in Table 3.2 and from Fig. 3.1 that the other stable accelerated solution, which we will discuss in detail in the next section, is accelerated only for large values of the coupling ($|\beta| \geqslant 1/\sqrt{2}$), and cannot be a viable description of the present-day Universe.

This conclusion does not hold in the context of more complex cosmological models where more than one dark matter species is present. We will describe in detail in Chapter 4 one notable model of this kind (Amendola et al., 2008), but it is nevertheless important to stress here that in the context of the simplest coupled dark energy scenario with a single dark matter species, the only possible cosmological evolution is the one that ends up in a scalar field dominated attractor after going through a long radiation dominated epoch and a subsequent ϕMDE.

3.5 The strong coupling regime and the solution of the Coincidence Problem

The only other accelerated stable critical point besides the scalar field dominated one described in the previous section is given by point III. This is also a scaling solution on which the dark energy scalar field ϕ and the dark matter fluid share with a constant ratio the total cosmic energy, and which is accelerated for sufficiently negative values of the coupling β. For instance, if we set $\beta = -4.61$, $\mu = 2.19$, the existence and stability conditions for the point III are fulfilled, as well as the acceleration condition $\mu < -2\beta$, and for this choice of the parameters of the model we get:

$$\begin{aligned} \Omega_\phi &= 0.743\,, \\ \Omega_c &= 0.257\,, \\ w_\phi &= -0.91\,, \\ w_{\rm eff} &= -0.68\,, \end{aligned} \tag{3.28}$$

which are cosmological parameters compatible with observational data on the present-day Universe. When the solution given by point III is reached, these values will remain indefinitely constant throughout the subsequent expansion history of the Universe. This behavior therefore addresses the Coincidence Problem by removing the surprising coincidence of the present time being the only moment in cosmic history when the scalar field and the cold dark matter fluid have comparable energy densities, and as a consequence of the stability of the critical point III this qualitative solution of the Coincidence Problem is independent of the initial conditions of the system. However, in the context of cosmological models with a single dark matter species this solution turns out to be of very limited viability, since it runs in conflict with cosmological constraints coming from CMB and Large Scale Structure properties. In fact, with the parameters β and μ set as above, which ensures the stability and the acceleration of the scaling attractor III, the system follows a trajectory which starts from a radiation dominated phase (close to point IV), then goes through a transient given by the saddle point V, on which the cold dark matter density cannot exceed, as already remarked above, a value of $\Omega_c = 0.083$ (and for the parameter choice made here this value would actually be reduced to $\Omega_c = 0.016$), and finally reaches the scaling attractor given by point III. This trajectory does not exist, as already stressed, for the uncoupled case $\beta = 0$.

The striking features of this peculiar cosmic evolution, as found in Amendola (2000), are a much longer duration of radiation domination, which lasts until recently (roughly until $z \simeq 50$), and a complete lack of a matter dominated epoch. Such evolution heavily suppresses the growth of density fluctuations, first by the long radiation dominated epoch, and subsequently by the accelerated expansion, and so is starkly incompatible with the present observed value of $\sigma_8 = 0.769$ (Komatsu et al., 2008).

Although conceptually appealing due to its ability to provide a solution of the Coincidence Problem, the scaling attractor described by point III is therefore not a viable solution for the simplest models of coupled dark energy, and we will therefore focus our investigation of the non-linear effects of coupled dark energy scenarios, discussed in Chapters 5 and 6, only on the parameter space region leading to the final attractor given by point I.

However, the strong coupling regime leading to the scaling attractor III could represent an interesting and viable possibility for the solution of the Coincidence Problem in the context of cosmological models with multiple dark matter families, and in particular for the *Growing Neutrino Scenario* (Amendola et al., 2008) that will be extensively discussed in Chapter 4. A detailed investigation of this kind of model by means of the same numerical apparatus described in Chapters 5 and 6 will be surely performed in the near future.

3.6 A generalized model for interacting dark energy: background and perturbations evolution

We can now generalize the simple case of interacting dark energy discussed in the previous three sections to a more general situation where also other cosmic fluids – coupled or not to the dark energy scalar field – can be present in the Universe besides radiation and cold dark matter. In particular, this will allow us to include the baryonic component in the analysis of cosmic evolution, and in this context we will derive the perturbation equations for the evolution of the different fluids up to linear order that will be used in the next Chapters for the implementation of coupled dark energy models in the algorithm of the N-body code GADGET-2.

In general, coupled cosmologies can be described following the consideration (Kodama and Sasaki, 1984) that in any multicomponent system, though the total stress-energy tensor ${T^{\mu}}_{\nu}$ is conserved

$$\sum_{\alpha} \nabla_{\nu} T^{\nu}_{(\alpha)\mu} = 0\,, \tag{3.29}$$

the stress-energy tensor $T^{\mu}_{(\alpha)\nu}$ for each species α is, in general, not conserved and its divergence has a source term $Q_{(\alpha)\mu}$ representing the possibility that species are coupled:

$$\nabla_{\nu} T^{\nu}_{(\alpha)\mu} = Q_{(\alpha)\mu}\,, \tag{3.30}$$

with the constraint

$$\sum_{\alpha} Q_{(\alpha)\mu} = 0\,, \tag{3.31}$$

as already discussed in Section 3.2 (Eq. 3.4).

Furthermore, we will assume also in this analysis, as we already did in the previous Chapters, a flat Friedmann-Lemaître-Robertson-Walker (FLRW) cosmology, in which the line element can be written as $\mathrm{d}s^2 = a^2(\tau)(-\mathrm{d}\tau^2 + \delta_{ij}\mathrm{d}x^i\mathrm{d}x^j)$ where $a(\tau)$ is the scale factor, and τ is the *conformal time*, related to the *cosmic time* t by the relation:

$$d\tau = \frac{dt}{a}\,. \tag{3.32}$$

The Lagrangian of the system is of the form:

$$\mathcal{L} = -\frac{1}{2}g^{\mu\nu}\partial_\mu\phi\partial_\mu\phi - U(\phi) - m(\phi)\bar{\psi}\psi + \mathcal{L}_{\rm kin}[\psi] + \mathcal{L}_\alpha\,, \tag{3.33}$$

in which the mass of matter fields ψ coupled to the dark energy is a function of the scalar field ϕ as already introduced in Section 3.2 (Eq. 3.9). We assume here that other cosmic fluids not coupled to the dark energy scalar field (labelled by α) are also present in the Universe. In the following we will consider the case in which the dark energy is only coupled to cold dark matter. The choice $m(\phi)$ specifies the coupling and as a consequence the source term $Q_{(\phi)\mu}$ via the expression:

$$Q_{(\phi)\mu} = \frac{\partial \ln m(\phi)}{\partial\phi}\rho_c\,\partial_\mu\phi. \tag{3.34}$$

Due to the constraint 3.31, if no other species is involved in the coupling, $Q_{(c)\mu} = -Q_{(\phi)\mu}$.

The zero-component of Eq. 3.30 provides the conservation equations for the energy densities of each species:

$$\begin{aligned} \rho'_\phi &= -3\mathcal{H}\rho_\phi(1+w_\phi) - Q_{(\phi)0} \quad , \\ \rho'_c &= -3\mathcal{H}\rho_c + Q_{(\phi)0}\,, \end{aligned} \tag{3.35}$$

where $\mathcal{H}$ is the *conformal Hubble function* defined by:

$$\mathcal{H} \equiv \frac{1}{a}\frac{da}{d\tau}\,. \tag{3.36}$$

Here we have treated each component as a fluid with $T^\nu_{(\alpha)\mu} = (\rho_\alpha + p_\alpha)u_\mu u^\nu + p_\alpha\delta^\nu_\mu$, where $u_\mu = (-a, 0, 0, 0)$ is the fluid 4-velocity and $w_\alpha \equiv p_\alpha/\rho_\alpha$ is the equation of state. The class of models considered here corresponds to the choice:

$$m(\phi) = m_0 e^{-\beta(\phi)\frac{\phi}{M}}\,, \tag{3.37}$$

with the coupling term equal to

$$Q_{(\phi)0} = -\frac{\beta(\phi)}{M}\rho_c\phi' . \tag{3.38}$$

This set of cosmologies has been widely investigated, for $\beta(\phi)$ given by a constant, both in its background and linear perturbation features (Wetterich, 1995; Amendola, 2000) as well as with regard to the effects on structure formation (Amendola, 2004; Pettorino and Baccigalupi, 2008), and via a first N-body simulation (Macciò et al., 2004).

We now perturb the quantities involved in our cosmological framework up to first order in the perturbations (Kodama and Sasaki, 1984; Ma and Bertschinger, 1995). The perturbed metric tensor can then be written as

$$\tilde{g}_{\mu\nu}(\tau, \mathbf{x}) = \mathbf{g}_{\mu\nu}(\tau) + \delta\mathbf{g}_{\mu\nu}(\tau, \mathbf{x}) , \tag{3.39}$$

where $\delta g_{\mu\nu} \ll 1$ is the linear metric perturbation, whose expression in Fourier space is given by:

$$\begin{aligned} \delta g_{00} &= -2a^2 AY , \\ \delta g_{0i} &= -a^2 BY_i , \\ \delta g_{ij} &= 2a^2[H_L Y \delta_{ij} + H_T Y_{ij}] , \end{aligned} \tag{3.40}$$

where A, B, H_L, H_T are functions of time and of the wave vector $\mathbf{k}$, and Y_i, Y_{ij} are the vector and tensor harmonic functions obtained by differentiating Y, defined as the solution of the Laplace equation $\delta^{ij}\nabla_i\nabla_j Y = -|k|^2 Y$. Analogously, the perturbed stress-energy tensor for each fluid (α) can be written as $\tilde{T}^{\mu}_{(\alpha)\nu} = T^{\mu}_{(\alpha)\nu} + \delta T^{\mu}_{(\alpha)\nu}$ where the perturbations read as:

$$\begin{aligned} \delta T^0_{(\alpha)0} &= -\rho_{(\alpha)}\delta_{(\alpha)} Y , \qquad (3.41) \\ \delta T^0_{(\alpha)i} &= h_{(\alpha)}(v_{(\alpha)} - B) Y_i , \\ \delta T^i_{(\alpha)0} &= -h_{(\alpha)} v_{(\alpha)} Y^i , \\ \delta T^i_{(\alpha)j} &= p_{(\alpha)} \left[\pi_{L(\alpha)} Y \delta^i_j + \pi_{T(\alpha)} Y^i_j\right] . \end{aligned}$$

The perturbed conservation equations then become:

$$(\rho_\alpha\delta_\alpha)' + 3\mathcal{H}\rho_\alpha\delta_\alpha + h_\alpha(kv_\alpha + 3H_L') + 3\mathcal{H}p_\alpha\pi_{L\alpha} = -\delta Q_{(\alpha)0} \tag{3.42}$$

for the energy density perturbation $\delta_\alpha = \delta\rho_\alpha/\rho_\alpha$, and:

$$[h_\alpha(v_\alpha - B)]' + 4\mathcal{H}h_\alpha(v_\alpha - B) - kp_\alpha\pi_{L\alpha} - h_\alpha kA + \frac{2}{3}kp\pi_{T\alpha} = \delta Q_{(\alpha)i} \tag{3.43}$$

for the velocity perturbation v_α.

The scalar field ϕ can also be perturbed, yielding in Fourier space

$$\tilde{\phi} = \phi + \delta\phi = \phi + \chi(\tau) Y\,. \tag{3.44}$$

Furthermore, we can express the perturbations of the source as:

$$\begin{aligned} \delta Q_{(\phi)0} &= -\frac{\beta(\phi)}{M}\rho_c \delta\phi' - \frac{\beta(\phi)}{M}\phi'\delta\rho_c - \frac{\beta_{,\phi}}{M}\phi'\rho_c\delta\phi\,, && (3.45)\\ \delta Q_{(\phi)i} &= k\frac{\beta(\phi)}{M}\rho_c\delta\phi\,. && (3.46)\end{aligned}$$

In the Newtonian gauge ($B = 0, H_T = 0, H_L = \mathbf{\Phi}, A = \mathbf{\Psi}$) the set of equations for the density and velocity perturbations for dark energy and cold dark matter read:

$$\begin{aligned} &\delta\rho'_\phi + 3\mathcal{H}(\delta\rho_\phi + \delta p_\phi) + k h_\phi v_\phi + 3h_\phi \mathbf{\Phi}' = \frac{\beta(\phi)}{M}\rho_c\delta\phi' + \frac{\beta(\phi)}{M}\phi'\delta\rho_c + \frac{\beta_{,\phi}}{M}\phi'\delta\phi\rho_c\,,\\ &\delta\rho'_c + 3\mathcal{H}\delta\rho_c + k\rho_c v_c + 3\rho_c\mathbf{\Phi}' = -\frac{\beta(\phi)}{M}\rho_c\delta\phi' - \frac{\beta(\phi)}{M}\phi'\delta\rho_c - \frac{\beta_{,\phi}}{M}\phi'\delta\phi\rho_c\,,\\ &h_\phi v'_\phi + \left(h'_\phi + 4\mathcal{H}h_\phi\right)v_\phi - k\delta p_\phi - k h_\phi\mathbf{\Psi} = k\frac{\beta(\phi)}{M}\rho_c\delta\phi\,,\\ &v'_c + \left(\mathcal{H} - \frac{\beta(\phi)}{M}\phi'\right)v_c - k\mathbf{\Psi} = -k\frac{\beta(\phi)}{M}\delta\phi\,. \end{aligned} \tag{3.47}$$

The perturbed Klein Gordon equation in Newtonian gauge reads:

$$\begin{aligned} \delta\phi'' &+ 2\mathcal{H}\delta\phi' + \left(k^2 + a^2 U_{,\phi\phi}\right)\delta\phi - \phi'\left(\mathbf{\Psi}' - 3\mathbf{\Phi}'\right) + 2a^2 U_{,\phi}\mathbf{\Psi} = \\ & 3\mathcal{H}^2\Omega_c\left[\beta(\phi)\delta_c + 2\beta(\phi)\mathbf{\Psi} + \beta_{,\phi}(\phi)\delta\phi\right]\,. \end{aligned} \tag{3.48}$$

For the N-body implementation we are interested in, the Newtonian limit holds, for which $\lambda \equiv \mathcal{H}/k \ll 1$. In this case we have

$$\delta\phi \sim 3\lambda^2\Omega_c\beta(\phi)\delta_c\,. \tag{3.49}$$

In this limit, the gravitational potential is approximately given by

$$\mathbf{\Phi} \sim \frac{3}{2}\frac{\lambda^2}{M^2}\sum_{\alpha\neq\phi}\Omega_\alpha\delta_\alpha\,. \tag{3.50}$$

We can then define an effective gravitational potential

$$\mathbf{\Phi_c} \equiv \mathbf{\Phi} + \frac{\beta(\phi)}{M}\delta\phi, \tag{3.51}$$

which also reads, in real space and after substituting the expressions for $\mathbf{\Phi}$ (Eq. 3.50) and for $\delta\phi$ (Eq. 3.49):

$$\nabla^2 \mathbf{\Phi_c} = -\frac{a^2}{2}\rho_c\delta_c\left(1+2\beta^2(\phi)\right) - \frac{a^2}{2}\sum_{\alpha\neq\phi,c}\rho_\alpha\delta_\alpha\,, \tag{3.52}$$

where the last term takes into account the case in which other components not coupled to the dark energy are present in the total energy budget of the Universe. We can see here another important feature introduced by the coupling: cold dark matter then feels an effective enhanced gravitational constant

$$\tilde{G}_c = G_N[1+2\beta^2(\phi)], \tag{3.53}$$

where G_N is the usual Newtonian value. Therefore, the strength of the gravitational interaction is not a constant anymore if β is a function of the scalar field ϕ. The last equation in 3.47, written in real space and in terms of the effective gravitational potential, gives a modified Euler equation of the form:

$$\vec{\nabla}\vec{v}_c' + \left(\mathcal{H} - \frac{\beta(\phi)}{M}\phi'\right)\vec{\nabla}\vec{v}_c + \frac{3}{2}\mathcal{H}^2\left[\Omega_c\delta_c + 2\Omega_c\delta_c\beta^2(\phi) + \sum_{\alpha\neq\phi,c}\Omega_\alpha\delta_\alpha\right] = 0\,. \tag{3.54}$$

As in Amendola (2004), if we assume that the cold dark matter is concentrated in one particle of mass m_c at a distance r from a particle of mass M_c at the origin, we can rewrite the cold dark matter density contribution as

$$\Omega_c\delta_c = \frac{8\pi G M_c e^{-\int\beta(\phi)\mathrm{d}\phi}\delta(0)}{3\mathcal{H}^2 a}\,, \tag{3.55}$$

where we have used the fact that a non-relativistic particle at position $\vec{r}$ has a density given by $m_c n\delta(\vec{r})$ (where $\delta(\vec{r})$ stands for the Dirac distribution) with mass given by $m_c \propto e^{-\int\beta(\phi)\mathrm{d}\phi}$, formally obtained from Eq. 3.36. We have further assumed that the density of the M_c mass particle is much larger than ρ_c. The Euler equation in cosmic time ($\mathrm{d}t = a\,\mathrm{d}\tau$) can then be rewritten in the form of an acceleration equation for the particle at position $\vec{r}$:

$$\dot{\vec{v}}_c = -\tilde{H}\vec{v}_c - \vec{\nabla}\frac{\tilde{G}_c\tilde{M}_c}{r}\,, \tag{3.56}$$

where we explicitly see that the usual equation is modified in three ways.

First, the friction term now contains an additional contribution given by the second term of the expression defining $\tilde{H}$:

$$\tilde{H} \equiv H\left(1 - \frac{\beta(\phi)}{M}\frac{\dot{\phi}}{H}\right)\,. \tag{3.57}$$

Second, the cold dark matter particles feel an effective gravitational constant $\tilde{G}$ given by 3.53.

Third, the cold dark matter particles have an effective mass, varying with time, given by:

$$\tilde{M}_c \equiv M_c e^{-\int \beta(\phi)\frac{\mathrm{d}\phi}{\mathrm{d}a}\mathrm{d}a} \quad . \tag{3.58}$$

In the N-body analysis carried out in the present work, we consider β to be a constant, so that the effective mass formally reads $\tilde{M}_c \equiv M_c e^{-\beta(\phi-\phi_0)}$. We have numerically solved the full background and linear perturbation equations with a suitably modified version of CMBEASY (Doran, 2005), that we briefly describe here.

In collaboration with G. Robbers and V. Pettorino we have implemented the full background and linear perturbation equations derived above in the Boltzmann code CMBEASY (Doran, 2005) for the general case of a dark energy component coupled to dark matter via a coupling term given by Eq. 3.30. The form of this coupling, as well as the evolution of the dark energy (either modelled as a scalar field or purely as a dark energy fluid), can be freely specified in our implementation.

Compared to the standard case of uncoupled dark energy, the modifications include a modified behavior of the background evolution of cold dark matter and dark energy given by Eqs. 3.35 and 3.36, as well as the implementation of the linear perturbations described by Eq. 3.47, and their corresponding adiabatic initial conditions. The presence of a coupling between cold dark matter and dark energy further complicates the choice of suitable initial conditions even for the background quantities, since dark matter no longer scales as a^{-3}, and so cannot simply be rescaled from its desired value today. For each of the models considered in the rest of this work we choose to set the initial value of the scalar field close to its tracker value in the uncoupled case, and then adjust the value of the potential constant Λ (see Eq. 5.1 in Chapter 5) and the initial cold dark matter energy density such that we obtain the desired present-day values.

Part II

The Growing Neutrino Scenario

Chapter 4

Quintessence models with a Growing Matter component

4.1 Multiple dark matter families

As we have discussed in detail in the previous Chapter, the only two accelerated solutions for the system 3.20-3.22 are given by Point I and Point III of Table 3.1. Of these two solutions, as we have already stressed, only the scalar field dominated attractor given by Point I can represent a viable solution for the late time cosmology in a system with one single cold dark matter species. In fact, from Table 3.2 we can see that the solution III is accelerated only for quite large values of the coupling ($|\beta| > 2\mu$) which would be in conflict with observational bounds on the coupling to cold dark matter derived from CMB analysis, $|\beta| < 0.1$ (Bean et al., 2008), for most of the reasonable values of the potential slope μ.

Moreover, we have already mentioned in Chapter 3 that from the analysis of the dynamics of coupled dark energy models in the parameter space region that determines the acceleration of the solution III (Amendola, 2000), the cosmic evolution that leads to this final scaling attractor lacks a cold dark matter dominated epoch, which results in a strong suppression of structure growth.

The appealing feature of addressing – at least qualitatively – the Coincidence Problem, characterizing the solution III, can therefore be exploited only in presence of some other mechanism able to drive the growth of cosmic structures up to the presently measured value of σ_8.

This mechanism could be provided by the existence of two disjoint scaling solutions, the first one dominated by the cold dark matter fluid and the later one dominated by the dark energy scalar field in a similar fashion as for Point III.

However, as already anticipated, in Amendola et al. (2006) it has been shown that even a fully generalized scalar field lagrangian density $p(\phi, \chi)$ cannot produce this "double scaling" dynamics. A way out of this problem cannot therefore reside in changing the form of the lagrangian density of the dark energy scalar field.

On the other hand, as suggested in the first place by Huey and Wandelt (2006), one could imagine generalizing the system 3.20-3.22 to a situation in which two different families of dark matter are present in the Universe. In this way, one of the two dark matter species – uncoupled or weakly coupled to the dark energy scalar field – could drive the long matter dominated scaling solution that brings the scalar field energy density to its present observed value, therefore addressing the Fine Tuning Problem and allowing the growth of cosmic structures up to the observed value of σ_8, while the other one – more strongly coupled to the dark energy – could drive the system to a final scaling attractor of the type described by Point III of Table 3.1, therefore easing the Coincidence Problem.

The development of this idea is the main subject of the present Chapter.

4.2 The Growing Matter Model

We can realize the model described in the final part of the previous section by assuming that, besides the usual cold dark matter fluid, another species of dark matter is present in the Universe and contributes to the total energy density. We will assume here for simplicity that the cold dark matter fluid is not coupled to the dark energy scalar field, which means $\beta_c = 0$, although a small value of the cold dark matter coupling, compatible with the trajectories that lead to the final attractor given by Point I of Table 3.1 and with the present observational bounds (Bean et al., 2008), would not modify the main conclusions of our analysis.

On the other hand, we will assume that the new additional dark matter component, which we call "Growing Matter", is coupled to the dark energy scalar field ϕ via a constant coupling function β_g compatible with the acceleration condition for the final scaling attractor given by Point III of Table 3.1. According to such conditions, one has that for an exponential potential as defined in Eq. 2.6 with a positive value of the potential slope μ, the coupling β_g needs to be negative and large.

As a consequence of this condition, one has from Eq. 3.10 that the mass of Growing Matter particles will increase with time:

$$m_g(\phi) = m_g(0)e^{-\kappa\beta_g\phi}\,. \tag{4.1}$$

This means that, opposite to the case for a positive coupling between dark energy and the cold dark matter fluid, the energy density of the Growing Matter component will decrease with the expansion of the Universe slower than a^{-3}, due to a direct injection of energy coming from the dark energy scalar field on top of the usual volume dilution.

The dynamic equation for the dark energy scalar field ϕ will then be modified by the presence of the coupling to the Growing Matter component according to Eq. 3.35:

$$\ddot{\phi} + 3H\dot{\phi} = -\frac{\partial V}{\partial\phi} + \kappa\beta_g\rho_g\,. \tag{4.2}$$

Evidently, Eq. 4.2 contains an additional "force" acting on the scalar field ϕ besides the usual one deriving from the self-interaction potential $V(\phi)$. This "force" is proportional to ρ_g and will counteract any increase of ϕ once $\beta_g\rho_g$ has become comparable to $\partial V/\partial\phi$. This new term in the evolution equation for the scalar field is capable, for the case of a negative and large value of the coupling β_g, to dramatically slow down the evolution of ϕ.

For the case of an almost static behavior of $\phi(t)$ (i.e. for $x \ll y$) the equation of state w_ϕ will then approach the Cosmological Constant value of $w_\phi = -1$, and the scalar field potential $V(\phi)$ will then act similarly to a Cosmological Constant.

This phenomenology is responsible for the acceleration of the Universe on the scaling attractor solution III, that in the present case will feature a constant ratio of the dark energy scalar field ϕ and of the Growing Matter component in place of the uncoupled cold dark matter fluid, which, on this scaling solution, will dilute away.

In this model, during the early phases of the evolution of the Universe the new additional terms in the dynamic equations deriving from the Growing Matter component play no role yet, since the Growing Matter energy density ρ_g is negligible, and therefore the cosmological evolution follows the usual *tracking* solution for the uncoupled dynamic dark energy scenario discussed in Chapter 2, i.e. the solution represented by the last point in Table 2.1. On this attractor one has:

$$\phi(t) = \phi_0 + \frac{2}{\kappa\mu}\ln(\frac{t}{t_0}) \,, \tag{4.3}$$

$$V(\phi) \sim \dot{\phi}^2 \sim \rho_c \sim t^{-2} \,, \tag{4.4}$$

$$m_g \sim \Omega_g \sim t^{2\gamma} \,, \quad \rho_g \sim t^{2(\gamma-1)} \,, \tag{4.5}$$

where we have defined a new important dimensionless parameter for our model:

$$\gamma \equiv -\frac{\beta}{\mu} \,. \tag{4.6}$$

It is evident from Eq. 4.5 that for $\gamma > 0$ (or $\beta < 0$) the relative weight of Growing Matter Ω_g increases with time, and that the Growing Matter energy density ρ_g, as anticipated, scales slower than a^{-3}, or even increases:

$$\rho_g \propto a^{-3(\gamma-1)} \,. \tag{4.7}$$

The *tracking* scaling regime ends once $\gamma\Omega_g$ has reached a value of order one. When this happens, in fact, the additional terms proportional to the Growing Matter energy density in the evolution equations start to become important, and the *tracking* evolution of the scalar field is stopped by the new additional "force" in the Klein Gordon equation 4.2.

After the exit from the *tracking* scaling regime, the Universe evolves towards the final scaling attractor given by the solution III of Table 3.1. On this attractor, the expansion of the Universe can be accelerated according to the conditions listed in Table 3.2 for the point III, which means:

$$\mu < -2\beta \rightarrow \gamma > \frac{1}{2} \,. \tag{4.8}$$

Since the stress-energy tensor for the sum of dark energy and Growing Matter is conserved, the equation of state in the non-relativistic regime defined as:

$$w \equiv \frac{p_\phi}{\rho_\phi + \rho_g} \tag{4.9}$$

represents the equation of state measured by e.g. Supernovae experiments given that the two fluids behave at the background level as a single conserved component.

In the accelerated regime, the late time scaling attractor given by Point III evolves as:

$$\begin{aligned} H(t) &= \frac{2(\gamma+1)}{3}t^{-1}\,, && (4.10)\\ w &= -1+\frac{1}{\gamma+1}\,, && (4.11)\\ \Omega_\phi &= 1-\Omega_g = 1-\frac{1}{\gamma+1}+\frac{3}{\mu^2(\gamma+1)^2}\,. && (4.12) \end{aligned}$$

For large γ, the total matter content of the Universe, given by $\Omega_M = \Omega_c + \Omega_b + \Omega_g$, is given, on the late time attractor, by $\Omega_M \approx \Omega_g \approx 1/\gamma$, and is therefore quite small. The presently observed value $\Omega_M \approx 0.25$ then indicates that we are now in the middle of the transition from matter domination – characterized by $\Omega_M \approx 1 - 3/\mu^2$ – to the final attractor dominated by the scalar field.

The limiting case $\gamma \gg 1$ admits a particularly simple description. In this case, in fact, there is a sudden transition between the two scaling solutions at the time t_c when the two terms on the right-hand-side of Eq. 4.2 have equal size, which means $\mu V = -\beta_g\rho_g$, or $\Omega_g = \Omega_\phi/\gamma$. The dark energy scalar field ϕ evolves before this time following the *tracking* attractor, and then it stops at a value $\phi_c \equiv \phi(t)$ at t_c. Thus, for $t \geqslant t_c$ and large γ the cosmological evolution is almost the same as for a Cosmological Constant with value $V(\phi_c)$. On the other hand, before t_c, the standard cold dark matter cosmology is only mildly modified by the presence of an early dark energy component, that for large enough μ ensures compatibility with observations of CMB anisotropies and structure formation.

The redshift of the transition can be estimated by equating the potential V at the end of the *tracking* scaling solution to its present value:

$$\frac{H(z_c)}{H_0^2} = \frac{2}{3}\Omega_\phi(0)\mu^2 \qquad (4.13)$$

and can be approximated as:

$$1 + z_c \approx \left[\frac{2\Omega_\phi(0)\mu^2}{3-3\Omega_\phi(0)}\right]^{1/3}\,. \qquad (4.14)$$

Assuming $\mu = 10$, and either $\gamma = 5.2$ or $\gamma = 39$, as we have done for the numerical examples shown below, one obtains $z_c \approx 6$ or $z_c \approx 5$, respectively. Therefore z_c is large enough not to affect the present supernovae observations.

4.3 The Growing Neutrino Scenario

So far we have made no assumption about the constituent of the Growing Matter component. Here we propose to associate Growing Matter with cosmic neutrinos, which offers the interesting perspective that no new particles – besides the dark energy scalar field and cold dark matter – need to be introduced.

Furthermore, the present value of the Growing Matter energy density ρ_g can be computed from the relic neutrino abundance and the present average neutrino mass $m_\nu(t_0)$ through the relation (assuming $h = 0.72$):

$$\Omega_g(0) = \frac{m_\nu(t_0)}{16\mathrm{eV}}\,. \tag{4.15}$$

For large $|\beta|$ the neutrino mass becomes rapidly very small in the past, such that neutrinos cannot affect early structure formation. Therefore the standard cosmological bounds on the neutrino mass (Komatsu et al., 2008) do not apply.

We show in Fig. 4.1 the time evolution of the different cosmic components and the effective equation of state for the combined fluid of the dark energy scalar field ϕ and Growing Matter.

For a given neutrino mass $m_\nu(t_0)$, this model has only two parameters, μ and γ, which will determine the present matter density $\Omega_M(t_0)$ as in Eq. 4.12. Replacing γ by $\Omega_M(t_0)$ the model has then only one more parameter, μ, as compared to the ΛCDM model. For an analytical estimate of the relation between $\Omega_M(t_0) = 1 - \Omega_\phi(t_0)$ and $m_\nu(t_0)$ we use the observation (see Fig. 4.1) that the ratio Ω_g/Ω_ϕ (averaged) has already reached today its asymptotic value given by Eq. 4.12, and we get:

$$\Omega_\phi(t_0) = \left[\frac{\gamma+1}{1-\frac{3}{\mu^2(\gamma+1)}} - 1\right]\frac{m_\nu(t_0)}{30.8h^2\mathrm{eV}} \approx \frac{\gamma m_\nu(t_0)}{16\mathrm{eV}}\,. \tag{4.16}$$

This relation determines the present dark energy density by the neutrino mass and γ as:

$$[\rho_\phi(t_0)]^{1/4} = 1.27\left(\frac{\gamma m_\nu(t_0)}{\mathrm{eV}}\right)^{1/4} 10^{-3}\mathrm{eV}\,. \tag{4.17}$$

Since the equation of state is today already near the asymptotic value of Eq. 4.11 (see again Fig. 4.1), it is possible to relate it to the neutrino mass by Eqs. 4.11 and 4.17, yielding:

$$w = -1 + \frac{m_\nu(t_0)}{12\mathrm{eV}}\,. \tag{4.18}$$

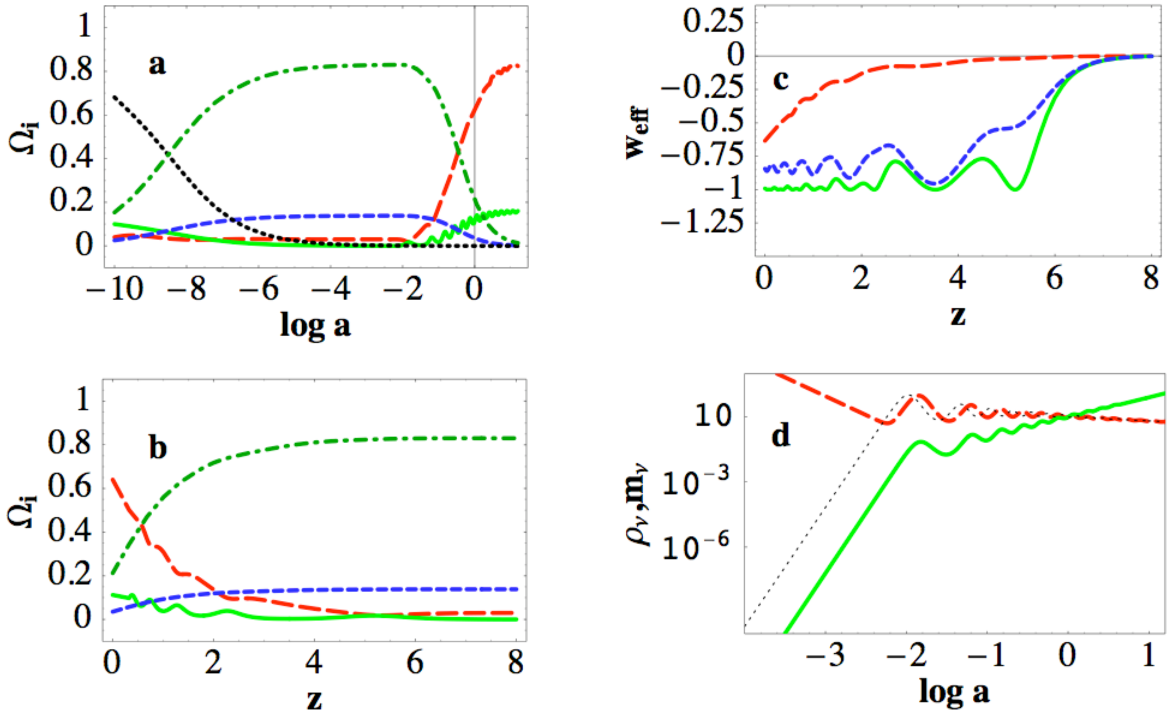

Figure 4.1: Cosmological evolution for neutrino Growing Matter for $\mu = 10$, $\gamma = 5.2$ and $m_\nu(t_0) = 2.3$ eV. *Panel a*: density fractions for radiation Ω_r (black, dotted line), cold dark matter Ω_c (dark-green, dot-dashed line), baryons Ω_b (blue, short-dashed line), dark energy Ω_ϕ (red, long-dashed line), and Growing Matter (neutrinos) Ω_g (light-green, solid line). *Panel b*: blow up of *Panel a* near the present time. *Panel c*: total equation of state $w_{\text{eff}} \equiv p_{\text{tot}}/\rho_{\text{tot}}$ (red, long dashed line); combined equation of state of dark energy and neutrinos (blue, short-dashed line); and equation of state of the dark energy alone (green, solid line). *Panel d*: neutrino energy density ρ_g (red, long-dashed line) and neutrino mass m_ν (green, solid line) normalized to unity today. The dotted curve represents the energy density of always non-relativistic heavy Growing Matter.

This expression is a very remarkable result of the model, since it directly relates the present dark energy equation of state to the present value of the neutrino mass, yielding $m_\nu(t_0) < 2.4$ eV for $w < -0.8$.

4.4 Enhanced growth of neutrino density fluctuations

As we have shown in section 3.6, a dark matter species coupled to the dark energy scalar field through an interaction term of the form considered here, is subject to an extra attractive force that would result in an effectively enhanced strength of the gravitational attraction. We have also shown in Eq. 3.53, that the enhancement does not depend on the sign of the coupling, since the enhancement factor is given by $(1 + 2\beta^2)$.

Therefore, in the case of Growing Matter, the dark energy scalar field will mediate, for scales smaller than the scalar range l_ϕ:

$$l_\phi = \frac{1}{\kappa\mu\sqrt{V}}\,, \tag{4.19}$$

a new scalar interaction that will enhance the gravitational attraction by a factor $(1+2\beta_g^2)$.

The condition for the onset of an enhanced growth of density fluctuations in the Growing Matter component, i.e. for the growth of $\delta\rho_g$, requires that the average scalar force $\sim 2\beta_g^2\Omega_g$ is comparable to the average gravitational force $\sim \Omega_M$. This happens at a redshift z_{eg}, somewhat larger than the crossover redshift z_c defined above. Therefore, at the time of the start of the enhanced growth, the *tracking* scaling solution is still valid with $\Omega_M \approx 1 - 3/\mu^2$ and:

$$\begin{aligned} \Omega_g(z) &= [(1+z_c)/(1+z)]^{3\gamma}\,\Omega_g(z_c)\,, & (4.20)\\ \Omega_g(z_c) &\approx \gamma y^2(z_c) \approx 3\gamma/(2\mu^2)\,, & (4.21) \end{aligned}$$

which results in an expression for z_{eg}:

$$\frac{1+z_{eg}}{1+z_c} = \left[3\gamma^2(\gamma+1)\right]^{1/3\gamma}\,. \tag{4.22}$$

As we said, the enhanced growth of Growing Matter density fluctuations concerns only structures with size smaller than the range l_ϕ of the scalar force mediated by the dark energy scalar field ϕ. For the *tracking* scaling solution, one has (Wetterich, 1995):

$$l_\phi(t) = \frac{\sqrt{2}}{3H(t)}\,, \tag{4.23}$$

while l_ϕ remains essentially constant in the late time cosmology, i.e. for $t > t_c$. For scales larger than l_ϕ the enhanced growth is suppressed, and therefore a "window of adiabatic fluctuations" opens up in the range $l_\phi < l < H^{-1}$.

It is also important to stress another aspect concerning the growth of Growing Matter density fluctuations in the case where the Growing Matter component is associated with neutrinos. Neutrino Growing Matter was relativistic at early times, so that free streaming prevents clustering. For the case of $\beta_g < 0$ that we are discussing here, neutrinos have actually remained relativistic much longer than neutrinos with constant mass.

In the limit of large γ one can estimate that the neutrinos are relativistic at $a < a_R$, where a_R is given by:

$$a_R \approx [m_\nu(t_0)/T_{\nu,0}]^{-1/4} = 0.11\left(\frac{m_\nu(t_0)}{1\mathrm{eV}}\right)^{-1/4}\,, \tag{4.24}$$

which corresponds to $z_R \in (2 - 10)$ for $m_\nu(t_0) \in (0.015 - 2.3)$. The growth of neutrino structures starts only for $z < z_R$, and even then, neutrinos cannot cluster on scales smaller than their "free streaming length" l_{fs}, which is given by the horizon scale at the time 4.24 when neutrinos become non-relativistic, close to:

$$H^{-1}(a_R) \approx 200\,(m_\nu(t_0)/1\mathrm{eV})^{-3/8}\,h^{-1}\mathrm{Mpc} \approx (150 - 1500)\mathrm{Mpc}\,. \qquad (4.25)$$

For scales within the window $l_{fs} < l < l_\phi$ the neutrino clustering is strongly enhanced (for $z < z_{eg}$) due to the additional attractive force mediated by the dark energy scalar field. This enhanced clustering starts first for scales close to l_{fs}.

One may thus investigate the possible formation of lumps with a characteristic scale around l_{fs}. This has been done recently by Mota et al. (2008) and Pettorino et al. (2009) finding evidence, from a numerical computation of the linear density evolution, of the appearance of structures with scales compatible with 4.25.

4.5 Observational features

As we have stressed above, for the large γ limit the cosmological evolution for $t > t_c$ is almost the same as for a Cosmological Constant with value $V(\phi_c)$. However, for not too large values of μ and γ the model differs from ΛCDM, and we will discuss here the different deviations that could possibly be directly observable.

First of all, the presence of an early dark energy component, as a consequence of the *tracking* scaling regime driven by uncoupled cold dark matter, will manifest itself by the detailed peak location of the CMB anisotropies (Doran et al., 2001a), by the change in the linear growth of cosmic structures (Ferreira and Joyce, 1997; Doran et al., 2001b), and by the abundance and properties of non-linear structures (Bartelmann et al., 2005; Grossi and Springel, 2008; Francis et al., 2008).

Second, for not too large γ there would be a sizeable fraction of Growing Matter today, namely $\Omega_g \approx \Omega_\phi/\gamma$. For the case of neutrino Growing Matter this would require rather large neutrino masses. As a consequence of this non-negligible Growing Matter fraction, the present matter density $\rho_M = \rho_c + \rho_b + \rho_g$ differs from the rescaled matter density in the early Universe $\rho_c + \rho_b$. This difference may affect the matching of the present values of

Ω_M and Ω_b/Ω_M obtained from supernovae, baryon acoustic oscillations and clusters, with determinations from the CMB at high redshift through the value of t_{eq} and the baryon content of the Universe at last scattering. This effect is anyway small for large values of γ (i.e. for low neutrino masses).

Third, as we already discussed in the previous section, Growing Matter can affect the formation of structures in the late stages through the onset of the enhanced growth of Growing Matter density fluctuations. For very massive particles, Growing Matter would consist of relatively few particles which have presumably fallen into the cold dark matter structures formed in early cosmology. For scales smaller than the range l_ϕ of the scalar interaction these particles feel a mutual attraction enhanced by a factor $(1 + 2\beta_g^2)$ as compared to gravity. Thus, once a sufficient Ω_g is reached, the Growing Matter structures $\delta\rho_g$ will grow rapidly. They will then influence, in turn, the structures in baryons and cold dark matter once the gravitational potential of the Growing Matter structures becomes comparable to the one of the cold dark matter structures. This, however, happens rather late, especially for large γ, since Growing Matter constitutes only a small fraction of the present matter density in this case.

Finally, it is interesting to realize that the dark energy relative density Ω_ϕ during the *tracking* matter dominated scaling solution depends only on μ (see Table 2.1), while during the final accelerated phase it depends on μ and γ (see Eq. 4.12). The linear fluctuation growth during the two phases will also depend on the two parameters in a different way. Then, an estimation of the growth rate during the two epochs will constrain separately the two parameters of the model. Along with the comparison between the neutrino mass and the dark energy equation of state given by Eq. 4.18, this offers a direct way to test the Growing Neutrino Scenario.

Part III

Numerical Implementation and Cosmological Simulations

Chapter 5

Numerical implementation of coupled dark energy models

The main aim of this work is to investigate the effects that a coupling between dark energy and other cosmological components, as introduced in the last paragraph of Chapter 3, can have on cosmic structure formation, with a particular focus on the non-linear regime which is not readily accessible by the linear analytic approach described above. To this end we study a set of cosmological N-body simulations performed with the code GADGET-2 (Springel, 2005), which we suitably modified for this purpose.

The required modifications of the standard algorithms of an N-body code for simulating coupled dark energy cosmologies are extensively described in this Chapter. Interestingly, they require us to reconsider and in part drop several assumptions and approximations that are usually adopted in N-body simulations. We note that previous attempts to use cosmological N-body simulations for different flavors of modified Newtonian gravity have been discussed, for example, in Macciò et al. (2004); Nusser et al. (2005); Stabenau and Jain (2006); Springel and Farrar (2007); Laszlo and Bean (2008); Sutter and Ricker (2008); Oyaizu (2008); Kesden and Kamionkowski (2006), but to our knowledge Macciò et al. (2004) is the only previous work focusing on the properties of non-linear structures in models of coupled quintessence.

We will therefore frequently refer to the analysis pursued by Macciò et al. (2004). With our modified version of GADGET-2 we first ran a set of low-resolution cosmological simulations ($L_{\rm box} = 320h^{-1}$Mpc, $N_{\rm part} = 2 \times 128^3$) for the same coupled dark energy models investigated in Macciò et al. (2004), but with cosmological parameters updated to the latest results from WMAP (Komatsu et al., 2008) for a ΛCDM cosmological model.

Parameter	Value
Ω_{CDM}	0.213
H_0	71.9 km s^{-1} Mpc^{-1}
Ω_{DE}	0.743
σ_8	0.769
Ω_b	0.044
n	0.963

Table 5.1: Cosmological parameters for our set of N-body simulations, consistent with the WMAP 5 year results for a ΛCDM cosmology (Komatsu et al., 2008).

In the coupled models we consider, the role of dark energy is played by a quintessence scalar field with a Ratra-Peebles (Ratra and Peebles, 1988) self-interaction potential of the form:

$$U(\phi) = \frac{\Lambda^{4+\alpha}}{\phi^{\alpha}} \,, \tag{5.1}$$

where Λ and α fix the dark energy scale in agreement with observations, and with a constant coupling to cold dark matter particles only, as described in Chapter 3; we label them as RP1-RP6 in analogy with Macciò et al. (2004). It is important to notice here that we adopt with Eq. 3.38 a different definition of the coupling β than the one adopted in Macciò et al. (2004). This is the reason why the values of β for our RP1-RP6 models listed in Table 5.2 are different from the ones listed in Macciò et al. (2004), although the models are identical.

For four of these models (ΛCDM, RP1, RP2, RP5) we then ran high-resolution simulations in a smaller cosmological box ($L_{\mathrm{box}} = 80h^{-1}$ Mpc, $N_{\mathrm{part}} = 2 \times 512^3$), and we investigated the properties of collapsed objects for this set of simulations. In addition to these four high-resolution simulations we ran another three simulations with the same resolution (ΛCDM-NO-SPH, RP5-NO-SPH, RP5-NO-GF), whose features will be described below. The cosmological parameters for our models are listed in Table 5.1, and the physical parameters of each model together with the details of the corresponding N-body simulations are listed in Table 5.2.

The presence of a direct coupling between the dark energy scalar field ϕ and other cosmic fluids – in the fashion described by Eqs. 3.30,3.35, 3.36 – introduces new features in the cosmic background evolution as well as additional physical processes that must be taken into account in N-body models. In the following, we describe these features and their implementation in GADGET-2 one by one, recalling and further emphasizing the

Model	α	β_b	β_c	Box Size (h^{-1} Mpc)	Number of particles	M_b ($h^{-1}M_\odot$)	$M_{\rm CDM}$ ($h^{-1}M_\odot$)	ϵ_s (h^{-1} kpc)
ΛCDM (low)	0	0	0	320	2×128^3	1.9×10^{11}	9.2×10^{11}	50.0
ΛCDM (high)	0	0	0	80	2×512^3	4.7×10^7	2.3×10^8	3.5
ΛCDM (high - no SPH)	0	0	0	80	2×512^3	4.7×10^7	2.3×10^8	3.5
RP1 (low)	0.143	0	0.04	320	2×128^3	1.9×10^{11}	9.2×10^{11}	50.0
RP1 (high)	0.143	0	0.04	80	2×512^3	4.7×10^7	2.3×10^8	3.5
RP2 (low)	0.143	0	0.08	320	2×128^3	1.9×10^{11}	9.2×10^{11}	50.0
RP2 (high)	0.143	0	0.08	80	2×512^3	4.7×10^7	2.3×10^8	3.5
RP3 (low)	0.143	0	0.12	320	2×128^3	1.9×10^{11}	9.2×10^{11}	50.0
RP4 (low)	0.143	0	0.16	320	2×128^3	1.9×10^{11}	9.2×10^{11}	50.0
RP5 (low)	0.143	0	0.2	320	2×128^3	1.9×10^{11}	9.2×10^{11}	50.0
RP5 (high)	0.143	0	0.2	80	2×512^3	4.7×10^7	2.3×10^8	3.5
RP5 (high - no SPH)	0.143	0	0.2	80	2×512^3	4.7×10^7	2.3×10^8	3.5
RP5 (high - no GF)	0.143	0	0.2	80	2×512^3	4.7×10^7	2.3×10^8	3.5
RP6 (low)	2.0	0	0.12	320	2×128^3	1.9×10^{11}	9.2×10^{11}	50.0

Table 5.2: List of the different simulations performed with our modified version of GADGET-2. The simulations have different force and mass resolution, and are accordingly labelled as *low* or *high* resolution. Notice that the values of the coupling listed here are different from the ones adopted in Macciò et al. (2004) due to the different definition of the coupling function 3.37. However, the models in effect have *identical* coupling strength to those investigated in Macciò et al. (2004).

Function	Meaning
$H(a)$	Hubble function
$\Delta G(a)$	Possible global variation of the gravitational constant
$\beta_b(\phi)$	Coupling function for the baryons
$\beta_c(\phi)$	Coupling function for cold dark matter
Δm_b	Correction term for baryon particle masses
Δm_c	Correction term for cold dark matter particle masses
$\Omega_{kin}(\phi)$	Dimensionless kinetic energy density of the scalar field

Table 5.3: List of input functions for the coupled dark energy implementation in GADGET-2.

results described in Macciò et al. (2004) and in Pettorino and Baccigalupi (2008).

5.1 Modified expansion rate

As pointed out in Chapter 3, the coupling modifies the background evolution through the existence of a phase – corresponding to the so called ϕMDE era in Amendola (2000) – in which the coupled matter fluid (cold dark matter in our case) and the dark energy scalar field evolve with a constant energy density ratio (here we always assume the Universe to be flat such that $\Omega_{\text{tot}} = 1$). This leads to the presence of a non-negligible early dark energy component (Doran et al., 2001c; Doran and Robbers, 2006) during the entire epoch of structure formation. The effect of such an early dark energy is to change the expansion history of the Universe, which has to be properly taken into account for the N-body time integration. In order to do so, we replaced the computation of the Hubble function $H(a)$ in GADGET-2 by a linear interpolation from a table of values of $H(a)$ precomputed for each model under investigation with the modified version of CMBEASY described in Chapter 3. The effect of the coupling on the expansion is shown in Fig. 5.1. We note that the same approach has also been adopted for the other relevant quantities described in Table 5.3, which were first computed numerically using CMBEASY, and then used as an input for our modified version of GADGET-2.

5.2 Mass variation

As described in Sec. 3.6, the coupled species feature an effective particle mass that changes in time. Consequently, the corresponding cosmological densities ρ_c or ρ_b no longer scale as a^{-3}, but will have a correction term arising from the variation of particle masses on top of the pure volume dilution. This correction depends on the scalar field dynamics,

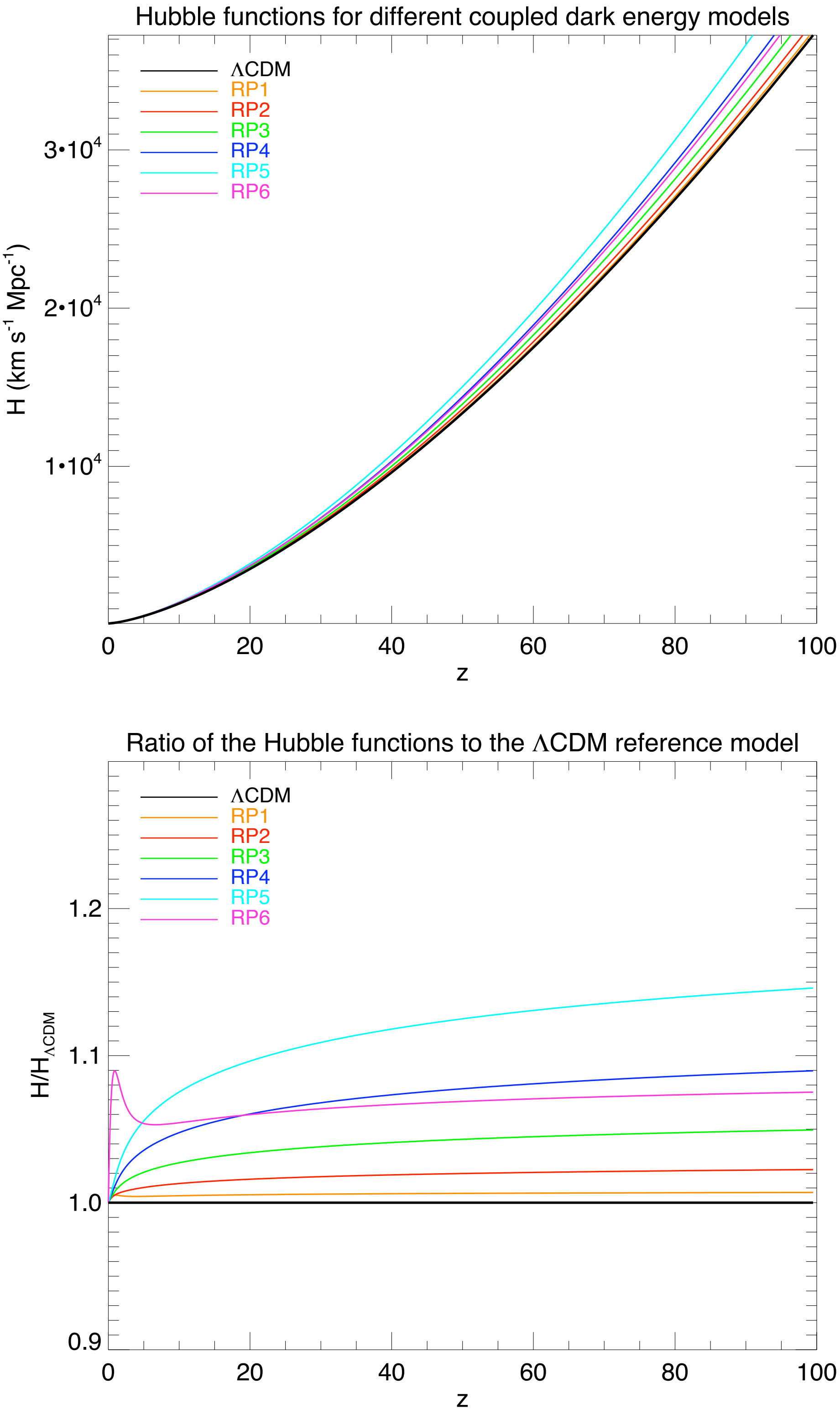

Figure 5.1: *Top panel*: Hubble functions as a function of redshift for the different coupled dark energy models with constant coupling investigated in this work and listed in Table 5.2 as compared to ΛCDM (black curve). *Bottom panel*: Ratio of the Hubble functions of each coupled dark energy model to the Hubble function for the reference ΛCDM cosmology as a function of redshift.

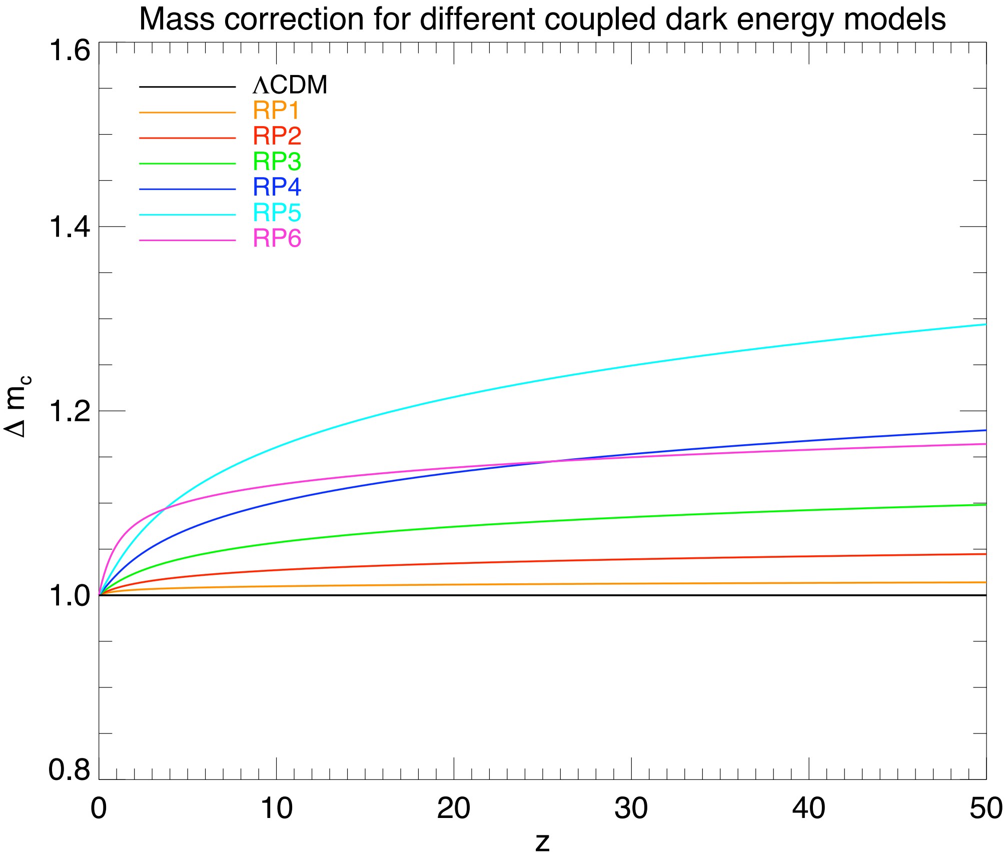

Figure 5.2: Mass correction as a function of redshift for the coupled dark energy models with constant coupling investigated in this work and listed in Table 5.2 as compared to ΛCDM (black curve).

and takes the form of Eq. 3.58. Then, if the particle masses in the simulation box are computed according to the cosmic densities $\Omega_{c,0}$ and $\Omega_{b,0}$ at the present time, they will need to be corrected at each timestep by a factor

$$\Delta m_c(a) = e^{-\int_a^1 \beta_c(\phi)\frac{\mathrm{d}\phi}{\mathrm{d}a}\mathrm{d}a}, \tag{5.2}$$

$$\Delta m_b(a) = e^{-\int_a^1 \beta_b(\phi)\frac{\mathrm{d}\phi}{\mathrm{d}a}\mathrm{d}a}. \tag{5.3}$$

In Fig. 5.2, we show the evolution with redshift of the correction term 5.2 for our set of models.

Although the coupled dark energy implementation for GADGET-2 that we present here allows in principle for a coupling also to baryons, such a coupling is tightly constrained by experimental tests of gravity on solar system scales (Damour et al., 1990). Therefore, in the coupled dark energy models we consider in this work, no coupling to baryons is considered, and baryon masses are always constant. However, even a very tiny coupling to baryons, in the range allowed by present bounds, could possibly play a significant role in cosmological models with multiple dark matter families (Huey and Wandelt, 2006), like for example the *Growing Neutrino* scenario introduced by Amendola et al. (2008) and extensively described in Chapter 4.

5.3 Cosmological extra friction

A further modification to the GADGET-2 code concerns the extra cosmological friction term induced by the coupling in the Euler equation, as shown in Eqs. 3.56,3.57. In standard cosmological simulations with GADGET-2 the usual cosmological friction term (first term of Eq. 3.57) is not directly computed because the choice of variables removes it from the acceleration equation. If we denote with $\vec{x}$ comoving coordinates and with $\vec{r} = a(t)\vec{x}$ physical coordinates, we have that:

$$\dot{\vec{r}} = H\vec{r} + \vec{v}_p \,, \qquad \vec{v}_p \equiv a(t)\dot{\vec{x}} \,. \tag{5.4}$$

Instead of using the peculiar velocity $\vec{v}_p$, GADGET-2 makes use of the variable $\vec{p} \equiv a^2(t)\dot{\vec{x}}$ (see Springel (2005) for more details), for which the following relation holds:

$$\dot{\vec{v}}_p = \frac{1}{a}\dot{\vec{p}} - \frac{H}{a}\vec{p}. \tag{5.5}$$

It is then straightforward, by using Eq. 5.5, to find a generalization of Eq. 3.56 to a system of N particles, in terms of the new velocity variable $\vec{p}$:

$$\dot{\vec{p}}_i = \frac{1}{a}\left[\beta_\gamma(\phi)\frac{\dot{\phi}}{M}a\vec{p}_i + \sum_{j\neq i}\frac{\tilde{G}_{ij}m_j\vec{x}_{ij}}{|\vec{x}_{ij}|^3}\right] \,, \tag{5.6}$$

where i and j are indices that span over all the particles of the simulation, $\gamma = c, b$ for cold dark matter or baryons respectively, and $\tilde{G}_{ij}$ is the effective gravitational constant between the i-th and the j-th particles, as determined in Eq. 3.53 and whose implementation will be discussed below.

It is evident from Eq. 5.6 that for zero coupling no cosmological friction term is present in the acceleration equation, which is then just Newton's law in comoving coordinates. In general, however, whenever a coupling is present, the additional term given by the expression:

$$a(\dot{\vec{p}} + \Delta\dot{\vec{p}}) \equiv a\dot{\vec{p}} + \beta_\gamma(\phi)\frac{\dot{\phi}}{M}a\vec{p}_i \tag{5.7}$$

has to be explicitly added to the Newtonian acceleration of every particle. This term does not depend on the matter distribution in the rest of the Universe. It is therefore a purely cosmological drag that would be present also in the absence of any gravitational attraction. It is interesting to notice that in the case of constant positive coupling and a monotonic scalar field potential, as investigated here, the extra cosmological friction term induces an acceleration in the same direction as the velocity of the particle. It therefore is effectively an "anti-friction" term, speeding up the motion of the particles.

Scalar field models where the dynamics of the field or the evolution of the coupling induce a change in the sign of $\beta_i(\phi)\dot{\phi}$, thereby changing the direction of this extra friction force, could present particular features different from the ones identified and described in the rest of this work. Such models will be studied in the near future (Baldi and Macciò, prep) with the numerical implementation that we discuss here.

5.4 Fifth force implementation

One of the most important modifications introduced by the coupling between dark energy and cold dark matter is the presence of a modified gravitational constant, formally written as in Eq. 3.53, for the gravitational interaction of cold dark matter particles. In fact, if in general the substitution (Amendola, 2004)

$$G_N \rightarrow \tilde{G}_{lm} = G_N \cdot (1 + 2\beta_l\beta_m) \,, \tag{5.8}$$

holds for each pair (l, m) of particles, with l and m denoting the species of the particle, in our case only the $(l, m) = (c, c)$ interaction is affected, while (b, c) or (b, b) interactions remain unchanged since $\beta_b = 0$. The dependence of this modified gravitational interaction on the particle type requires an N-body code to distinguish among different particle types in the gravitational force calculation. In GADGET-2, the gravitational interaction is computed by means of a TreePM hybrid method (see Springel, 2005, for details about the TreePM algorithm), so that both the tree and the particle-mesh algorithms have to be modified in order to account for this new phenomenology.

Tree algorithm modifications – In a standard tree algorithm, each node of the tree carries information about the position of its centre of mass, its velocity, and its total mass. The decision whether to compute the force exerted on a target particle by the whole node or to further divide it into eight smaller nodes is made based on a specific opening criterion, which sets the accuracy threshold for approximating the gravitational potential of a distribution of particles with its low-order multipole expansion. Since in uncoupled cosmological models all particles interact with the same gravitational strength, as soon as the opening criterion is fulfilled the force is computed assigning all the mass contained in the node to its centre of mass. For coupled quintessence cosmologies, this is no longer accurate enough given that the different particle species will contribute differently to the gravitational force acting on a target particle. This means that besides the total mass and the total centre of mass position and velocity, each node has to carry information about the mass and centre-of-mass position and velocity of each particle species with different coupling.

Particle-Mesh algorithm modifications – In the Tree-PM algorithm, the long-range part of the gravitational force is computed by means of Fourier techniques. For coupled dark energy models, where different particle species interact with an effectively different gravitational force, the PM procedure has to be repeated as many times as there are differently interacting particle types, each time assigning to the cartesian grid only the mass in particles of a single type, and then computing the gravitational potential and the acceleration deriving from the spatial distribution of that particle species alone. In this way, the total force is built up as a sum of several partial force fields from each particle type.

5.5 Initial conditions

The initial conditions of a cosmological N-body simulation need to specify the positions and velocities of all the particles in the cosmological box at the starting redshift z_i of the simulation. These quantities are usually computed by setting up a random-phase realization of the power spectrum of the studied cosmological model according to the Zel'dovich approximation (Zel'dovich, 1970). The normalization amplitude of the power spectrum is adjusted such that the linearly evolved rms-fluctuation σ_8 on a top-hat scale of $8\,h^{-1}$Mpc at a given redshift $z_{\rm norm}$ (usually chosen to be $z_{\rm norm} = 0$) has a prescribed amplitude.

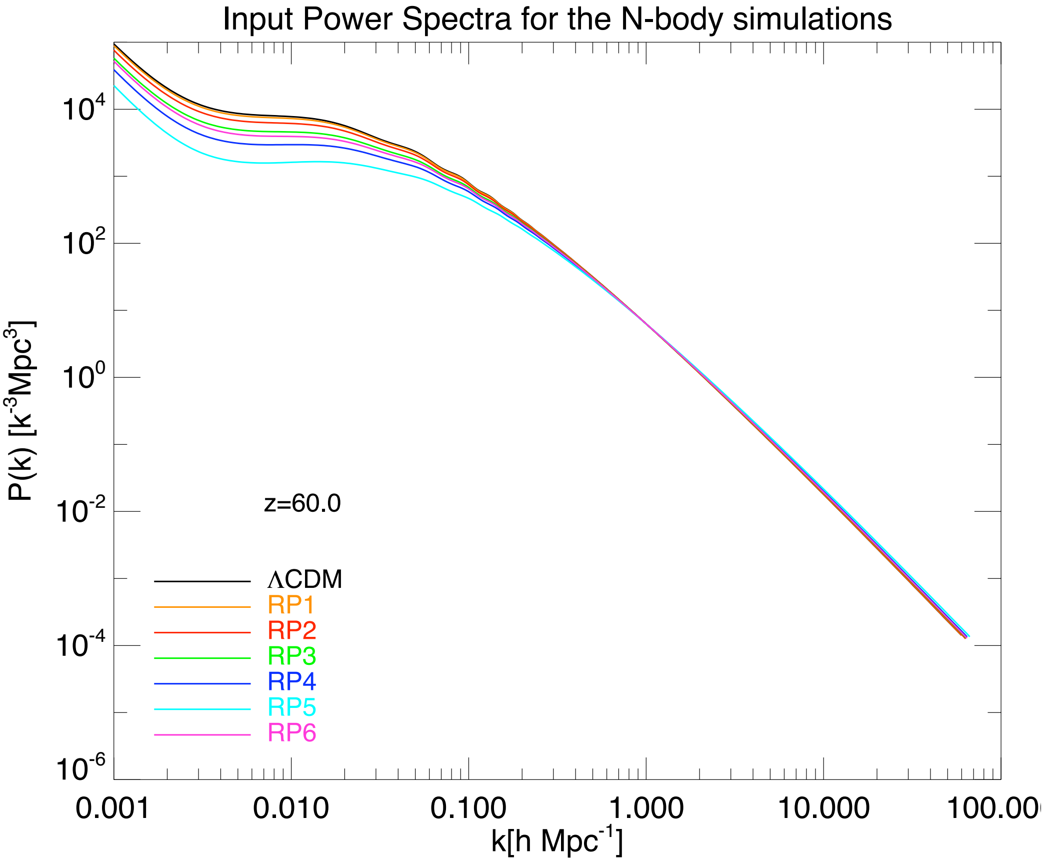

Figure 5.3: Gauge-invariant matter power spectra at $z = 60$ for the interacting dark energy models with constant coupling investigated in the present work as computed with the modified version of CMBEASY described in Chapter 3. The increase of power for $k \leqslant 0.004h$ Mpc^{-1} is due to the choice of the gauge-invariant variables for computing the evolution of perturbations implemented in CMBEASY.

The coupling between dark energy and cold dark matter can have a strong impact on the transfer function of matter density fluctuations, as first pointed out by Mainini and Bonometto (2007). For this reason we compute the required initial power spectrum directly with the modified Boltzmann code CMBEASY, because the phenomenological parameterizations of the matter power spectrum available for the ΛCDM cosmology (e.g. Bardeen et al., 1986; Eisenstein and Hu, 1998) would not be accurate enough. The resulting effect on the power spectrum is shown in Fig. 5.3 for the different models considered in our set of simulations.

Once the desired density field has been realized with this procedure, the displacements of the particles from the grid points need to be rescaled with the linear growth factor D_+ for the cosmological model under investigation between the redshifts $z_{\rm norm}$ and z_i

in order to set the correct amplitude of the power spectrum at the starting redshift of the simulation. Also, the velocities of the particles are related to the local overdensities according to linear perturbation theory, via the following relation, here written in Fourier space:

$$\vec{v}(\vec{k}, a) = i f(a) a H \delta(\vec{k}, a) \frac{\vec{k}}{k^2} , \tag{5.9}$$

where the growth rate $f(a)$ is defined as

$$f(a) \equiv \frac{d \ln D_+}{d \ln a} . \tag{5.10}$$

This requires an accurate calculation of the linear growth function $D_+(z)$ for the coupled model, which we again compute numerically with CMBEASY.

We note that a phenomenological parameterization of the growth function for coupled dark energy models with constant coupling to cold dark matter has recently been made available by Di Porto and Amendola (2008). However, it is only valid for models with no admixture of uncoupled matter, whereas in our case we also have a baryonic component. Also, in the ΛCDM cosmology, the total growth rate is well approximated by a power of the total matter density Ω_M^γ, with $\gamma = 0.55$, roughly independently of the cosmological constant density (Peebles, 1980). This, however, is no longer true in coupled cosmologies, as we show in Figs. 5.4,5.5,5.6. We find that, for our set of coupled dark energy models, a different phenomenological fit given by

$$f(a) \sim \Omega_M^\gamma (1 + \gamma \frac{\Omega_{\rm CDM}}{\Omega_M} \epsilon_c \beta_c^2) , \tag{5.11}$$

with $\gamma = 0.56$ (as previously found in Amendola and Quercellini, 2004) and $\epsilon_c = 2.4$ works well. The fit 5.11 reproduces the growth rate with a maximum error of $\sim 2\%$ over a range of coupling values between 0 and 0.2 and for a cosmic baryon fraction Ω_b/Ω_m at $z = 0$ in the interval $0.0 - 0.1$ for the case of the potential slope $\alpha = 0.143$ (corresponding to the slope of the RP1-RP5 models). For a value of $\alpha = 2.0$ (corresponding to the slope assumed for RP6) the maximum error increases to $\sim 4\%$ in the same range of coupling and baryon fraction. In Figs. 5.4,5.5,5.6, we plot the fitting formulae together with the exact $f(a)$. For our initial conditions setup we in any case prefer to use the exact function $f(a)$ directly computed for each model with CMBEASY, rather than any of the phenomenological approximations.

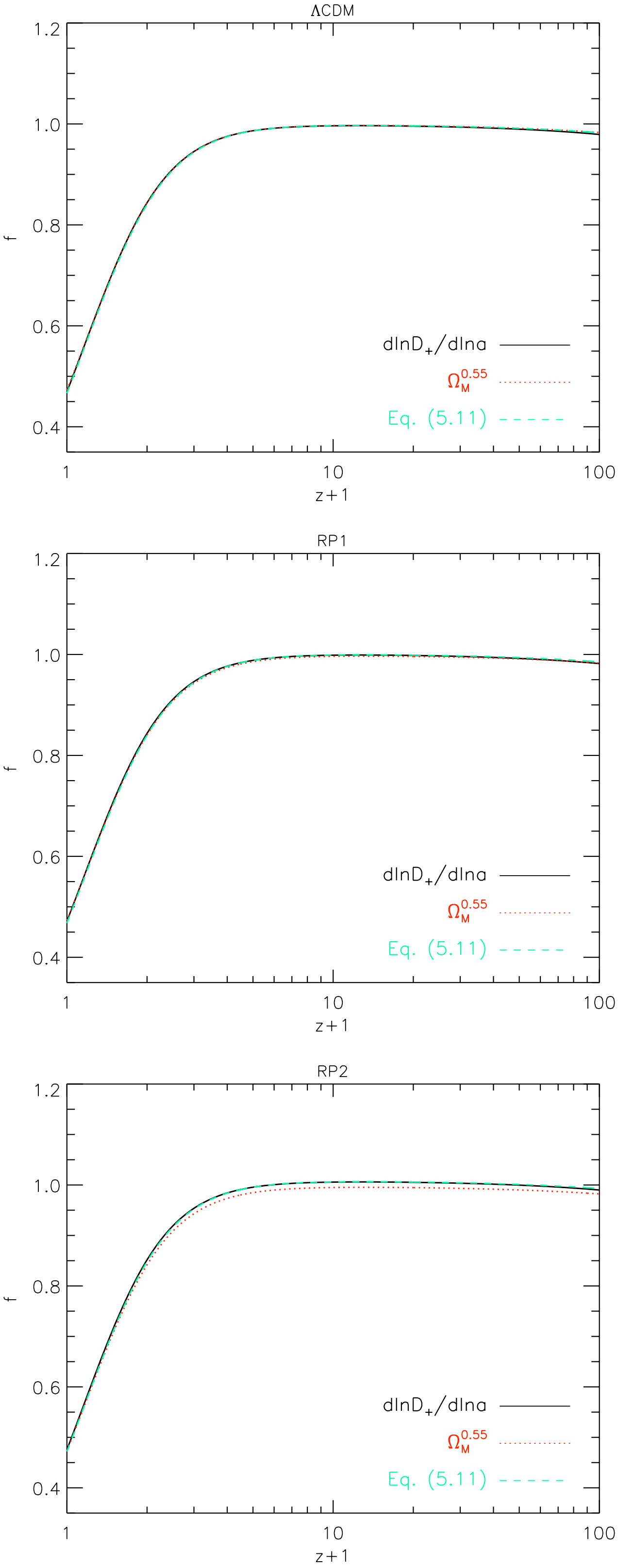

Figure 5.4: Comparison of the function $f(a)$ with its usual approximation $f = \Omega_M^{0.55}$ and with the new fit of Eq. 5.11 for the models ΛCDM, RP1, RP2.

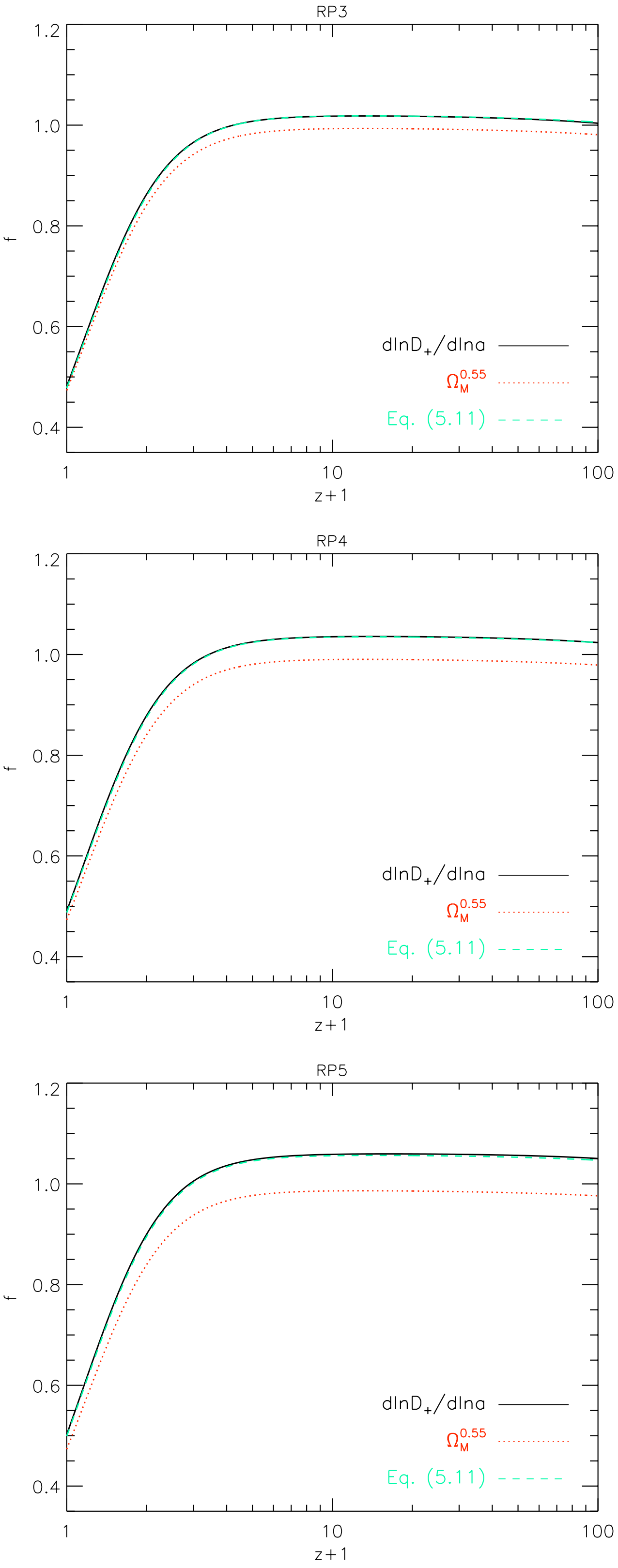

Figure 5.5: Comparison of the function $f(a)$ with its usual approximation $f = \Omega_M^{0.55}$ and with the new fit of Eq. 5.11 for the models RP3, RP4, RP5.

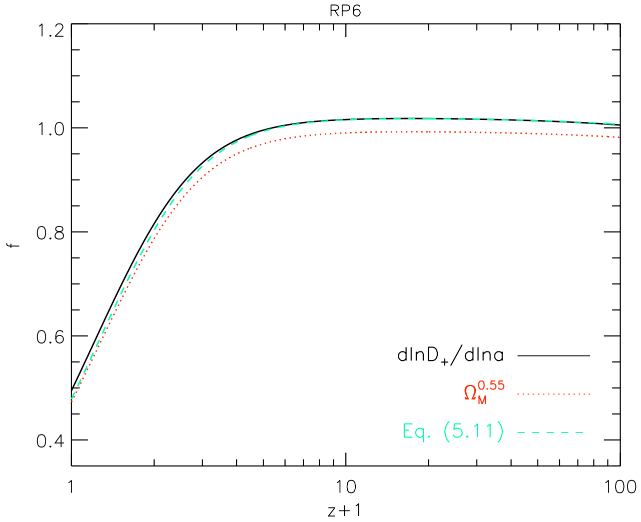

Figure 5.6: Comparison of the function $f(a)$ with its usual approximation $f = \Omega_M^{0.55}$ and with the new fit of Eq. 5.11 for the model RP6.

5.6 Summary of the coupled dark energy interaction scheme

The whole implementation of coupled dark energy models in the N-body code GADGET-2 that we developed and that has been discussed extensively in the present Chapter can be represented and summarized by the scheme shown in Fig. 5.7. In our simulation box we will have two different kinds of matter particles: baryons (represented in Fig. 5.7 by the light blue circles), and cold dark matter (represented by the black circles).

The simulation box, i.e. the space in which the particles are located, will expand with a rate given by the specific Hubble function of each cosmological model, which will depend, besides the usual cosmological parameters, on the strength of the coupling constant β.

The mass of the baryon particles will keep the constant value computed according to the cosmological baryon density at $z = 0$, which means:

$$m_b = \frac{\Omega_b(0) 3 H_0^2 L_{\rm box}^3}{8\pi G_N N_{\rm part}} \,. \tag{5.12}$$

The mass of cold dark matter particles, instead, will be corrected at each timestep with the correction factor Δm_c given by Eq. 5.2, which means that cold dark matter particles will have a mass:

$$m_c(a) = \frac{\Omega_c(0) 3 H_0^2 L_{\rm box}^3}{8\pi G_N N_{\rm part}} \times \Delta m_c(a) \,. \tag{5.13}$$

The gravitational interaction between two baryon particles will be the usual newtonian interaction, i.e. the strength of the gravitational force will be given by G_N, as well as for the case of an interaction between a baryonic particle and a cold dark matter particle. On the other hand, the gravitational interaction between two dark matter particles will be ruled by the effective gravitational constant $\tilde{G}_{cc} = G_N(1 + 2\beta_c^2)$, according to Eq. 5.8.

Finally, the cold dark matter particles will receive an additional acceleration in the direction of their velocity at each timestep, where this additional acceleration is proportional to the particle velocity $\vec{v}$ and to the factor f defined as:

$$f \equiv \beta\frac{\dot{\phi}}{M} \tag{5.14}$$

as derived in Eq. 5.7.

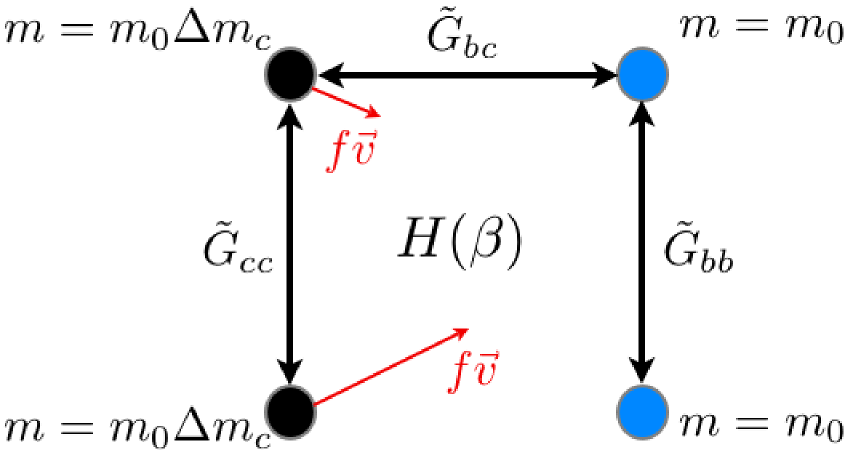

Figure 5.7: Schematic representation of the possible particle-particle interactions in our N-body simulations and of all the implemented modifications of the code GADGET-2 extensively discussed in this Chapter.

5.7 Tests of the numerical implementation: the linear growth factor

As a first test of our implementation we check whether the linear growth of density fluctuations in the simulations is in agreement with the linear theory prediction for each coupled dark energy model under investigation. To do so, we compute the growth factor from the simulation outputs of the low-resolution simulations described in Table 5.2 by evaluating the change in the amplitude of the matter power spectrum on very large scales, and we compare it with the solution of the system of coupled equations for linear perturbations 3.47, numerically integrated with CMBEASY. The comparison is shown in Fig. 5.8 for all the constant coupling models. The accuracy of the linear growth computed

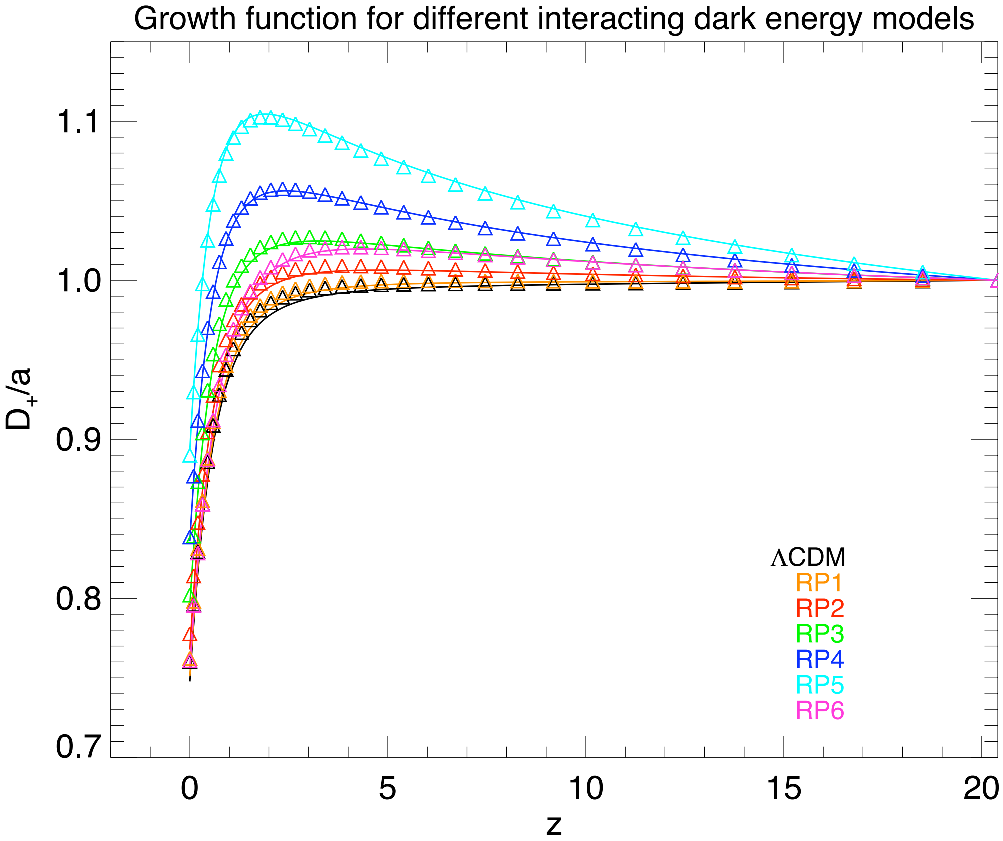

Figure 5.8: Evolution of the growth function with redshift for the seven models of coupled dark energy investigated with the low-resolution simulations ran with our modified version of GADGET-2. The solid lines are the total growth functions as evaluated numerically with CMBEASY, while the triangles are the growth functions evaluated from the simulations. The relative accuracy in reproducing the theoretical prediction is of the order of a few percent, irrespective of the coupling value β_c.

from the simulations in fitting the theoretical prediction is of the same order for all the values of the coupling, and the discrepancy with respect to the numerical solution obtained with our modified version of GADGET-2 never exceeds a few percent.

Chapter 6

The N-body simulations

6.1 Our set of N-body simulations

In our simulations, we are especially interested in the effects that the presence of a coupling between dark energy and cold dark matter induces in the properties of collapsed structures, and we would like to understand which of these effects are due to linear features of the coupled theory, and which are due to the modified gravitational interaction in the dark sector. This goal turns out to be challenging due to the presence of several different sources of changes in the simulation outcomes within our set of runs. To summarize this, let us briefly discuss in which respect, besides the different gravitational interactions, the high-resolution simulations listed in Table 5.2 are different from each other:

- the initial conditions of the simulations are generated using a different matter power spectrum for each model, i.e. the influence of the coupled dark energy on the initial power spectrum is taken into account and this means that every simulation will have a slightly different initial power spectrum shape;
- the amplitude of density fluctuations is normalized at $z = 0$ for all the simulations to $\sigma_8 = 0.796$, but due to the different shapes of the individual power spectra the amplitude of density fluctuations at the present time will not be the same in all simulations at all scales;
- the initial displacement of particles is computed for each simulation by scaling down the individual power spectrum amplitudes as normalized at $z = 0$ to the initial redshift of the simulations ($z_i = 60$) by using for each simulation the appropriate growth function. This results in a lower initial amplitude for more strongly coupled

models;

- hydrodynamical forces are acting on baryon particles in all the four fully self-consistent simulations (ΛCDM, RP1, RP2, RP5), and therefore differences in the evolution of the dark matter and baryon distributions might be due to a superposition of hydrodynamics and modified gravitational interaction.

In order to try to disentangle which of these differences cause significant changes in our results, we decided to run three further test simulations in which, in turn, some of the new physics has been disabled.

- In the two simulations labelled as "NO-SPH" (ΛCDM-NO-SPH, RP5-NO-SPH), we disabled hydrodynamical SPH (Smoothed Particle Hydrodynamics) forces in the code integration. We can then compare a ΛCDM model with a strongly coupled model treating both baryons and cold dark matter particles as collisionless particles. The differences in the dynamics will then be due only to the different gravitational interaction implemented in the RP5 model. However, the shape and amplitude of the initial power spectrum for the two simulations are still different;
- In the simulation labelled RP5-NO-GF, we ran a RP5 cosmological model using as initial conditions the same file we used for the ΛCDM run. This means that no effect arising in this simulation compared to ΛCDM can be due to different initial conditions, i.e. due to the differences in the shape and amplitude of the initial power spectra that are present in the other simulations.

6.2 The results

We now describe our results for the effect of the coupling between dark energy and cold dark matter on non-linear structures. As first basic analysis steps we apply the Friends-of-Friends (FoF) and SUBFIND algorithms (Springel et al., 2001) to identify groups and gravitationally bound subgroups in each of our simulations. Given that the seed used for the random realization of the power spectrum in the initial conditions is the same for all the seven simulations, structures will form roughly at the same positions in all simulations, as can be seen from Figs. 6.1,6.2 and it is hence possible to identify the same objects in all the simulations and to compare their properties. Nevertheless, due to the different timestepping induced by the different physics implemented in each run, and the slightly different transfer functions, objects in the different simulations can be slightly offset from each other. We therefore apply a selection criterion and identify objects found in the different simulations as the same structure only if the most bound particle of each of them lies within the virial radius of the corresponding structure in the ΛCDM simulation. If this criterion is not fulfilled for all the different simulations we want to compare, we do not consider the corresponding halo in any of the comparison analysis described below. We restrict this matching procedure to the 200 most massive halos identified by the FoF algorithm, which have virial masses ranging from $4.64 \times 10^{12} h^{-1} M_{\odot}$ to $2.83 \times 10^{14} h^{-1} M_{\odot}$. Note that depending on the specific set of simulations we consider in our comparative analysis, this can result in small differences in the number of halos included in each of the comparison samples.

6.3 Halo mass function

For the four fully self-consistent high-resolution simulations listed in Table 5.2 (ΛCDM, RP1, RP2, RP5), we have computed the halo mass function based on the groups identified with the Friends-of-Friends (FoF) algorithm with a linking length of $\lambda = 0.2 \times \bar{d}$, where $\bar{d}$ is the mean particle spacing. It is important to recall that our simulations have the same initial random phases and are normalized to the same σ_8 today, but the shapes of the input power spectra are slightly different for each simulation. In Figs. 6.3,6.4 we plot the cumulative mass functions for the four simulations at different redshifts. Remarkably, the mass functions of all the cosmological models and at all the different redshifts considered are well fit by the formula given in Jenkins et al. (2001), provided it is evaluated with the actual power spectrum and the correct linear growth factor for the corresponding cosmological model. The usual mass function formalism hence continues to work even for coupled dark energy cosmologies, a result in line with recent findings for early dark energy cosmologies (Grossi and Springel, 2008).

We also plot in Figs. 6.5,6.6 the multiplicity function, defined as the derivative of the mass function with respect to the mass ($M^2/\rho \cdot \mathrm{d}n(< M)/\mathrm{d}M$), for each simulation at different redshifts. This more sensitive representation of the mass function reveals a slightly better agreement with the formula by Sheth and Tormen (1999) compared with

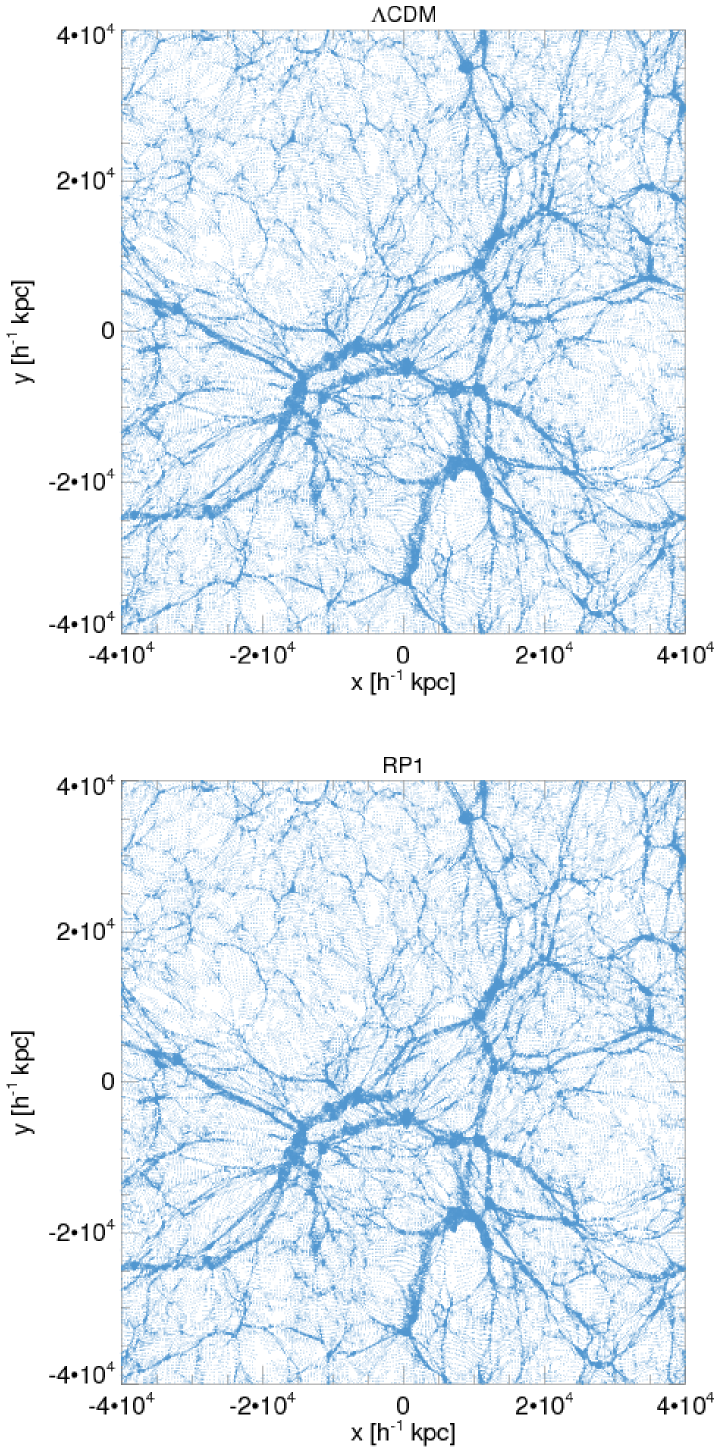

Figure 6.1: Projection on the x-y plane of the cold dark matter particles in the simulation box which lie within a slice of thickness $300h^{-1}$kpc perpendicular to the z axis, for the simulations ΛCDM and RP1. As a consequence of the choice of the same random phases for the initial conditions in the different runs the large scale structure looks the same for the two plots, and also in comparison with the plots of Fig. 6.2 in the next page.

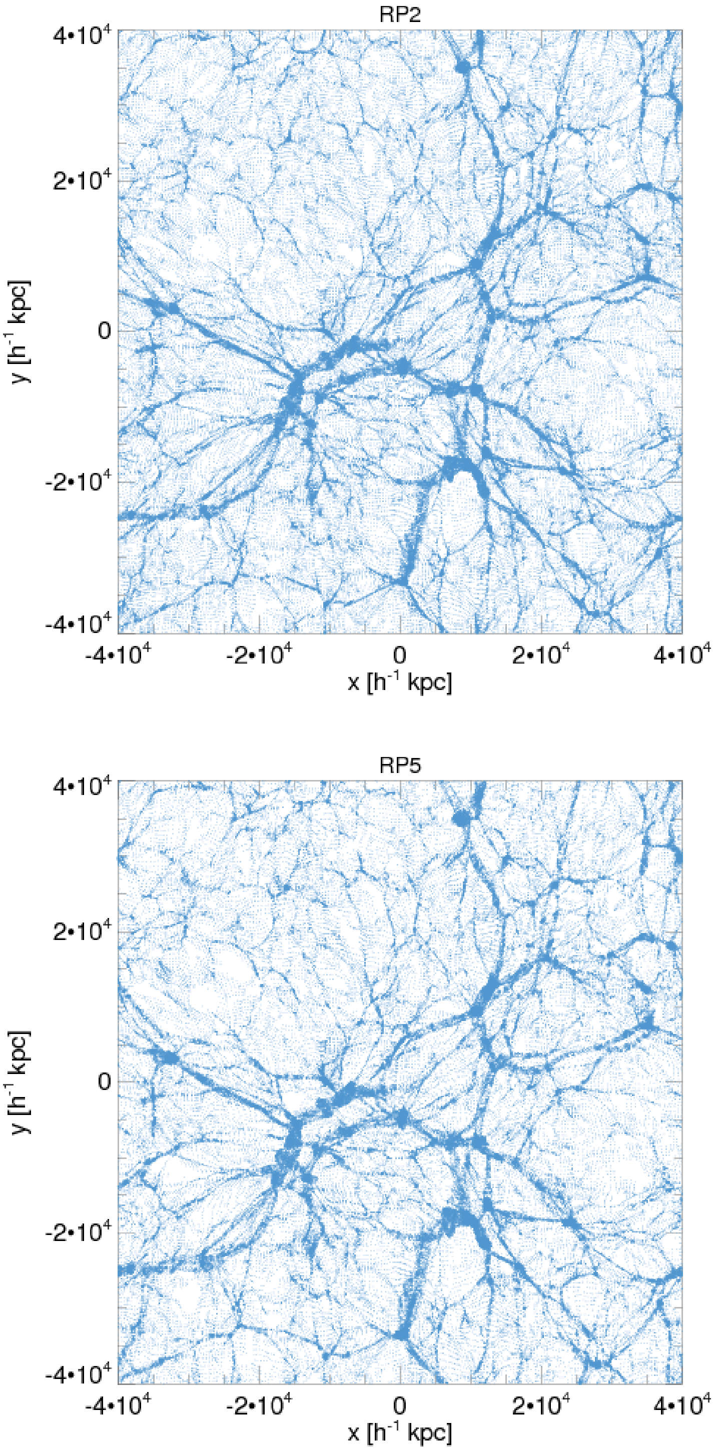

Figure 6.2: Projection on the x-y plane of the cold dark matter particles in the simulation box which lie within a slice of thickness $300h^{-1}$kpc perpendicular to the z axis, for the simulations RP2 and RP5. As a consequence of the choice of the same random phases for the initial conditions in the different runs the large scale structure looks the same for the two plots, and also in comparison with the plots of Fig. 6.1 in the previous page.

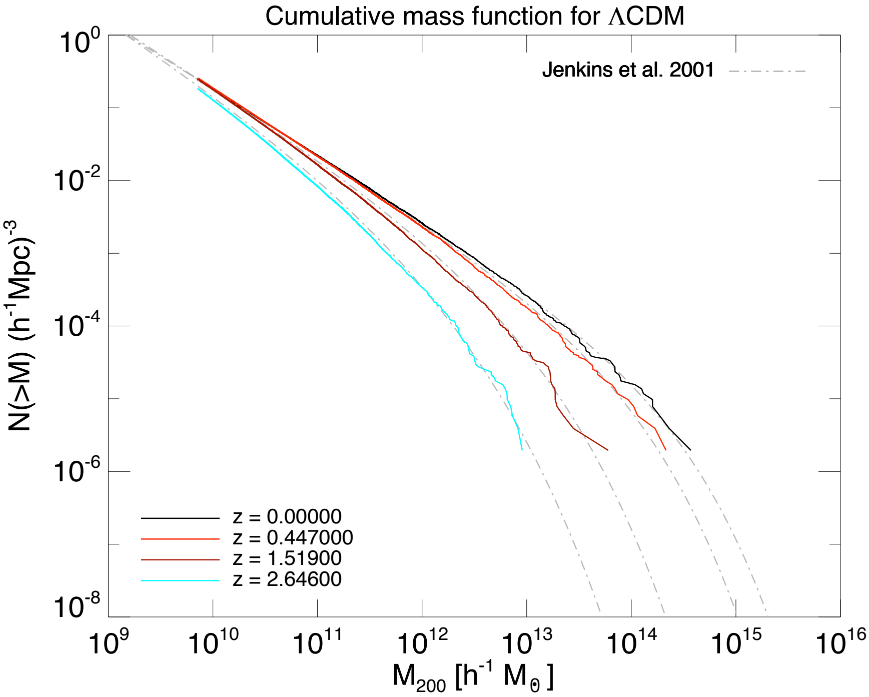

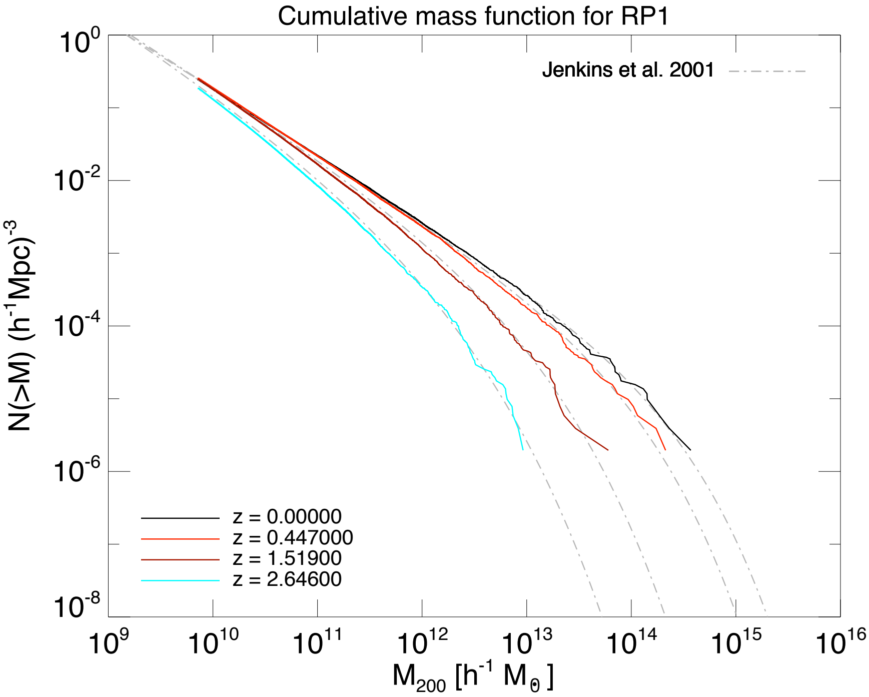

Figure 6.3: Cumulative mass functions for the fully self-consistent high-resolution simulations of the models ΛCDM and RP1. The four differently-colored solid lines in each figure represent the cumulative mass function at four different redshifts in each of the investigated models. The dot-dashed lines are the corresponding predictions according to the Jenkins et al. (2001) formula, computed for each simulation with the appropriate growth function and power spectrum.

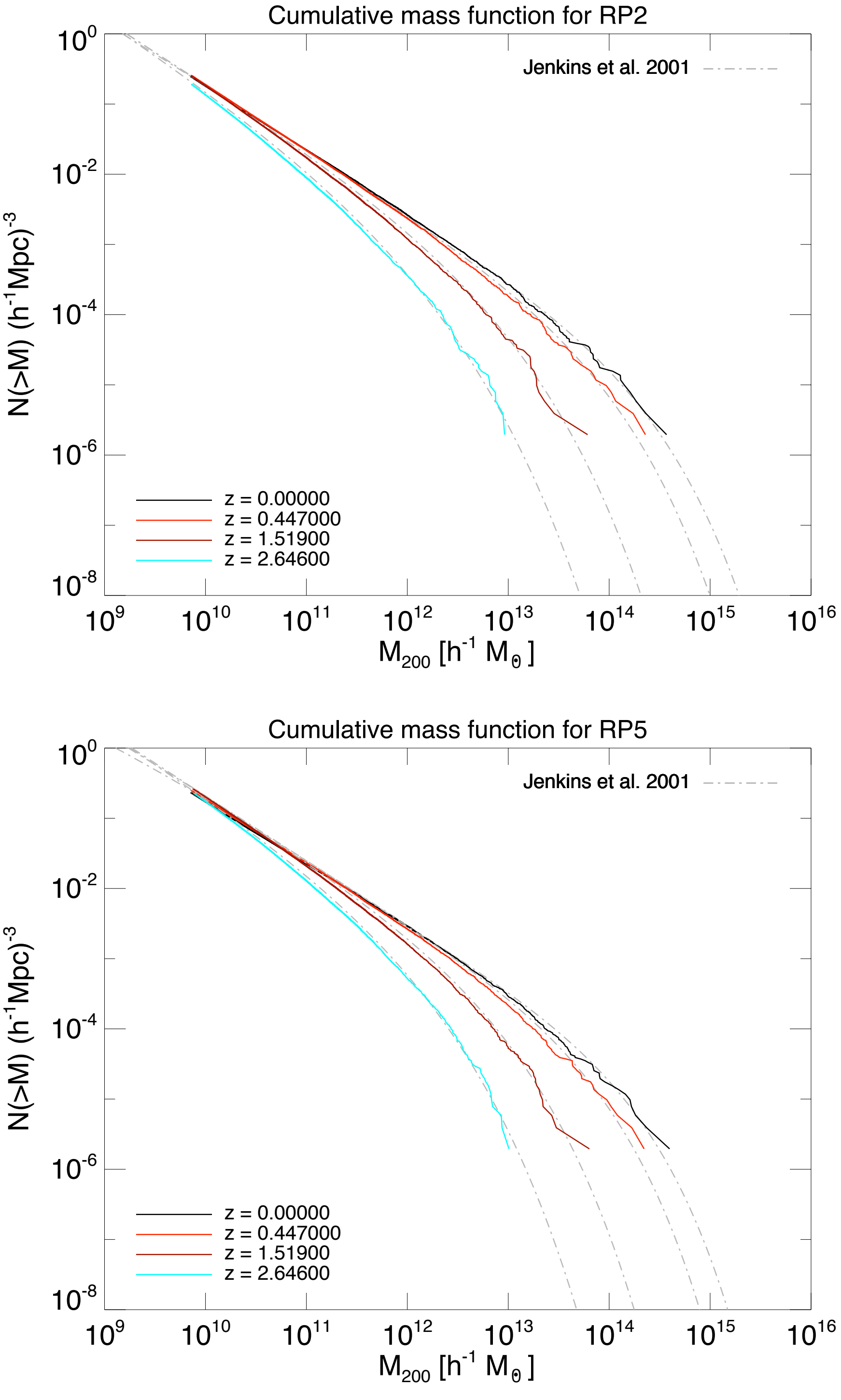

Figure 6.4: Cumulative mass functions for the fully self-consistent high-resolution simulations of the models RP2 and RP5. The four differently-colored solid lines in each figure represent the cumulative mass function at four different redshifts in each of the investigated models. The dot-dashed lines are the corresponding predictions according to the Jenkins et al. (2001) formula, computed for each simulation with the appropriate growth function and power spectrum.

that of Jenkins et al. (2001), which are both overplotted for a direct comparison.

6.4 Matter power spectrum

The presence of a long-range fifth-force acting only between cold dark matter particles induces a linear bias on all scales between the amplitude of density fluctuations in baryons and cold dark matter. These density fluctuations, in fact, start with the same relative amplitude in the initial conditions of all the simulations, and then grow at a different rate due to the presence of the extra force. Such a bias is then easily distinguishable from the hydrodynamical bias that develops only at small scales as structure evolves. This effect is clearly visible in our simulations, as can be seen from the baryon and cold dark matter power spectra at $z = 0$ in the four different cosmologies we analyze (Fig. 6.7): the density power spectra of baryons and cold dark matter end up with a different amplitude on all scales at $z = 0$ in the coupled dark energy models. Cold dark matter always has a larger amplitude, and the difference grows with increasing coupling β_c.

In order to disentangle this effect from the small scale bias due to pressure forces acting on baryons, we can make use of our “NO-SPH” simulations to show the result if only the fifth-force effect is included. This is shown in the last two panels of Fig. 6.7.

In order to make the effect described above even more visible, and to better show the difference of the hydrodynamical bias from the gravitational one induced by the coupled dark energy component, we also plot in Figs. 6.8,6.9 the ratio of the power $\Delta^2(k) = P(k)k^3/2\pi$ in baryons to that in cold dark matter at different redshifts. In these plots, we have corrected all the curves for a spurious effect on small scales due to the mass difference between baryon and cold dark matter particles in the simulations that induces a small drop in the baryon power. This effect is of purely numerical origin and could be easily removed by using particles of equal mass for the two cosmological matter species in the N-body runs.

Let us now briefly comment on the plots of Figs. 6.8,6.9. The curves represent the bias between the baryon and the cold dark matter density fluctuation amplitudes as a function of the wave number. A constant bias of 1.0 at all redshifts is the expected result for two collisionless matter species interacting with the same gravitational strength, and this is what we find for our ΛCDM-NO-SPH simulation (dark blue curve). In the

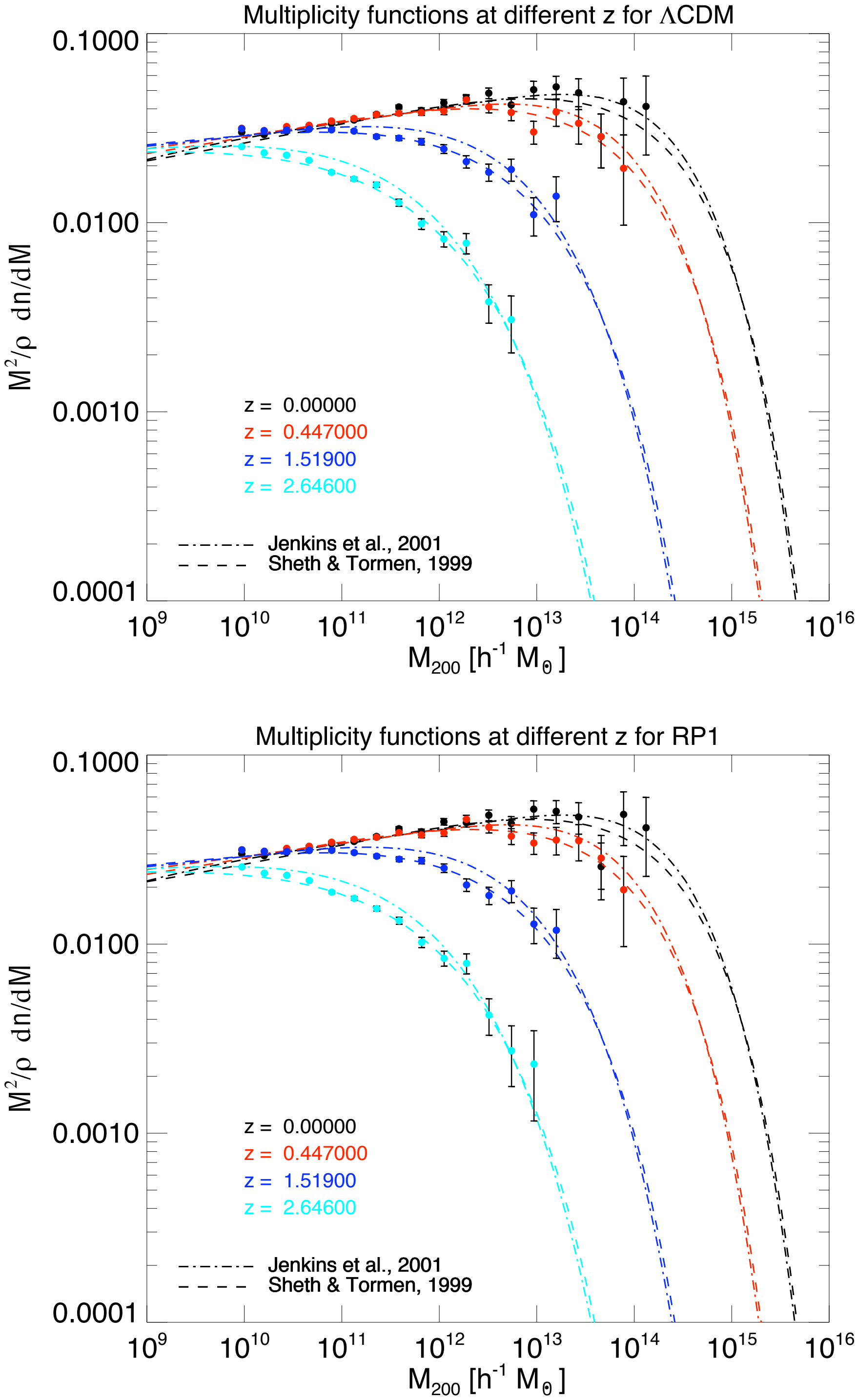

Figure 6.5: Multiplicity functions for the high-resolution simulations of the models ΛCDM and RP1. The four differently-colored sets of data points are the multiplicity functions evaluated in equally spaced logarithmic mass bins at four different redshifts. The dot-dashed and dashed lines represent the predictions for the multiplicity function from Jenkins et al. (2001) and Sheth and Tormen (1999), respectively, computed for each simulation with the appropriate growth function and power spectrum. The comparison clearly shows a slightly better agreement with the fitting function by Sheth and Tormen (1999), in particular at high redshift.

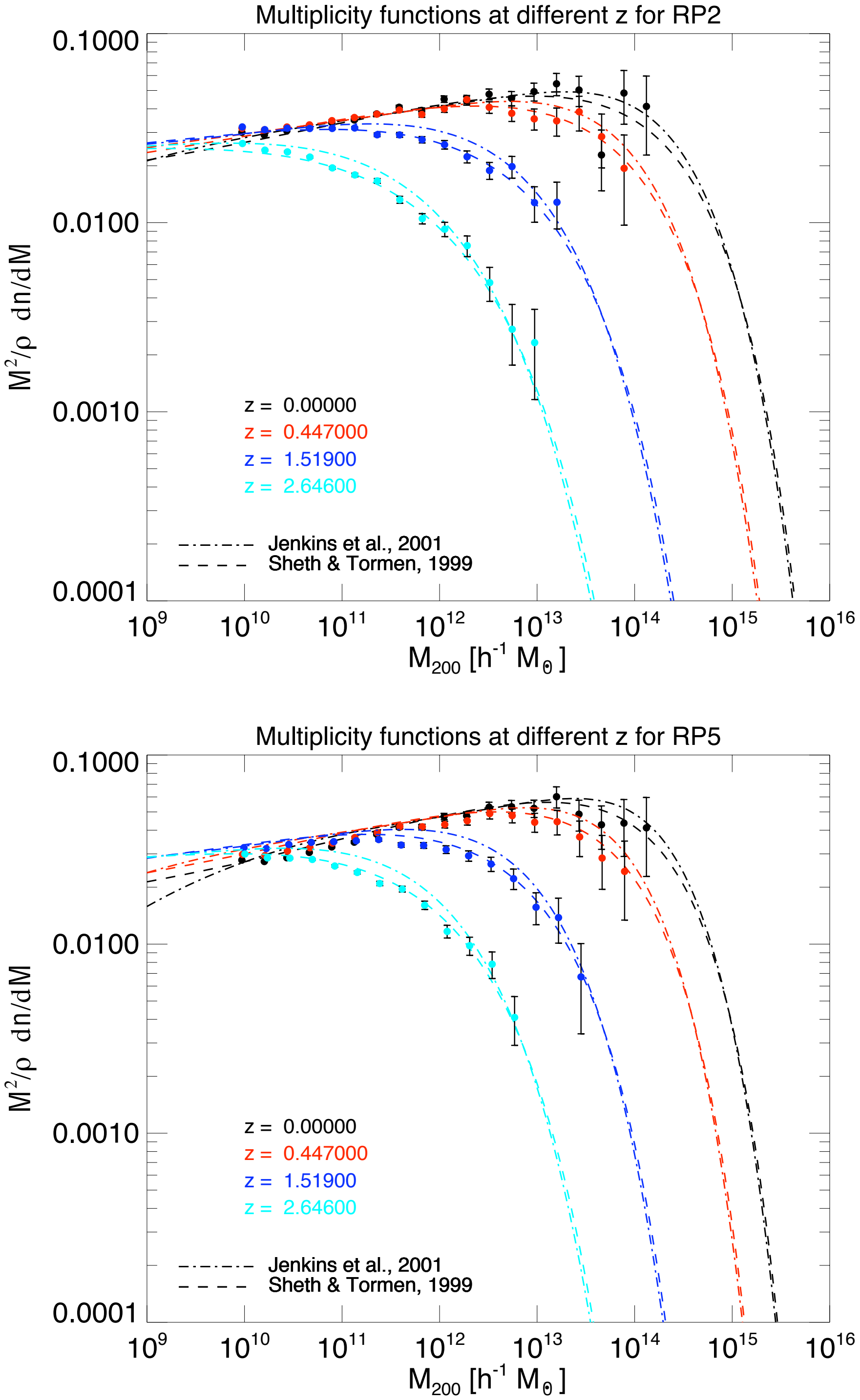

Figure 6.6: Multiplicity functions for the high-resolution simulations of the models RP2 and RP5. The four differently-colored sets of data points are the multiplicity functions evaluated in equally spaced logarithmic mass bins at four different redshifts. The dot-dashed and dashed lines represent the predictions for the multiplicity function from Jenkins et al. (2001) and Sheth and Tormen (1999), respectively, computed for each simulation with the appropriate growth function and power spectrum. The comparison clearly shows a slightly better agreement with the fitting function by Sheth and Tormen (1999), in particular at high redshift.

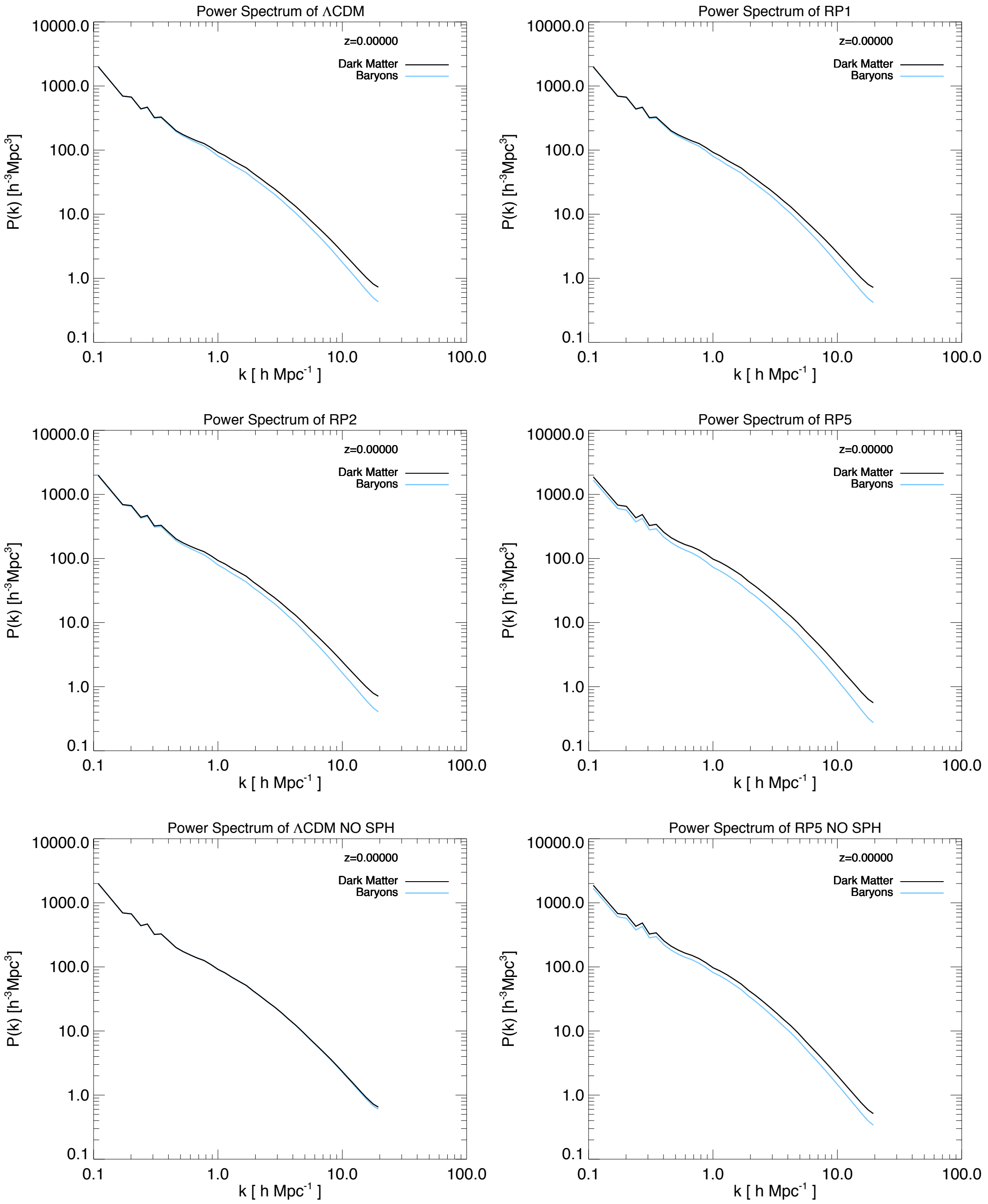
Power Spectrum of ΛCDM

Power Spectrum of RP1

Power Spectrum of RP2

Power Spectrum of RP5

Power Spectrum of ΛCDM NO SPH

Power Spectrum of RP5 NO SPH

Figure 6.7: Power spectra of cold dark matter (black line) and baryons (blue line) at $z = 0$ for the set of coupled dark energy models under investigation. The appearance of a bias between the two distributions, which grows with increasing coupling β_c, is clearly visible at the large scale end of the plots. The last two panels show the comparison of a ΛCDM and a coupled dark energy cosmology with $\beta_c = 0.2$ in absence of hydrodynamic forces acting on baryons. In these two panels, the bias on all scales is purely due to the interaction of cold dark matter with the dark energy scalar field ϕ.

ΛCDM simulation, we notice that this value of 1.0 is maintained at all redshifts only for large scales, while on smaller scales, as structures evolve, the collisional nature of baryon particles progressively induces a drop of this ratio (black curve). The same behavior is seen for all the other hydrodynamic simulations (RP1, RP2, RP5). However, in the latter cases, the large-scale bias is always smaller than 1.0, already at high redshifts, and it decreases with increasing values of the cold dark matter coupling β_c, as expected. This is the gravitational bias that appears also at large scales in Fig. 6.7.

Particularly interesting is then again the case of the RP5-NO-SPH simulation (dark-green curve), as compared to the ΛCDM-NO-SPH one, because it allows us to disentangle the hydrodynamic effects from the effects due to the coupled dark energy extra physics. In this case we find that the bias of RP5-NO-SPH perfectly overlaps with the one of the other two RP5 simulations at high redshifts, while at lower and lower redshifts, the small scale behavior is progressively more and more different: as expected, the absence of hydrodynamic forces acting on baryon particles induces a larger value of the bias, which is now solely due to the different gravitational strength felt by the two particle species. It is however very interesting to notice that the bias does not keep the large-scale linear value at all scales, as it is the case for the ΛCDM-NO-SPH run, but evolves towards lower and lower values for smaller and smaller scales.

This clearly shows that non-linearities enhance the effect of the coupling on the growth of overdensities in the two differently interacting matter species.

6.5 Halo density profiles

Applying the selection criterion described above to our four fully self-consistent simulations (ΛCDM, RP1, RP2, RP5) we select among the 200 most massive groups identified at $z = 0$ for each run 74 objects that can be considered with certainty to be the same structure in the different simulations. For these 74 halos we compute the spherically averaged density profiles of cold dark matter and baryons as a function of radius around the position of the particle with the minimum gravitational potential.

Interestingly, the halos formed in the coupled dark energy cosmologies show systematically a lower inner overdensity with respect to ΛCDM, and this effect grows with increasing coupling. This is clearly visible in Figs. 6.10,6.11 where we show the

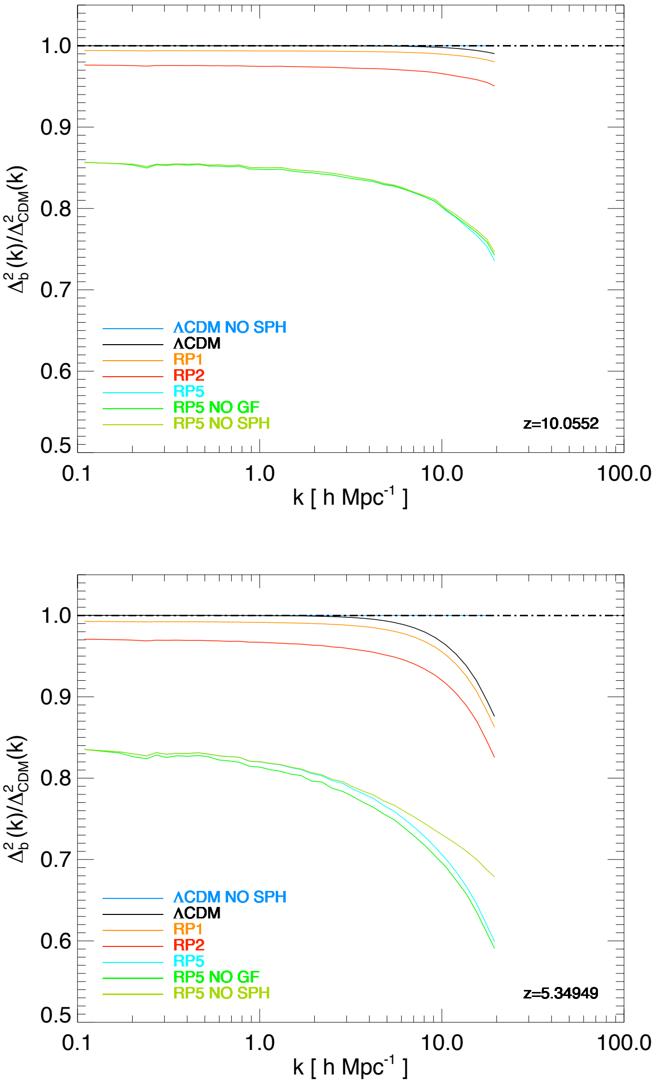

Figure 6.8: Ratio of the power spectra of baryons and cold dark matter as a function of wavenumber for the set of high-resolution simulations ran with our modified version of GADGET-2, for the redshifts $z = 10.06$ and $z = 5.35$. The linear large-scale bias appears already at high redshifts, while at lower redshifts the hydrodynamic forces start to suppress power in the baryon component at small scales. In absence of such hydrodynamic forces the progressive enhancement of the large scale bias at small scales for the RP5-NO-SPH run (light green curve) as compared to the completely flat behavior of the ΛCDM-NO-SPH simulation (blue curve) – where no bias is expected – shows clearly that non-linearities must increase the effect of the coupling on the different clustering rates of the two species. All the curves have been corrected for a spurious numerical drop of the baryonic power at small scales as described in the text.

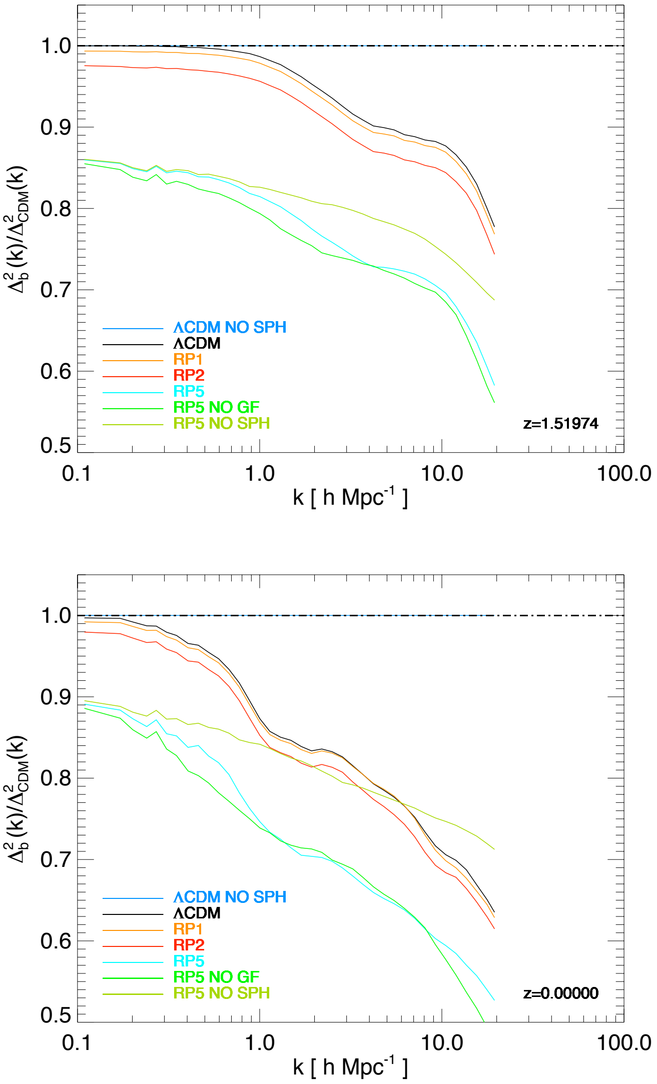

Figure 6.9: Ratio of the power spectra of baryons and cold dark matter as a function of wavenumber for the set of high-resolution simulations ran with our modified version of GADGET-2, for the redshifts $z = 1.52$, and $z = 0.0$. The linear large-scale bias appears already at high redshifts, while at lower redshifts the hydrodynamic forces start to suppress power in the baryon component at small scales. In absence of such hydrodynamic forces the progressive enhancement of the large scale bias at small scales for the RP5-NO-SPH run (light green curve) as compared to the completely flat behavior of the ΛCDM-NO-SPH simulation (blue curve) – where no bias is expected – shows clearly that non-linearities must increase the effect of the coupling on the different clustering rates of the two species. All the curves have been corrected for a spurious numerical drop of the baryonic power at small scales as described in the text.

density profiles of cold dark matter and baryons in the four different cosmologies for a few selected halos of different virial mass in our sample. We remark that this result is clearly incompatible with the essentially opposite behavior previously reported by Macciò et al. (2004). This deserves a more detailed discussion.

Unlike in Macciò et al. (2004), all the 74 halos in our comparison sample have density profiles that are well fitted by the NFW fitting function (Navarro et al., 1997)

$$\frac{\rho(r)}{\rho_{\rm crit}} = \frac{\delta^*}{(r/r_s)(1+r/r_s)^2}\,, \tag{6.1}$$

independent of the value of the coupling. Here δ^* is a parameter that sets the characteristic halo density contrast relative to the critical density $\rho_{\rm crit}$. The scale radius r_s increases for each halo with increasing coupling β_c, and becomes larger than that found in ΛCDM. In other words, the halos become *less concentrated* with increasing coupling.

For example, for the four halos shown in Figs. 6.10,6.11, the scale radius grows with increasing coupling by roughly 10% to 35% going from ΛCDM to RP5, as listed in Table 6.1, and shown in Fig. 6.12.

6.6 Halo concentrations

For all the 200 most massive halos found in each of our four fully self-consistent simulations we compute halo concentrations as

$$c = \frac{r_{200}}{r_s}\,, \tag{6.2}$$

based on our NFW fits to the halo density profiles. Here r_{200} is the radius enclosing a mean overdensity 200 times the critical density. Note that here no further selection criterion is applied, and the concentration is computed for all the 200 most massive halos in each simulation.

Consistently with the trend found for the inner overdensity in the halo density profiles and for the evolution of the scale radius with coupling, we find that halo concentrations are on average significantly lower for coupled dark energy models with respect to ΛCDM, and the effect again increases with increasing coupling β_c. This behavior is shown explicitly in the top panel of Fig. 6.13, where we plot halo concentrations as a function of the halo virial mass M_{200} for a series of our high-resolution simulations. In the standard

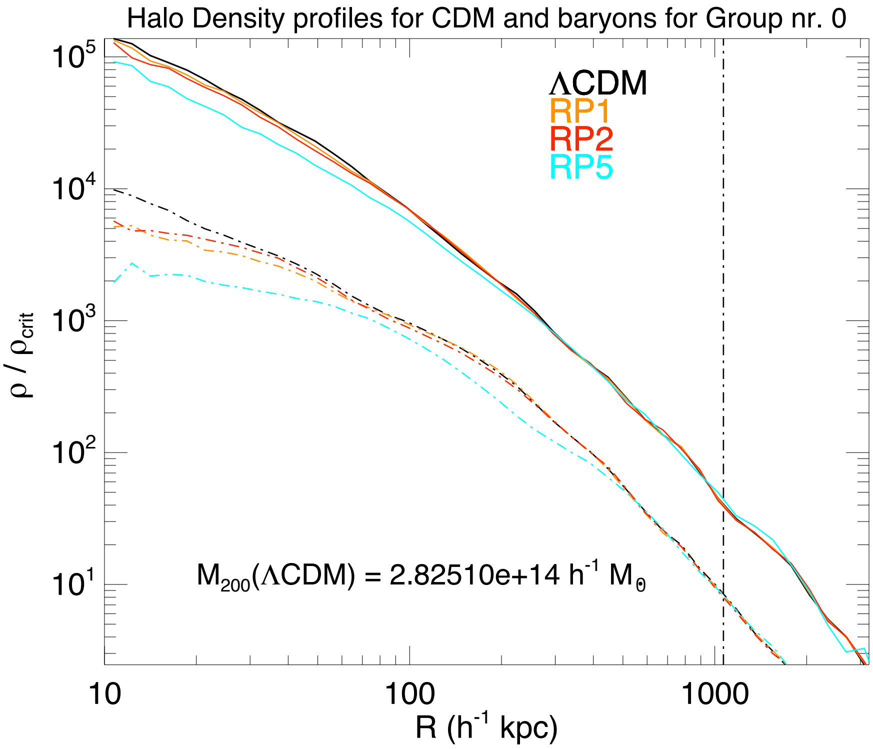

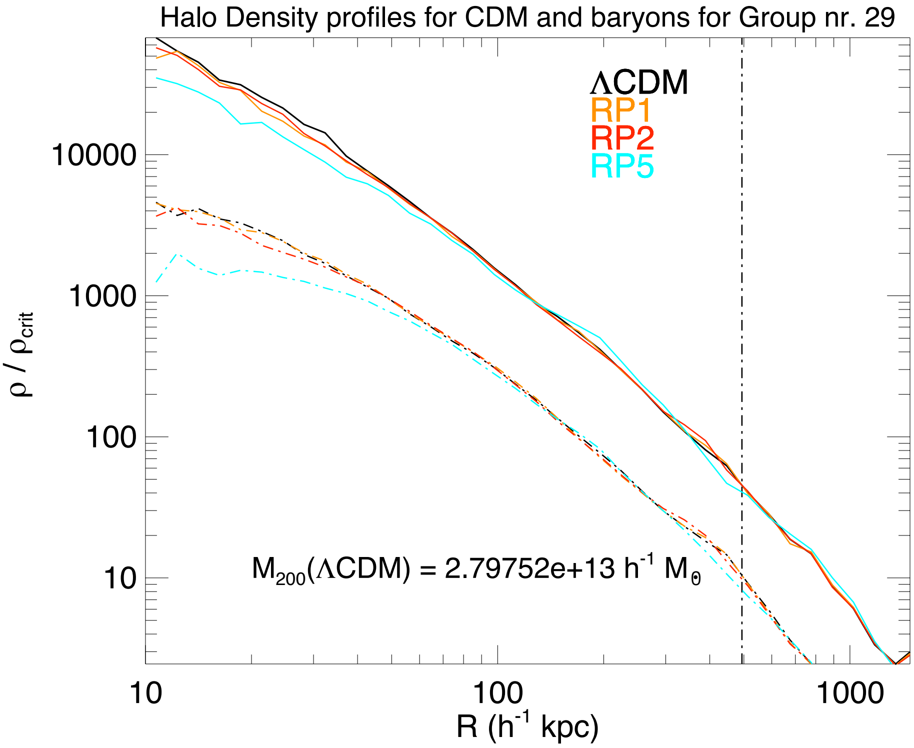

Figure 6.10: Density profiles of cold dark matter (solid lines) and baryons (dot-dashed lines) for two halos of virial masses $M_{200} = 2.83 \times 10^{14} h^{-1} M_\odot$ and $M_{200} = 2.78 \times 10^{13} h^{-1} M_\odot$ in the simulation box at $z = 0$. The vertical dot-dashed line indicates the location of the virial radius for the ΛCDM halo. The decrease of the inner overdensity of the profiles with increasing coupling is clearly visible in both plots.

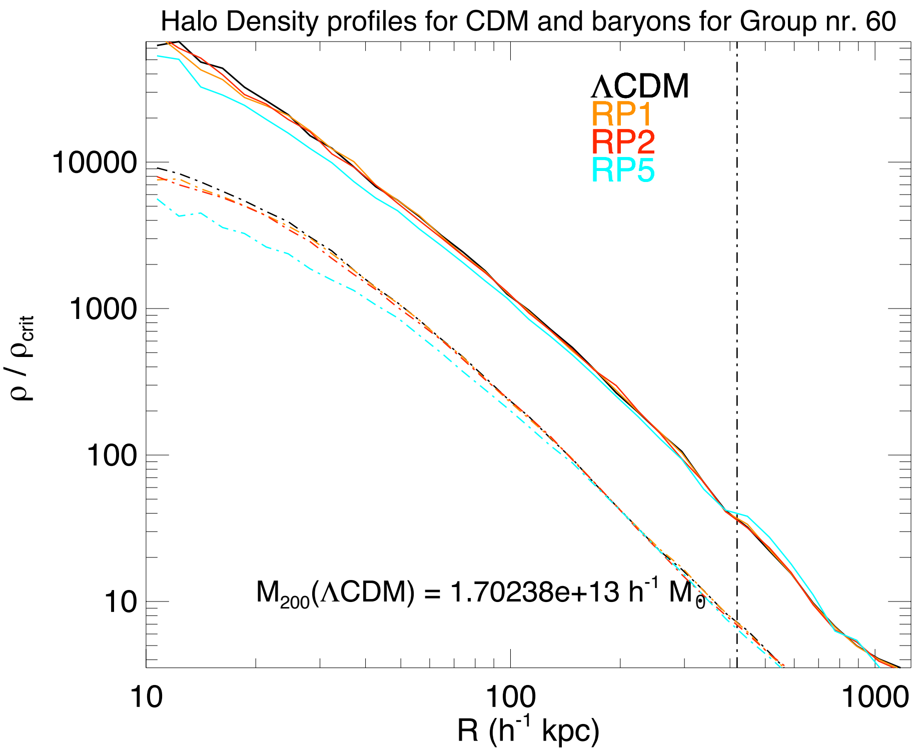

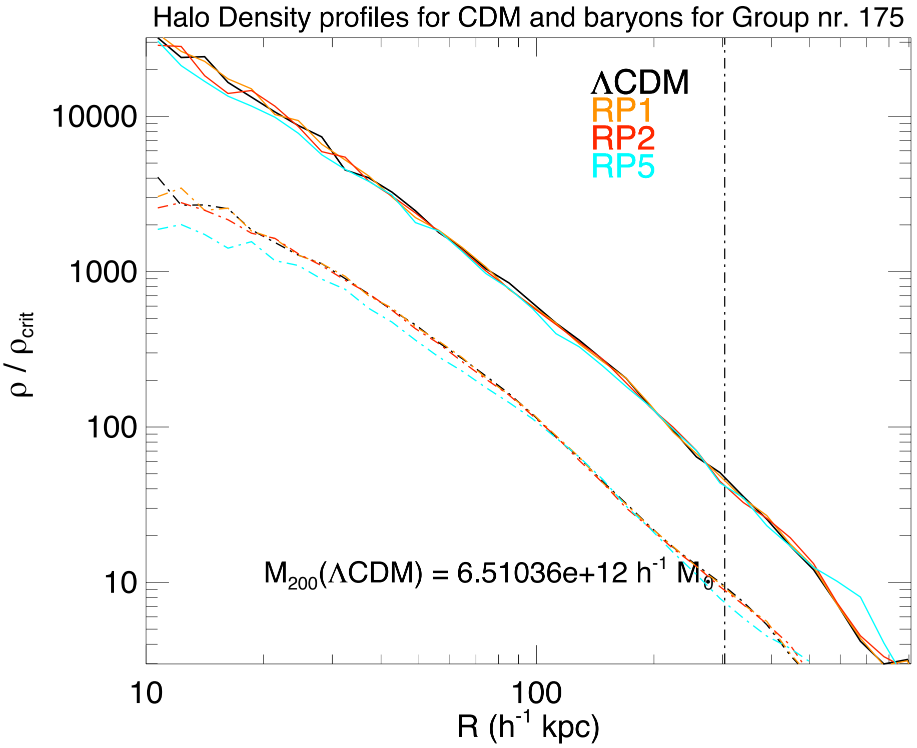

Figure 6.11: Density profiles of cold dark matter (solid lines) and baryons (dot-dashed lines) for two halos of virial masses $M_{200} = 1.7 \times 10^{13} h^{-1} M_\odot$ and $M_{200} = 6.51 \times 10^{12} h^{-1} M_\odot$ in the simulation box at $z = 0$. The vertical dot-dashed line indicates the location of the virial radius for the ΛCDM halo. The decrease of the inner overdensity of the profiles with increasing coupling is clearly visible in both plots.

	Group 0 r_s (h^{-1} kpc)	Group 0 $\frac{r_s}{r_s(\Lambda\mathrm{CDM})}$	Group 29 r_s (h^{-1} kpc)	Group 29 $\frac{r_s}{r_s(\Lambda\mathrm{CDM})}$	Group 60 r_s (h^{-1} kpc)	Group 60 $\frac{r_s}{r_s(\Lambda\mathrm{CDM})}$	Group 175 r_s (h^{-1} kpc)	Group 175 $\frac{r_s}{r_s(\Lambda\mathrm{CDM})}$
ΛCDM	225.14	1.0	105.51	1.0	61.92	1.0	70.61	1.0
RP1	229.00	1.02	120.21	1.14	61.16	0.99	67.45	0.96
RP2	233.96	1.04	119.68	1.13	63.52	1.03	70.48	1.0
RP5	295.47	1.31	143.92	1.36	73.46	1.19	76.26	1.08

Table 6.1: Evolution of the scale radius r_s for the four halos shown in Figs. 6.10,6.11 with respect to the corresponding ΛCDM value. The trend is towards larger values of r_s with increasing coupling β_c, with a relative growth of up to 36% for the largest coupling value $\beta_c = 0.2$.

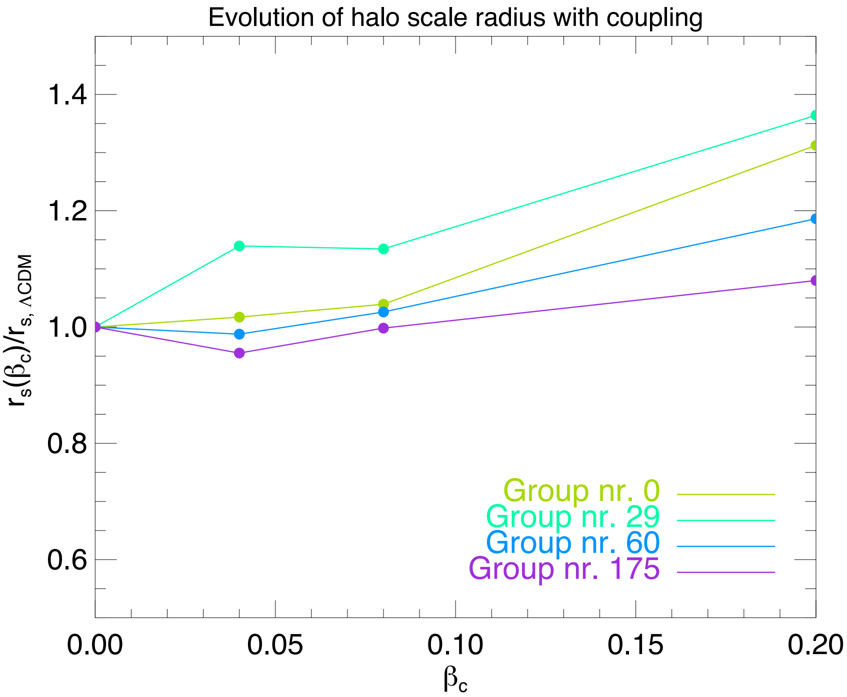

Figure 6.12: Relative variation with respect to ΛCDM of the scale radius r_s for the four halos plotted in Figs. 6.10,6.11 as a function of coupling β_c.

interpretation, the halo concentrations are thought to reflect the cosmic matter density at the time of formation of the halo, leading to the association of a larger value of the concentration with an earlier formation epoch, and vice versa. In the context of this standard picture, the effect we found for the concentrations could be interpreted as a sign of a later formation time of massive halos in the coupled dark energy models as compared to the ΛCDM model. Such a later formation time could possibly be due to the fact that matter density fluctuations start with a lower amplitude in the initial conditions of the coupled cosmologies with respect to ΛCDM, and this would make them form massive structures later, despite their faster linear growth (as shown in Fig. 5.8).

However, we can demonstrate that this is not the case, just making use of our RP5-NO-GF simulation, in which the Universe evolves according to the same physics as RP5, but starting with the identical initial conditions as used for the ΛCDM run. Therefore, any difference between these two simulations cannot be due to the initial amplitude of fluctuations. The evolution of halo concentrations with mass for this run is also plotted in the top panel of Fig. 6.13 (dark blue curve), and shows a very similar behavior to the RP5 curve.

As a cross check of this result, we have repeated the same analysis by computing halo concentrations with an independent method that circumvents the profile fitting. The concentration can be related to two other basic structural properties of a halo, namely its maximum circular velocity V_{max}, and the radius at which this velocity peak is located, r_{max}. According to Springel et al. (2008), the concentration can then be related to these two quantities by the relation:

$$\frac{200}{3}\frac{c^3}{\ln(1+c)-c/(1+c)} = 7.213\,\delta_V\,, \tag{6.3}$$

where δ_V is a simple function of V_{max} and r_{max}:

$$\delta_V = 2\left(\frac{V_{\mathrm{max}}}{H_0 r_{\mathrm{max}}}\right)^2 . \tag{6.4}$$

We denote the concentrations evaluated in this way as c^*, and include our results as a function of halo mass in the bottom panel of Fig. 6.13. Although not identical in detail, due to the different methods used to measure concentrations, the two plots of Fig. 6.13 show the same trend for the evolution of halo concentrations with coupling, and the same independence of this effect from the initial conditions of the simulations.

In order to directly verify that the lower concentrations cannot be a consequence of a later formation time, we have also computed the average formation redshift of the halos in our sample for all the four self-consistent simulations by building merger trees for all the halos in our sample, and by following backwards in time the main progenitor of each halo until the redshift at which its virial mass is only half of the final virial mass of the halo at $z = 0$. We define the corresponding time as the formation redshift z_f of the halo.

In Figure 6.14, we show z_f as a function of halo mass for all our cosmological models. It is evident that massive halos in the different cosmologies form approximately at the same time, with a slightly earlier formation for the RP5 cosmology, which one might have expected to translate into slightly larger values of the concentrations. Therefore we conclude that the unambiguous trend of lower halo concentrations for larger coupling values must be a peculiar feature that arises from the extra physics that characterizes the coupled dark energy cosmologies. A more detailed investigation of how this peculiar behavior arises is hence required in order to understand this phenomenology of the dynamics in coupled dark energy cosmologies.

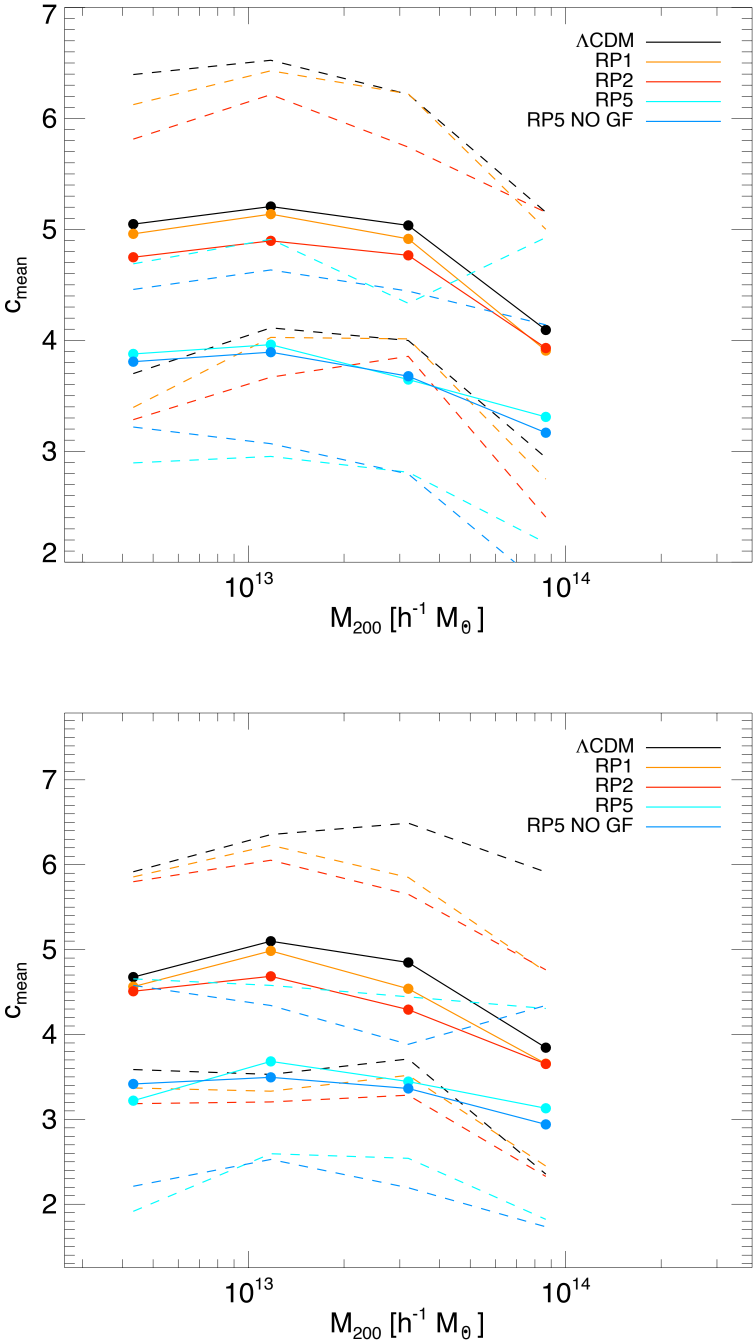

Figure 6.13: Variation of the mean halo concentration as a function of mass for the 200 most massive halos in our simulations and for the different cosmological models under investigation. The concentrations have been computed by directly fitting the halo density profile of each halo with an NFW model (*top panel*) or by using the method introduced by Springel et al. (2008) and described in Eqs. 6.3,6.4 (*bottom panel*). The halos have been binned by mass, and the mean concentration in each bin is plotted as a filled circle. The colored dashed lines indicate for each simulation the spread of 68% of the halos in each mass bin. The highest mass bin is not plotted because of its very low number of halos. The decrease of the mean concentration with increasing coupling appears in the same way in both plots.

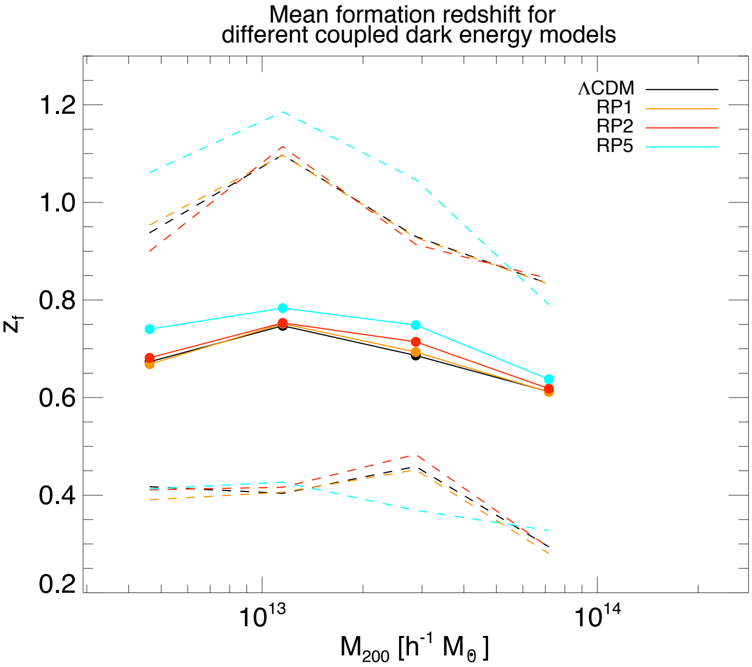

Figure 6.14: Mean halo formation redshift z_f as a function of halo mass for the 200 most massive halos in our simulations and for the different cosmological models under investigation. The formation redshift z_f is defined as the redshift at which the main progenitor of the halo has a virial mass equal to half the virial mass of the halo at $z = 0$. The halos have been binned by mass, and the mean formation redshift in each bin is plotted as a filled circle. The colored dashed lines indicate for each simulation the spread of 68% of the halos in each mass bin. The highest mass bin is not plotted because of its too low number of halos.

We perform such an investigation by switching off individually the two main effects which could be responsible of the concentration drop. These are the variation of particle mass and the extra friction term. To save computational time, we do this only for the most strongly coupled model RP5 and only for the late stages of cosmic evolution. More specifically, we take one of our RP5 simulation snapshots at a given redshift z^*, and use it as initial conditions file for a new run starting at $z = z^*$ down to $z = 0$ in which one of these two effects is switched off. We label these simulations as "RP5-NO-MASS" and "RP5-NO-FRIC" for the cases where the mass decrease or the friction term are dropped, respectively. We set $z^* = 1.5$ as a conservative choice based on the consideration that, according to our definition of formation redshift of a halo, all the halos in our sample have a formation redshift $z < z^*$, as shown in Fig. 6.14.

By switching off the mass variation for $z < z^*$, we find that the halo concentrations at $z = 0$ show a slight increase over the whole mass range of the sample with respect to the fully self-consistent RP5 simulation. This effect is shown in the top panel of Fig. 6.15. We interpret this as a sign of the fact that the mass decrease reduces the total gravitational potential energy of halos, resulting in a modification of their virial equilibrium configuration.

In fact, if the potential well of a halo gets shallower as time goes by as a consequence of the decrease of the mass of its cold dark matter content, the system will find itself with an excess of kinetic energy, and will therefore expand in order to restore virial equilibrium. Such an expansion is expected to cause a drop of the halo concentrations, which we confirm here because switching off this mechanisms yields consistently higher concentrations at $z = 0$. However, it is clear from Fig. 6.15 that this mechanism cannot account for the total effect of concentration decrease, but only for a small fraction of it.

We therefore now investigate the other possible origin of this effect, i.e. the impact of the friction term (3.57) on the dynamics of cold dark matter particles. To this end we switch off for $z < z^*$ the additional acceleration arising from the friction term for coupled particles described by Eq. 5.3. The outcome of this test simulation is shown in the bottom panel of Fig. 6.15: the increase of the concentrations with respect to the fully self-consistent RP5 simulation is now much more substantial than in the case of RP5-NO-MASS, and shows that the friction term is actually the dominant mechanism in determining the decrease of halo concentrations and the decrease of the inner overdensity

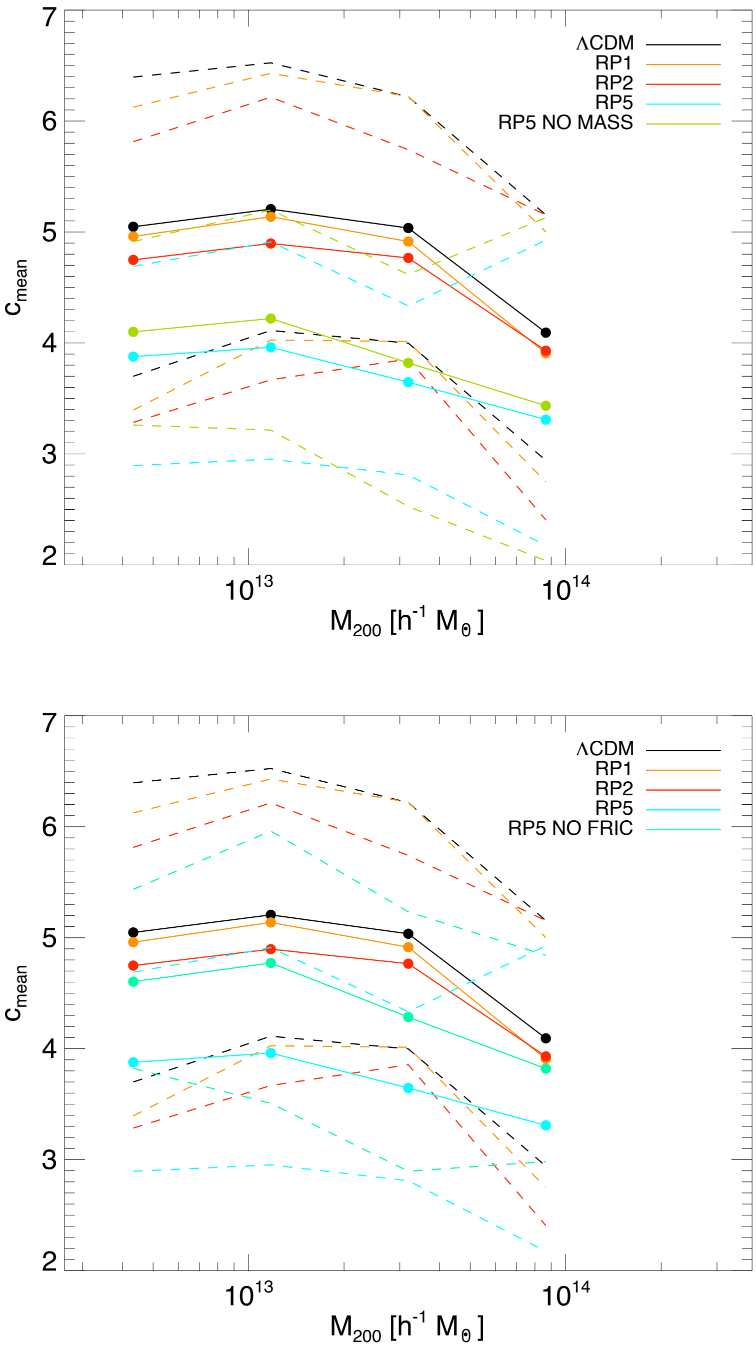

Figure 6.15: Variation of halo concentrations for the same models and the same halo sample as in Fig. 6.13, and for an additional test simulation in each of the two panels. In the *top panel*, the simulation RP5-NO-MASS shows the effect of switching off the mass correction for $z < z^* \sim 1.5$: there is a small but systematic increase of average halo concentrations over the whole mass range. In the *bottom panel*, the simulation RP5-NO-FRIC shows the effect of switching off in the same redshift interval the friction term. The increase of concentrations in this case is much more consistent and accounts for a large fraction of the total concentration reduction of RP5.

of cold dark matter halos discussed above. The interpretation of this effect seems quite unambiguous: the friction term induces an extra acceleration on coupled particles in the direction of their velocity, and this produces an increase of the total energy of the particles, moving the system out of its virial equilibrium configuration. The system responds by a small expansion and a lowering of the concentration.

As a further check of this interpretation of our results, we also test directly the dynamic evolution of halos to check whether they really slightly expand in the presence of coupling between dark energy and cold dark matter. To this end, we compute for all the halos in our sample the time evolution of the mass and the number of particles contained in a sphere of physical radius $r = 20\,h^{-1}$kpc centered on the potential minimum of each halo. This sphere represents the very innermost part of all the halos in our sample at any redshift between z^{*} and 0, and we refer to it as the halo "core"; its mass content is expected to be roughly constant for ΛCDM cosmologies at low redshifts. Indeed, we can recover this behavior for our ΛCDM simulation by averaging the evolution of core masses and particle numbers over the whole halo sample. On the other hand, for RP5, as expected according to our interpretation, both the mass and the number of particles in the halo cores strongly decrease with time. This is shown in Fig. 6.16, where the solid lines represent the average evolution of mass, and the dashed lines represent the average evolution of the particle number. Evidently, for ΛCDM the two curves coincide because the mass of the particles is constant and any change of the enclosed mass in the core must be due to a change of the number of enclosed particles. On the other hand, for RP5, the mass and the particle number behave differently due to the mass variation of cold dark matter particles. The decrease of the number of particles contained in the core can be interpreted as a manifestation of an expansion of the halos. Moreover, if we compute the same evolution for our RP5-NO-FRIC simulation, we find an almost constant evolution of the core particle number and a very weak decrease of the core mass due to the variation of cold dark matter particle mass. This result also confirms our interpretation concerning the origin of the decrease of concentrations: the friction term is the most relevant mechanism for inducing halo expansion at low redshifts, and as a consequence the decrease of the inner overdensity of cold dark matter halos and of their concentration.

While further investigation of these effects is certainly required in order to understand all the potential phenomenological features of interacting dark energy models, our

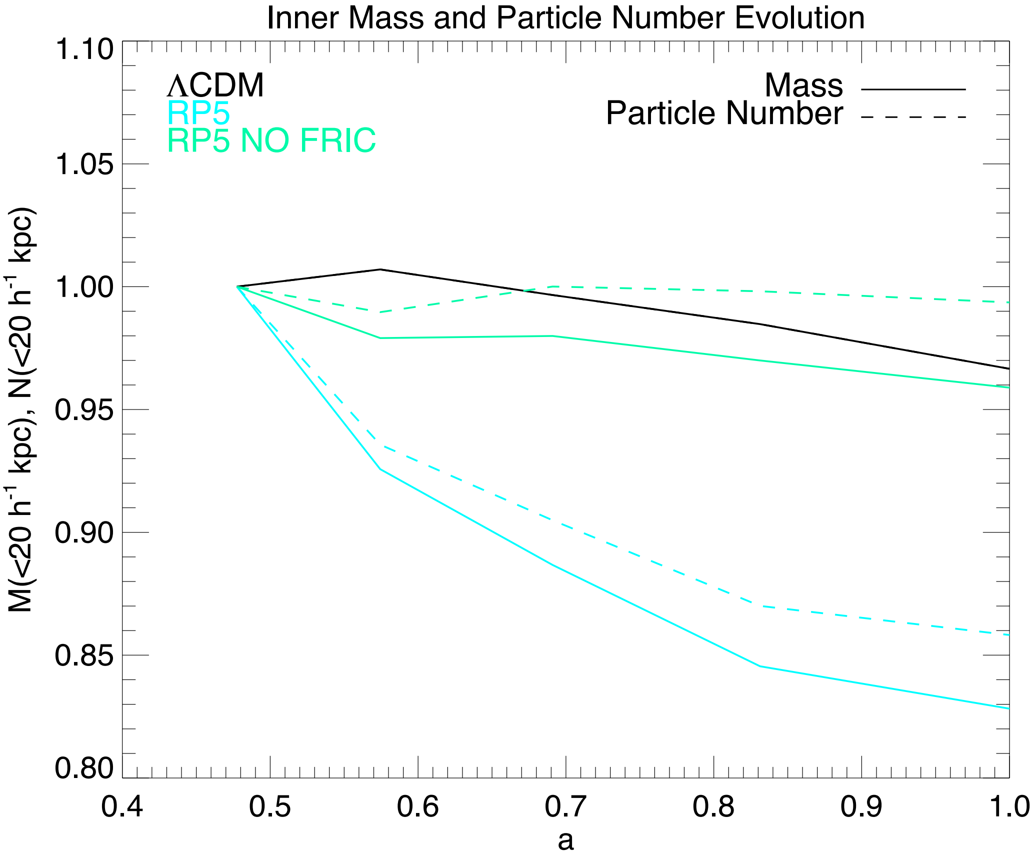

Figure 6.16: Evolution with respect to the scale factor a of the average mass (solid) and of the average number of particles (dashed) enclosed in a sphere of physical radius $r = 20h^{-1}$kpc centered on the potential minimum of each halo in our sample. The curves are normalized at $a = 0.48$ ($z \sim 1$) and show the expected flat behavior for the ΛCDM case (black line) for which the solid and the dashed curves coincide due to the constancy of the mass of particles. For the RP5 case (light blue curves), there is a strong decrease in time of both mass and particle number, which clearly illustrates the expansion of RP5 halos with respect to the ΛCDM case. By switching off the extra friction acting on cold dark matter particles (RP5-NO-FRIC, light green curves), an almost flat behavior is recovered again for the particle number, while the decrease of mass is now due to the particle mass variation – which is still in place for this simulation – on top of the particle number evolution. This plot therefore clearly shows that the extra physics of coupled dark energy cosmologies induces an overall expansion of cold dark matter halos at low redshifts, and clearly identifies the friction term as the leading mechanism that produces this expansion.

conclusion that a coupling between dark energy and cold dark matter produces less peaked halo density profiles and lower halo concentrations seems to be quite robust based on the analysis of the simulations that we have discussed here. We note again that our findings are in stark contrast with the results of previous work by Macciò et al. (2004) who found for coupled dark energy models a strong increase in concentration and density profiles in the centre that more steeply rise than in the ΛCDM cosmology.

The effects we find go in the direction of less "cuspyness" of halo density profiles, which is preferred by observations of low-mass halos and thus in fact opens up new room for the phenomenology of interacting dark energy models.

6.7 Integrated bias and halo baryon fraction

The extra force felt by cold dark matter particles induces, as we have already seen for the evolution of the matter power spectrum, a bias in the evolution of density fluctuations of baryons and cold dark matter (Mainini, 2005; Mainini and Bonometto, 2006). We can then use our selected halo sample to test the evolution of this bias from the linear regime already probed by the power spectrum on large scales to the highly non-linear regime in the centre of massive collapsed structures. We then test the evolution of the integrated bias

$$B(< r) \equiv \frac{\rho_b(< r) - \bar{\rho}_b}{\bar{\rho}_b} \cdot \frac{\bar{\rho}_c}{\rho_c(< r) - \bar{\rho}_c}\,, \tag{6.5}$$

as defined in Macciò et al. (2004), where $\rho_b(< r)$ and $\rho_c(< r)$ are the densities within a sphere of radius r around the potential minimum of a halo, for baryons and cold dark matter, respectively, and $\bar{\rho}_b$ and $\bar{\rho}_c$ are the cosmic mean densities in the two components. Following Macciò et al. (2004), we have not used the innermost part of the halos ($r < 10h^{-1}\mathrm{kpc} \sim 3 \times \epsilon_s$) in order to avoid potential resolution problems.

In Figs. 6.17,6.18, we show the evolution of the bias for four selected halos of our sample with similar masses to the ones shown in Figs. 6.10,6.11. It clearly appears that the bias is considerably enhanced in the non-linear regime, while at large scales it converges to the linear value evaluated from the power spectrum amplitude on large scales, represented in Figs. 6.17,6.18 by the horizontal dashed lines.

However, also in this case this effect could be due only to the presence of hydrodynamical forces acting on the baryons, and may not really be caused by the fifth-

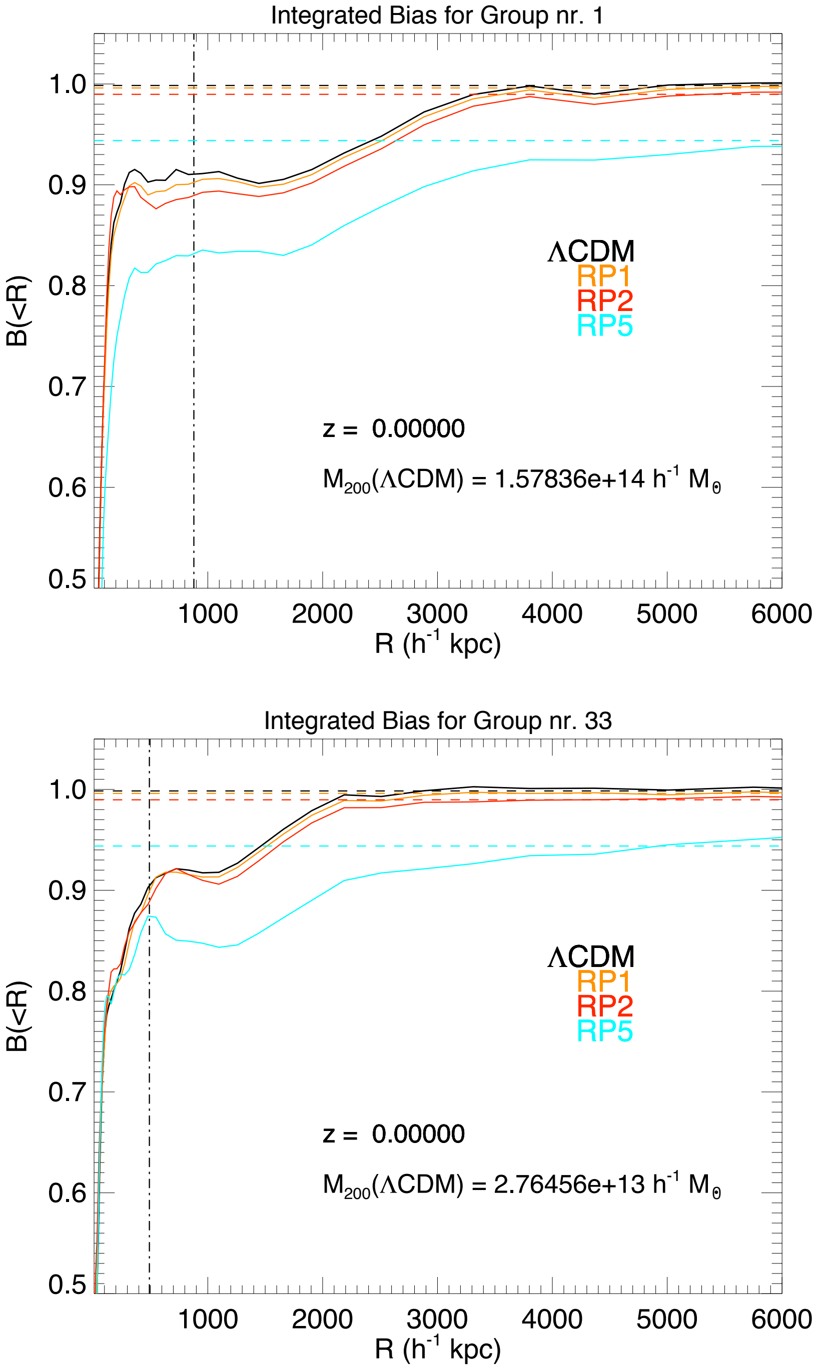

Figure 6.17: Variation of the integrated bias $B(< r)$ for the four fully self-consistent high-resolution simulations and for two selected halos of mass $M_{200} = 1.58 \times 10^{14} h^{-1} M_{\odot}$ and $M_{200} = 2.76 \times 10^{13} h^{-1} M_{\odot}$ in our sample. The horizontal dashed lines indicate the value of the large scale linear bias as evaluated from the power spectrum amplitudes of baryons and cold dark matter. The vertical black dot-dashed line shows the position of the virial radius for the ΛCDM halo in the sample. The drop of the value of $B(< r)$ in the innermost regions of the halos is evident but in these runs is given by a superposition of effects due to hydrodynamical forces and to the modified gravitational interaction. On large scales, the bias tends to converge to the linear value, as expected.

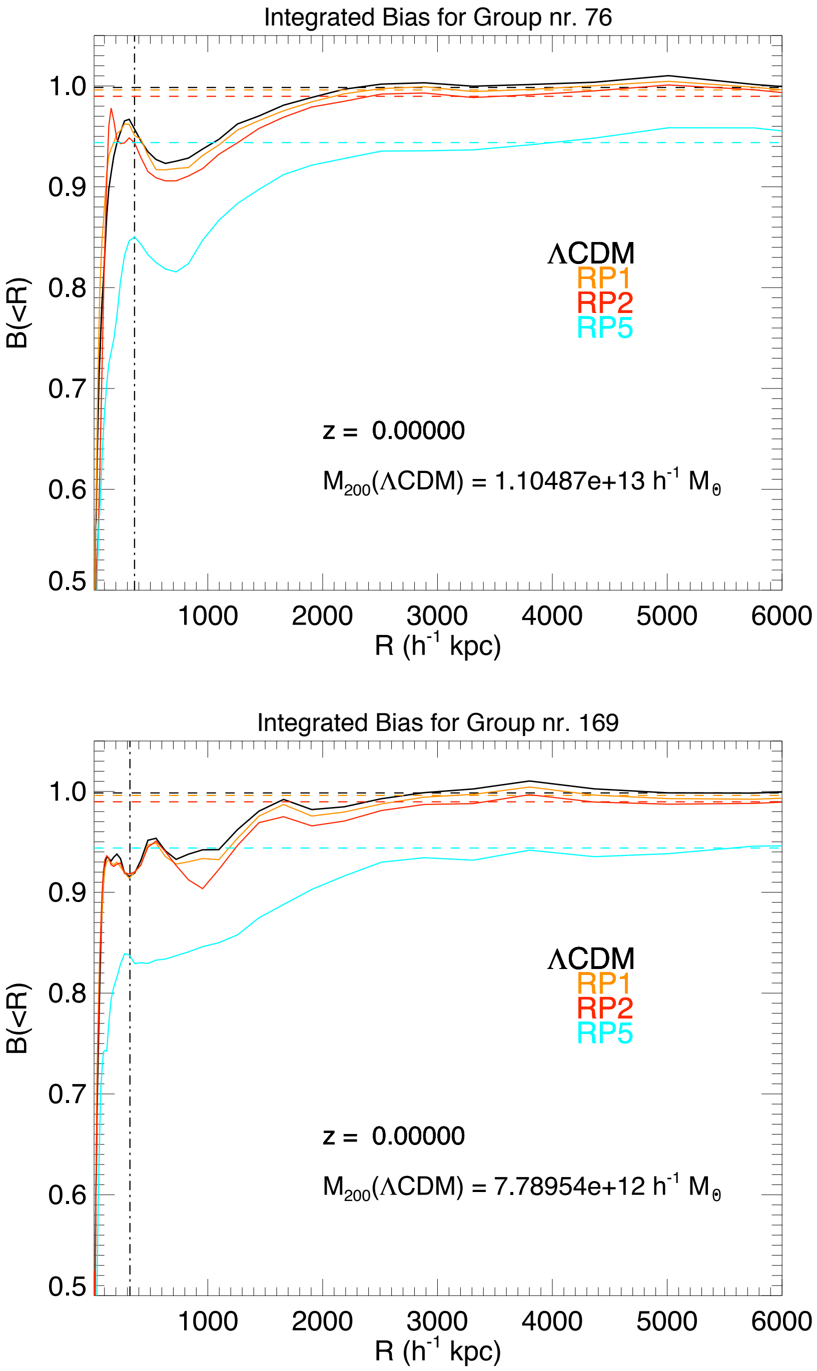

Figure 6.18: Variation of the integrated bias $B(< r)$ for the four fully self-consistent high-resolution simulations and for two selected halos of mass $M_{200} = 1.10 \times 10^{13} h^{-1} M_{\odot}$ and $M_{200} = 7.79 \times 10^{12} h^{-1} M_{\odot}$ in our sample. The horizontal dashed lines indicate the value of the large scale linear bias as evaluated from the power spectrum amplitudes of baryons and cold dark matter. The vertical black dot-dashed line shows the position of the virial radius for the ΛCDM halo in the sample. The drop of the value of $B(< r)$ in the innermost regions of the halos is evident but in these runs is given by a superposition of effects due to hydrodynamical forces and to the modified gravitational interaction. On large scales, the bias tends to converge to the linear value, as expected.

forces from the coupled dark energy scalar field, as we can infer from the fact that also the ΛCDM curve, where no coupled dark energy is present, shows a departure from the large scale value of 1.0 when approaching the centre of the halos. Once again we make use of our additional test simulations ΛCDM-NO-SPH and RP5-NO-SPH in order to disentangle the two effects. In Figs. 6.19,6.20 we show the same four plots as in Fig. 6.17,6.18 for the two simulations without hydrodynamic forces, and the appearance of a non-linear bias imprinted only by the coupled dark energy scalar field acting on cold dark matter particles is then absolutely evident. On the other hand, the absence of any bias, as expected, in the ΛCDM-NO-SPH run shows clearly that no major numerical problems can be responsible for the effect in the RP5-NO-SPH simulations.

It is interesting that the above effect produces a baryon deficit in virialized halos, i.e. they contain fewer baryons than expected based on their mass and the universal cosmological baryon fraction. In particular, this means that one cannot expect that baryon fractions determined through X-ray measurements in clusters would yield the cosmological value. In order to give a rough estimate of the magnitude of the discrepancy we compute the baryon fraction within the virial radius r_{200} of all the halos in our sample defined as

$$f_b \equiv \frac{M_b(< r_{200})}{M_{\rm tot}(< r_{200})} \tag{6.6}$$

for our four fully self-consistent simulations. We plot in Fig. 6.21 as a function of halo virial mass the relative baryon fraction defined as:

$$Y_b \equiv \frac{f_b}{\Omega_b/\Omega_m} \, . \tag{6.7}$$

For the ΛCDM case, our results for the evolution of Y_b are consistent with the value of $Y_b \sim 0.92$ found by the *Santa Barbara Cluster Comparison Project* (Frenk et al., 1999), and with the more recent results of Ettori et al. (2006) and Gottloeber and Yepes (2007), while for the coupled models the relative baryon fraction shows a progressive decrease with increasing coupling, down to a value of $Y_b \sim 0.86 - 0.87$ for the RP5 case.

It is also important to notice that this effect is always towards lower baryon fractions in clusters with respect to the cosmological value. This could in fact alleviate tensions between the high baryon abundance estimated from CMB observations, and the somewhat lower values inferred from detailed X-ray observations of galaxy clusters (Vikhlinin et al., 2006; McCarthy et al., 2007; LaRoque et al., 2006; Afshordi et al., 2007).

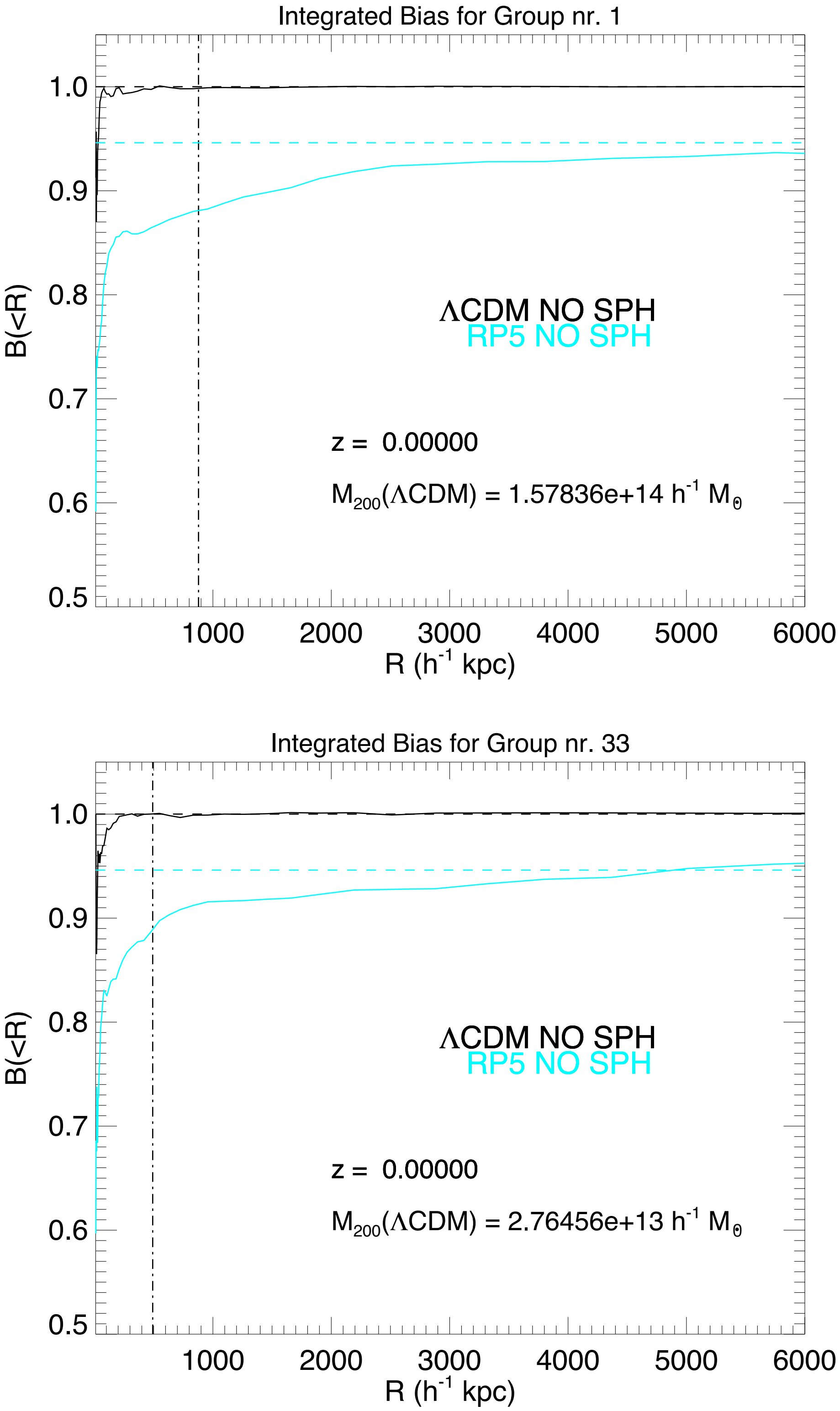

Figure 6.19: Variation of the integrated bias $B(< r)$ for the two high-resolution simulations without hydrodynamical forces on baryon particles for the same two halos shown in Fig. 6.17. The enhancement of the bias due to the extra scalar force in the core of highly non-linear structures appears here clearly.

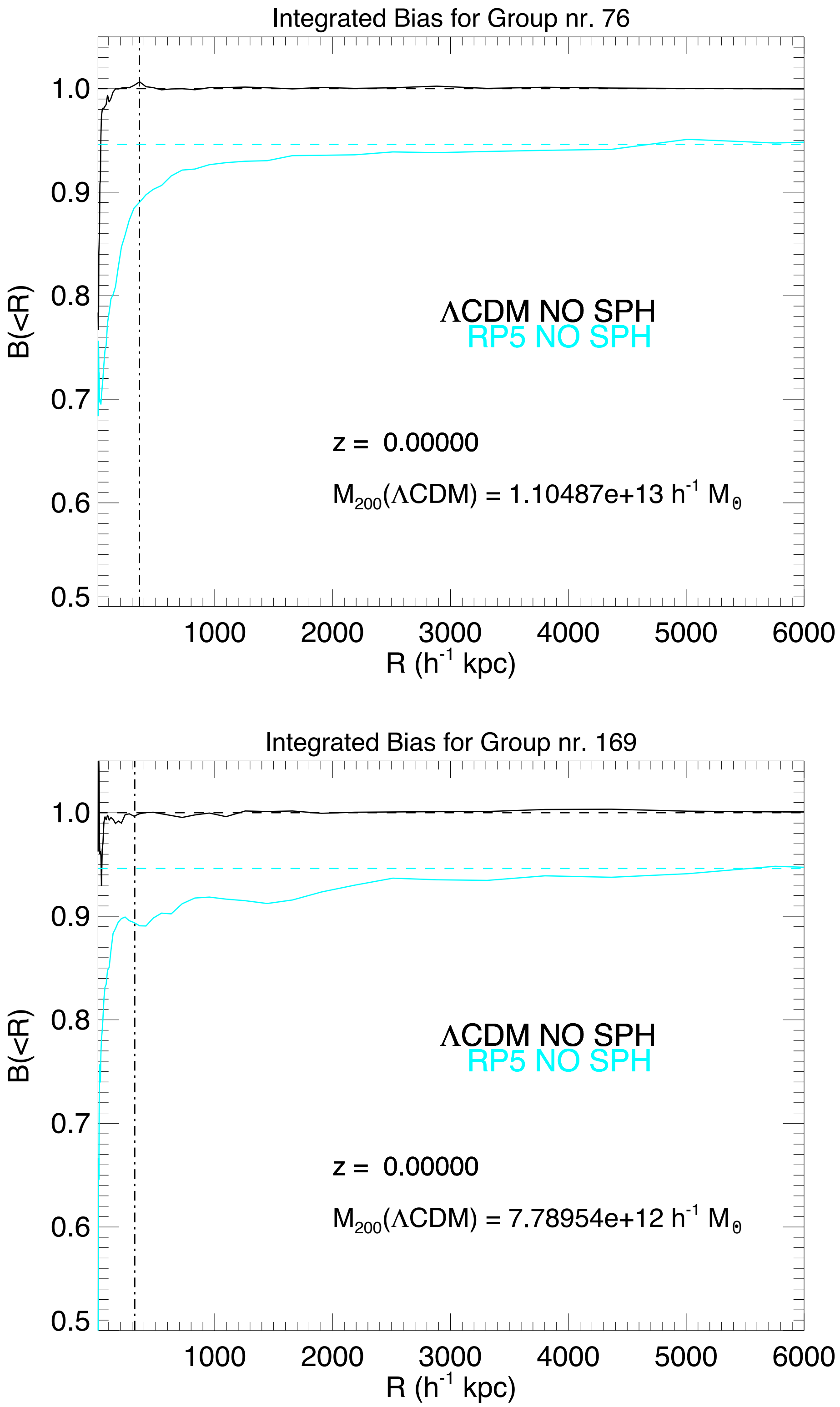

Figure 6.20: Variation of the integrated bias $B(< r)$ for the two high-resolution simulations without hydrodynamical forces on baryon particles for the same two halos shown in Fig. 6.18. The enhancement of the bias due to the extra scalar force in the core of highly non-linear structures appears here clearly.

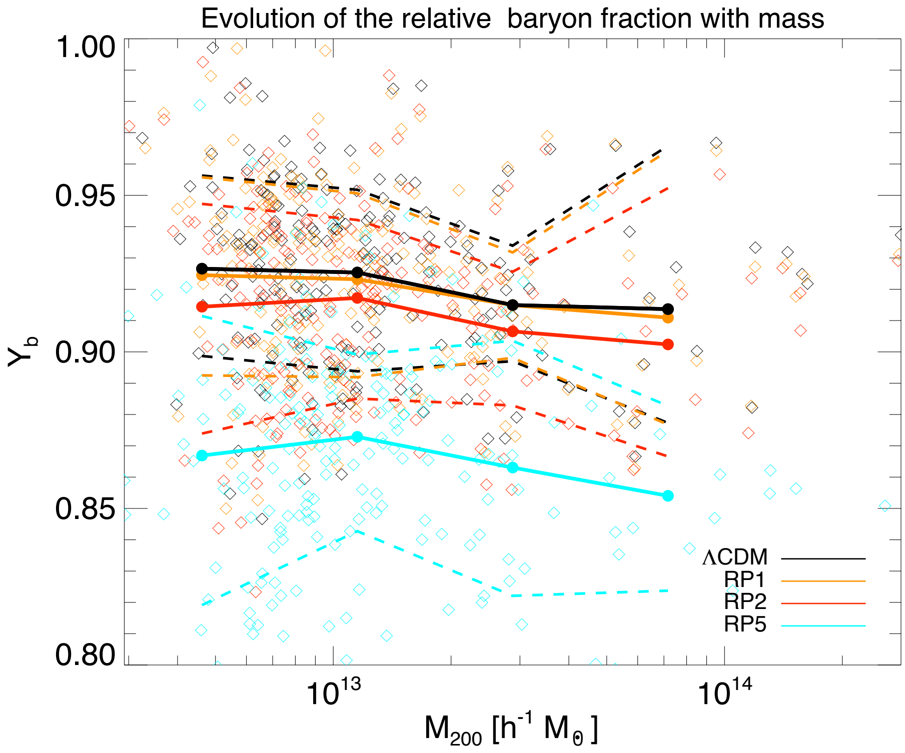

Figure 6.21: Variation with virial mass M_{200} of the relative baryon fraction Y_b within the virial radius r_{200} of all the halos in our sample. The colored diamonds represent the relative baryon fraction of each single halo, while the filled circles and the colored curves show the behavior of the mean relative baryon fraction in each mass bin for the four fully self-consistent high-resolution simulations. A decrease of Y_b with increasing coupling is clearly visible both in the distribution of the individual halos and in the averaged curves.

Conclusions

In the present work we have investigated the phenomenology of dynamic dark energy models based on the evolution of a classical scalar field moving in a self-interaction potential, for the case in which this scalar field interacts directly with other cosmic fluids.

After reviewing the most relevant features of this kind of phenomenological models and of the techniques used to constrain them at the background and linear perturbation level in Chapters 1, 2, and 3, we have presented and discussed our results in Chapters 4, 5, and 6.

Our investigation of such interacting dark energy models has been pursued from two different perspectives. The first one concerns the possibility to extend the simplest models of interaction to a situation where multiple dark matter families differently coupled to the dark energy scalar field are present in the energy budget of the Universe, as a possible solution of the *Coincidence Problem*. The second one concerns the study of the impact that the simplest models of interacting dark energy can have on the non-linear stages of structure formation, by means of the detailed analysis of high resolution N-body simulations.

The former aspect is discussed in Chapter 4, where we have shown that a simultaneous solution of the *Fine Tuning* and of the *Coincidence* problems can be given by a cosmological evolution consisting of two disjoint scaling solutions driven by two distinct dark matter families differently coupled to the dark energy scalar field. We have dubbed this scenario as the "*Growing Matter*" model, since the dark matter family driving the late time scaling solution needs to be strongly coupled to the dark energy scalar field such that the mass (and the energy density) of such *Growing Matter* species does increase with time.

We have also proposed to identify the *Growing Matter* component with cosmic neutrinos, which avoids introducing a new unknown particle in the model, and we have derived the main features of a cosmological model where neutrinos trigger the onset of the accelerated expansion of the Universe at the time when they become non-relativistic due to the fast growth of their average mass.

Interestingly, the model relates some relevant cosmological quantities (as the present dark energy density or the present dark energy equation of state w) to the average neutrino mass m_ν, and according to these relations the observed values for such cosmological quantities are compatible within the present laboratorary bounds on m_ν.

In particular, the most remarkable results of the model are given by equation 4.17:

$$[\rho_\phi(t_0)]^{1/4} = 1.27 \left(\frac{\gamma m_\nu(t_0)}{\mathrm{eV}}\right)^{1/4} 10^{-3}\mathrm{eV}\,, \tag{6.8}$$

which gives the present dark energy density in terms of the neutrino mass and of the dimensionless parameter γ of the model, and by equation 4.18:

$$w = -1 + \frac{m_\nu(t_0)}{12\mathrm{eV}}\,, \tag{6.9}$$

that relates the present dark energy equation of state to the neutrino mass.

The latter aspect is then discussed in Chapters 5 and 6, where we have investigated the non-linear effects of coupled quintessence models. To do so we have developed and tested a modified version of the cosmological N-body code GADGET-2 suitable for evolving these kinds of cosmological models. The numerical implementation we have developed is in fact quite general and not restricted to the simple specific models of coupled quintessence that we have investigated in this work. Instead, our implementation should be well suited for a much wider range of dark energy models. We also note that the ability to selectively enable or disable each of the modifications presented in Chapter 5, makes the code suitable for cosmological models that are unrelated to the coupled dark energy scenario but require similar new degrees of freedom that our implementation allows. These are:

1. the expansion history of the Universe can be specified according to any desired evolution of the Hubble rate as a function of the scale factor a;
2. a global variation in time of the gravitational constant and/or a variation in time of the gravitational strength for each individual matter species. This includes

the possibility to have a long range repulsive interaction between different particle species;

3. variation in time of the particle mass of each individual matter species;
4. friction or anti-friction terms in the equation of motion for each individual matter species.

With this implementation we have investigated the effects on structure formation of coupled dark energy models with a constant coupling β_c to the cold dark matter fluid. We have shown that the halo mass function is modified in coupled dark energy models, but can still be well fitted at different redshifts by the *Jenkins et al.* (Jenkins et al., 2001) fitting formula, or by the *Sheth & Tormen* (Sheth and Tormen, 1999) formula, which yields a moderately better agreement, especially at $z > 0$.

We have confirmed the analytic prediction that density fluctuations in baryons and cold dark matter will develop a bias on all scales due to the presence of a fifth-force acting only between cold dark matter particles. We have also shown that in addition to this the bias is enhanced when moving from the linear regime of very large scales to smaller and progressively more non-linear scales.

We have investigated the evolution of the bias between baryons and cold dark matter overdensities down to the very non-linear regime found in the inner part of collapsed objects, in the same fashion as described in Macciò et al. (2004). We found here similar results with this previous work, namely an enhancement of the bias in the non-linear region within and around massive halos. We also recover from this analysis the large scale value of the linear bias computed from the power spectrum when integrating the bias function up to very large radii from the centre of cold dark matter halos. The enhancement of the bias in highly non-linear structures has an impact on the determination of the baryon fraction from cluster measurements, and we have computed for all our halos the evolution of this fraction with coupling within the virial radius r_{200}, finding that the baryon fraction is reduced with increasing coupling by up to $\sim 8 - 10\%$ with respect to ΛCDM for the largest coupling value.

We have also investigated the effect of the coupling on the halo density profiles. We find that they are remarkably well fit over the resolved range by the *Navarro, Frenk, and White* formula (Navarro et al., 1997) for any value of the coupling. There is a clear trend for a decrease of the inner halo overdensity with respect to ΛCDM with increasing coupling (or, equivalently, an increase of the scale radius r_s for increasing coupling). This result conflicts with previous claims for the same class of coupled dark energy models (Macciò et al., 2004).

Using a number of special test simulations, we have identified the origin of this effect of reduced halo concentrations for increasing coupling. It actually arises from a combination of two peculiar features that the coupling introduces in the Newtonian limit of gravitational dynamics. The first of these is the decrease of cold dark matter particle mass with time (the opposite of what happens for the *Growing Neutrino Scenario* described above, where the mass increases due to the negative value of the coupling) which causes the absolute value of the total potential energy of a halo to decrease, and hence effectively moves the system to a configuration where an excess of kinetic energy is present relative to virial equilibrium. The second one is the additional "anti-friction" term, which directly raises the total energy of halos by accelerating their particles in the direction of their peculiar velocity. Both of these effects cause a halo to slightly expand in order to restore virial equilibrium, and this reduces the halo concentration.

In conclusion, we have developed a general numerical implementation of coupled dark energy models in the GADGET-2 code. We have then performed the first fully self-consistent high-resolution hydrodynamic N-body simulations of interacting dark energy models with constant coupling, and carried out a basic analysis of the non-linear structures that formed. Interestingly, we found that a larger coupling leads to a lower average halo concentration. Furthermore, both the baryon fraction in massive halos and the inner overdensity of cold dark matter halos decrease with increasing coupling. These effects alleviate the present tensions between observations and the ΛCDM model on small scales, implying that the coupled dark energy models are viable alternatives to the cosmological constant included in standard ΛCDM.

Acknowledgments

No piece of human work can ever be considered to belong to the activity and the effort of a single individual.
Whatever our achievements are, they always turn out to be the result of a long series of interactions with other people.

This is why, besides thanking all those who have directly collaborated with me on this work and that I have individually mentioned in the related papers, I want to acknowledge here all the people that happened to have some significant interaction with me – of any kind it might have been – during the years I have spent in Munich working on this project. In doing so, I mean to include those people who made my life easier and cheerful as well as those who happened to make it harder, since it is also through the opposite wind of difficult challenges that one discovers his own strengths and his own limits.

I purposely avoid here to make any list of names, with the sole exception of my parents, Maria Grazia and Gaetano, for the simple and obvious reason that without their unlimited support this enterprise would not have been conceivable right to start with.

Part IV

Bibliography

Bibliography

Afshordi, N., Lin, Y.-T., Nagai, D., and Sanderson, A. J. R. (2007). Missing Thermal Energy of the Intracluster Medium. *Mon. Not. Roy. Astron. Soc.*, 378:293–300.

Allen, S. W., Schmidt, R. W., Ebeling, H., Fabian, A. C., and van Speybroeck, L. (2004). Constraints on dark energy from Chandra observations of the largest relaxed galaxy clusters. *Mon. Not. Roy. Astron. Soc.*, 353:457.

Amendola, L. (2000). Coupled quintessence. *Phys. Rev.*, D62:043511.

Amendola, L. (2004). Linear and non-linear perturbations in dark energy models. *Phys. Rev.*, D69:103524.

Amendola, L., Baldi, M., and Wetterich, C. (2008). Growing Matter. *Phys. Rev.*, D78:023015.

Amendola, L., Quartin, M., Tsujikawa, S., and Waga, I. (2006). Challenges for scaling cosmologies. *Phys. Rev.*, D74:023525.

Amendola, L. and Quercellini, C. (2004). Skewness as a test of the equivalence principle. *Phys. Rev. Lett.*, 92:181102.

Armendariz-Picon, C., Mukhanov, V. F., and Steinhardt, P. J. (2000). A dynamical solution to the problem of a small cosmological constant and late-time cosmic acceleration. *Phys. Rev. Lett.*, 85:4438–4441.

Astier, P. et al. (2006). The Supernova Legacy Survey: Measurement of OmegaM, OmegaLambda and w from the First Year Data Set. *Astron. Astrophys.*, 447:31–48.

Baldi, M. and Macciò, A. V. (in prep.).

Bardeen, J. M., Bond, J. R., Kaiser, N., and Szalay, A. S. (1986). The Statistics of Peaks of Gaussian Random Fields. *Astrophys. J.*, 304:15–61.

Bartelmann, M., Doran, M., and Wetterich, C. (2005). Non-linear Structure Formation in Cosmologies with Early Dark Energy.

Bean, R., Flanagan, E. E., Laszlo, I., and Trodden, M. (2008). Constraining Interactions in Cosmology's Dark Sector.

Bean, R. and Melchiorri, A. (2002). Current constraints on the dark energy equation of state. *Phys. Rev.*, D65:041302.

Bekenstein, J. D. (2004). Relativistic gravitation theory for the MOND paradigm. *Phys. Rev.*, D70:083509.

Brans, C. and Dicke, R. H. (1961). Mach's principle and a relativistic theory of gravitation. *Phys. Rev.*, 124:925–935.

Brax, P. and Martin, J. (1999). Quintessence and supergravity. *Phys. Lett.*, B468:40–45.

Buchert, T. (2000). On average properties of inhomogeneous fluids in general relativity. I: Dust cosmologies. *Gen. Rel. Grav.*, 32:105–125.

Capozziello, S. and Francaviglia, M. (2008). Extended Theories of Gravity and their Cosmological and Astrophysical Applications. *Gen. Rel. Grav.*, 40:357–420.

Chuang, C.-H., Gu, J.-A., and Hwang, W.-Y. P. (2008). Inhomogeneity-Induced Cosmic Acceleration in a Dust Universe. *Class. Quant. Grav.*, 25:175001.

Copeland, E. J., Liddle, A. R., and Wands, D. (1998). Exponential potentials and cosmological scaling solutions. *Phys. Rev.*, D57:4686–4690.

Damour, T., Gibbons, G. W., and Gundlach, C. (1990). DARK MATTER, TIME VARYING G, AND A DILATON FIELD. *Phys. Rev. Lett.*, 64:123–126.

Di Porto, C. and Amendola, L. (2008). Observational constraints on the linear fluctuation growth rate. *Phys. Rev.*, D77:083508.

Doran, M. (2005). CMBEASY:: an Object Oriented Code for the Cosmic Microwave Background. *JCAP*, 0510:011.

Doran, M., Lilley, M. J., Schwindt, J., and Wetterich, C. (2001a). Quintessence and the separation of CMB peaks. *Astrophys. J.*, 559:501–506.

Doran, M. and Robbers, G. (2006). Early dark energy cosmologies. *JCAP*, 0606:026.

Doran, M., Schwindt, J.-M., and Wetterich, C. (2001b). Structure formation and the time dependence of quintessence. *Phys. Rev.*, D64:123520.

Doran, M., Schwindt, J.-M., and Wetterich, C. (2001c). Structure formation and the time dependence of quintessence. *Phys. Rev.*, D64:123520.

Efstathiou, G., Sutherland, W. J., and Maddox, S. J. (1990). The cosmological constant and cold dark matter. *Nature*, 348:705–707.

Einstein, A. (1917). Kosmologische betrachtungen zur allgemeinen relativitätstheorie (cosmological considerations in the general theory of relativity). *Koniglich Preußische Akademie der Wissenschaften.*

Eisenstein, D. J. and Hu, W. (1998). Baryonic Features in the Matter Transfer Function. *Astrophys. J.*, 496:605.

Ellis, G. F. R. and Stoeger, W. (1987). The 'fitting problem' in cosmology. *Class. Quant. Grav.*, 4:1697–1729.

Ettori, S., Dolag, K., Borgani, S., and Murante, G. (2006). The baryon fraction in hydrodynamical simulations of galaxy clusters. *Mon. Not. Roy. Astron. Soc.*, 365:1021–1030.

Ferreira, P. G. and Joyce, M. (1997). Structure formation with a self-tuning scalar field. *Phys. Rev. Lett.*, 79:4740–4743.

Francis, M. J., Lewis, G. F., and Linder, E. V. (2008). Halo Mass Functions in Early Dark Energy Cosmologies.

Frenk, C. S., White, S. D. M., Bode, P., Bond, J. R., Bryan, G. L., Cen, R., Couchman, H. M. P., Evrard, A. E., Gnedin, N., Jenkins, A., Khokhlov, A. M., Klypin, A., Navarro, J. F., Norman, M. L., Ostriker, J. P., Owen, J. M., Pearce, F. R., Pen, U.-L., Steinmetz, M., Thomas, P. A., Villumsen, J. V., Wadsley, J. W., Warren, M. S., Xu, G., and Yepes, G. (1999). The Santa Barbara Cluster Comparison Project: A Comparison of Cosmological Hydrodynamics Solutions. *ApJ*, 525:554–582.

Friedman, A. (1922). On the curvature of space. *Z. Phys.*, 10:377–386.

Giannantonio, T. et al. (2008). Combined analysis of the integrated Sachs-Wolfe effect and cosmological implications. *Phys. Rev.*, D77:123520.

Gottloeber, S. and Yepes, G. (2007). Shape, spin and baryon fraction of clusters in the MareNostrum Universe. *Astrophys. J.*, 664:117–122.

Grego, L. et al. (2001). Galaxy Cluster Gas Mass Fractions from Sunyaev-Zel'dovich Effect Measurements: Constraints on OmegaM. *Astrophys. J.*, 552:2.

Grossi, M. and Springel, V. (2008). The impact of Early Dark Energy on non-linear structure formation.

Hannestad, S. and Mortsell, E. (2004). Cosmological constraints on the dark energy equation of state and its evolution. *JCAP*, 0409:001.

Hubble, E. (1929). A relation between distance and radial velocity among extra–galactic nebulae. *Proc. Nat. Acad. Sci.*, 15:168–173.

Huey, G. and Wandelt, B. D. (2006). Interacting quintessence, the coincidence problem and cosmic acceleration. *Phys. Rev.*, D74:023519.

Jenkins, A. et al. (2001). Mass function of dark matter halos. *Mon. Not. Roy. Astron. Soc.*, 321:372.

Jimenez, R., Verde, L., Treu, T., and Stern, D. (2003). Constraints on the equation of state of dark energy and the Hubble constant from stellar ages and the CMB. *Astrophys. J.*, 593:622–629.

Kesden, M. and Kamionkowski, M. (2006). Tidal Tails Test the Equivalence Principle in the Dark Sector. *Phys. Rev.*, D74:083007.

Klypin, A. A., Kravtsov, A. V., Valenzuela, O., and Prada, F. (1999). Where are the missing galactic satellites? *Astrophys. J.*, 522:82–92.

Kodama, H. and Sasaki, M. (1984). Cosmological Perturbation Theory. *Prog. Theor. Phys. Suppl.*, 78:1–166.

Kolb, E. W., Matarrese, S., Notari, A., and Riotto, A. (2005). The effect of inhomogeneities on the expansion rate of the universe. *Phys. Rev.*, D71:023524.

Komatsu, E. et al. (2008). Five-Year Wilkinson Microwave Anisotropy Probe (WMAP) Observations:Cosmological Interpretation.

LaRoque, S. et al. (2006). X-ray and Sunyaev-Zel'dovich Effect Measurements of the Gas Mass Fraction in Galaxy Clusters. *Astrophys. J.*, 652:917–936.

Laszlo, I. and Bean, R. (2008). Nonlinear growth in modified gravity theories of dark energy. *Phys. Rev.*, D77:024048.

Lemaître, G. (1931). Expansion of the universe, A homogeneous universe of constant mass and increasing radius accounting for the radial velocity of extra-galactic nebul&aelig. *MNRAS*, 91:483–490.

Lucchin, F. and Matarrese, S. (1985). Power Law Inflation. *Phys. Rev.*, D32:1316.

Ma, C.-P. and Bertschinger, E. (1995). Cosmological perturbation theory in the synchronous and conformal Newtonian gauges. *Astrophys. J.*, 455:7–25.

Macciò, A. V., Quercellini, C., Mainini, R., Amendola, L., and Bonometto, S. A. (2004). N-body simulations for coupled dark energy: halo mass function and density profiles. *Phys. Rev.*, D69:123516.

Maddox, S. J., Efstathiou, G., Sutherland, W. J., and Loveday, J. (1990). Galaxy correlations on large scales. *Mon. Not. Roy. Astron. Soc.*, 242:43–49.

Mainini, R. (2005). Dark matter - baryon segregation in the non-linear evolution of coupled dark energy model. *Phys. Rev.*, D72:083514.

Mainini, R. and Bonometto, S. (2006). Mass functions in coupled Dark Energy models. *Phys. Rev.*, D74:043504.

Mainini, R. and Bonometto, S. (2007). Limits on coupling between dark components. *JCAP*, 0706:020.

McCarthy, I. G., Bower, R. G., and Balogh, M. L. (2007). Revisiting the Baryon Fractions of Galaxy Clusters: A Comparison with WMAP 3-year Results. *Mon. Not. Roy. Astron. Soc.*, 377:1457–1463.

Moore, B. et al. (1999). Dark matter substructure within galactic halos. *Astrophys. J.*, 524:L19–L22.

Mota, D. F., Pettorino, V., Robbers, G., and Wetterich, C. (2008). Neutrino clustering in growing neutrino quintessence. *Phys. Lett.*, B663:160–164.

Navarro, J. F., Frenk, C. S., and White, S. D. M. (1996). The Structure of Cold Dark Matter Halos. *Astrophys. J.*, 462:563–575.

Navarro, J. F., Frenk, C. S., and White, S. D. M. (1997). A Universal Density Profile from Hierarchical Clustering. *Astrophys. J.*, 490:493–508.

Nusser, A., Gubser, S. S., and Peebles, P. J. E. (2005). Structure formation with a long-range scalar dark matter interaction. *Phys. Rev.*, D71:083505.

Oyaizu, H. (2008). Non-linear evolution of f(R) cosmologies I: methodology.

Paranjape, A. and Singh, T. P. (2006). The Possibility of Cosmic Acceleration via Spatial Averaging in Lemaitre-Tolman-Bondi Models. *Class. Quant. Grav.*, 23:6955–6969.

Peacock, J. A. et al. (2001). A measurement of the cosmological mass density from clustering in the 2dF Galaxy Redshift Survey. *Nature*, 410:169–173.

Peebles, P. J. E. (1980). *The Large-Scale Structure of the Universe*. Princeton University Press.

Penzias, A. A. and Wilson, R. W. (1965). A Measurement of excess antenna temperature at 4080- Mc/s. *Astrophys. J.*, 142:419–421.

Percival, W. J. et al. (2001). The 2dF Galaxy Redshift Survey: The power spectrum and the matter content of the universe. *Mon. Not. Roy. Astron. Soc.*, 327:1297.

Perlmutter, S. (2008). http://supernova.lbl.gov/.

Perlmutter, S. et al. (1999). Measurements of Omega and Lambda from 42 High-Redshift Supernovae. *Astrophys. J.*, 517:565–586.

Pettorino, V. and Baccigalupi, C. (2008). Coupled and Extended Quintessence: theoretical differences and structure formation. *Phys. Rev.*, D77:103003.

Pettorino, V., Mota, D. F., Robbers, G., and Wetterich, C. (2009). Clustering in growing neutrino cosmologies.

Press, W. H. and Schechter, P. (1974). Formation of galaxies and clusters of galaxies by selfsimilar gravitational condensation. *Astrophys. J.*, 187:425–438.

Ratra, B. and Peebles, P. J. E. (1988). Cosmological Consequences of a Rolling Homogeneous Scalar Field. *Phys. Rev.*, D37:3406.

Riess, A. G. et al. (1998). Observational Evidence from Supernovae for an Accelerating Universe and a Cosmological Constant. *Astron. J.*, 116:1009–1038.

Robertson, H. P. (1935). Kinematics and World-Structure. *ApJ*, 82:284–+.

Rubakov, V. A. and Shaposhnikov, M. E. (1983). Extra Space-Time Dimensions: Towards a Solution to the Cosmological Constant Problem. *Phys. Lett.*, B125:139.

Sheth, R. K. and Tormen, G. (1999). Large scale bias and the peak background split. *Mon. Not. Roy. Astron. Soc.*, 308:119.

Springel, V. (2005). The cosmological simulation code GADGET-2. *Mon. Not. Roy. Astron. Soc.*, 364:1105–1134.

Springel, V. and Farrar, G. R. (2007). The speed of the 'bullet' in the merging galaxy cluster 1E0657-56. *MNRAS*, 380:911–925.

Springel, V., Wang, J., Vogelsberger, M., Ludlow, A., Jenkins, A., Helmi, A., Navarro, J. F., Frenk, C. S., and White, S. D. M. (2008). The Aquarius Project: the subhaloes of galactic haloes. *MNRAS*, 391:1685–1711.

Springel, V., White, S. D. M., Tormen, G., and Kauffmann, G. (2001). Populating a cluster of galaxies - I. Results at [formmu2]z=0. *MNRAS*, 328:726–750.

Stabenau, H. F. and Jain, B. (2006). N-Body Simulations of Alternate Gravity Models. *Phys. Rev.*, D74:084007.

Sutter, P. M. and Ricker, P. M. (2008). Detecting dark matter-dark energy coupling with the halo mass function.

Vikhlinin, A. et al. (2006). Chandra sample of nearby relaxed galaxy clusters: mass, gas fraction, and mass-temperature relation. *Astrophys. J.*, 640:691.

Walker, A. G. (1937). On milne's theory of world-structure walker. *Proc. London Math. Soc..1937; s2-42: 90-127*.

Weinberg, S. (1972). *Gravitation and Cosmology: Principles and Applications of the General Theory of Relativity*. John Wiley & Sons.

Wetterich, C. (1988). Cosmology and the Fate of Dilatation Symmetry. *Nucl. Phys.*, B302:668.

Wetterich, C. (1995). The Cosmon model for an asymptotically vanishing time dependent cosmological 'constant'. *Astron. Astrophys.*, 301:321–328.

Wright, E. L. et al. (1992). Interpretation of the Cosmic Microwave Background radiation anisotropy detected by the COBE differential microwave radiometer. *Astrophys. J.*, 396:L13–L18.

Xia, J.-Q. and Viel, M. (2009). Early Dark Energy at High Redshifts: Status and Perspectives.

Zel'dovich, Y. B. (1970). Gravitational instability: An Approximate theory for large density perturbations. *Astron. Astrophys.*, 5:84–89.